

# Collective Migration of Epithelial Sheets

by

Michael Peter Murrell

Submitted to the Department of Biological Engineering  
in partial fulfillment of the requirements for the degree of

Doctor of Philosophy in Biological Engineering

at the

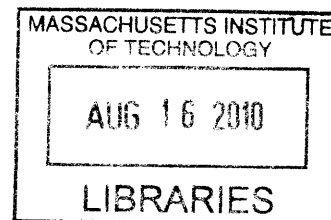
MASSACHUSETTS INSTITUTE OF TECHNOLOGY

**ARCHIVES**

April 2009

[June 2009]


©Michael P. Murrell, 2009.



Author .....  .....

Department of Biological Engineering

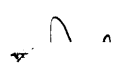
May 21, 2009

Certified by .....  .....

Roger D. Kamm

Professor, MIT

Thesis Supervisor

Certified by .....  .....

Paul Matsudaira

Professor, NUS

Thesis Supervisor

Accepted by .....  .....  .....

Alan Grodzinsky

Chairman, Department Committee on Graduate Students



# Collective Migration of Epithelial Sheets

by

Michael Peter Murrell

Submitted to the Department of Biological Engineering  
on May 21, 2009, in partial fulfillment of the  
requirements for the degree of  
Doctor of Philosophy in Biological Engineering

## Abstract

The varied movements of the epithelium play vital roles in the development and renewal of complex tissues, from the separation of tissues in the early embryo, to homeostasis in the adult. Their movement is intricately connected to their proper functioning as selective barriers of the intestinal mucosae, as well re-epithelialization in the healing of wounds. Yet, considering their ubiquity and relevance, the basic origin of the collective motion of sheets has eluded a clear and quantitative interpretation in physical terms, prohibited by the lack of understanding of the relationship between motility, cell-cell contact, and their mediation by the mechanical properties of the substratum to which they adhere. Therefore, within this context, this thesis defines the prerequisites for both equilibrium and non-equilibrium coordinated cell motion. The timescales and lengthscales of the *in vitro* migration of an epithelial monolayer were calculated and compared under imposed constraints designed to mimic various states of *in vivo* epithelia. These constraints include assays that recreate the wound response of the epithelium such as what is seen in the cornea and epidermis, by unequivocally separating the influence of free space from cell damage in the induction of coordinated motion. The motion of the epithelium was further explored by the generation of gradients that reproduce asymmetry in the capacity for cells to migrate, divide, or undergo apoptosis, such as what is found along the crypt-villus axis of the intestine. Finally, as the epithelium adheres and migrates against the basal lamina, a substrate of uncertain *in vivo* mechanical properties, we explored the contribution of substrate viscoelasticity to the dynamics of coordinated migration. Parameterized this way, multiple modes of motility emerge, each distinct dynamically, phenotypically, and in their dependence on cell-cell contact.

Thesis Supervisor: Roger D. Kamm  
Title: Professor, MIT

Thesis Supervisor: Paul Matsudaira  
Title: Professor, NUS

## Acknowledgments

Being able to perform research at MIT, and in the Department of Biological Engineering has been an extraordinary blessing. Therefore, I have to give thanks to He from whom all blessings flow, my Lord and Savior, Jesus Christ. His love is great, and his mercy is never-ending.

I devote this thesis, to my grandparents, Dr. and Mrs. Peter C. Murrell. I would have never been able to get this far, without their love and support. They raised me, provided for me, and sacrificed for me to bring me to this point, so this PhD belongs to them more than it belongs to me.

In addition, I have also benefited greatly from the body of Christ here in Cambridge, the Black Graduate Ministries (BGM) Group. They have been a huge source of support, and without them, this would not have been possible. They have become family to me over the last couple of years. This includes my close friends Renee Smith, Pierre Fuller, Christopher Rhodes, and Heather McLetchie-Leader. In addition BGM, my good friends Alex and Karen Sheh have not only been a source of support, but a source of inspiration of the years. Without them, this work also would not have been possible. Their constant, unwavering faith, serves as an example that I intend to emulate.

And, of course I have to give thanks to the members of my Thesis Committee. I have had unparalleled freedom to pursue my interests. I have always had open access to the resources necessary for accomplishing the work.



# Thesis Committee

Accepted by..........

Roger D. Kamm

Professor of Biological Engineering and Mechanical Engineering (MIT)

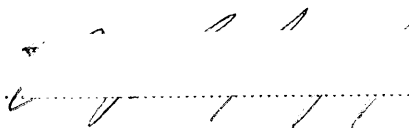
Thesis Supervisor

Accepted by..........

Paul Matsudaira

Professor of Biology (National University of Singapore)

Thesis Supervisor

Accepted by..........

Douglas Lauffenburger

Professor of Biological Engineering and Chemical Engineering (MIT)

Committee Chairman



# Contents

<b>1</b>	<b>Introduction</b>	<b>31</b>
1.1	<i>In vitro</i> models of Sheet Motion . . . . .	31
1.1.1	Wound Healing . . . . .	33
1.1.2	Model Wounds . . . . .	34
1.1.3	Cell Sorting . . . . .	36
1.2	Summary of Open Questions . . . . .	38
1.3	Summary of Testable Hypotheses . . . . .	42
1.4	Appendix . . . . .	46
1.4.1	A note on adhesion in the intestinal epithelium . . . . .	46
<b>2</b>	<b>Initial and Boundary Conditions in the Collective Migration of Epithelial Sheets</b>	<b>57</b>
2.1	Introduction . . . . .	57
2.2	Materials and Methods . . . . .	59
2.3	Mathematical Analysis . . . . .	61
2.4	Free Space is Sufficient for Generating Collective Motion . . . . .	62
2.4.1	Dynamics of the border . . . . .	63
2.4.2	Dynamics of the bulk . . . . .	64
2.5	Free Space is Necessary for Generating Collective Motion . . . . .	65
2.5.1	Closed Boundaries . . . . .	65
2.6	Conclusions . . . . .	66
2.7	Supplemental Information . . . . .	67
2.7.1	Density Dependence for Equilibrium Movement . . . . .	67

2.8	Appendix . . . . .	80
2.8.1	Shear Stress in the Microfluidic Channel . . . . .	80
2.8.2	Alternate Gradients in Motility . . . . .	82
2.8.3	Viability in the Microfluidic Chamber . . . . .	84
2.9	Protocols . . . . .	85
2.9.1	Soft Lithography of 100 $\mu\text{m}$ high channels . . . . .	85
2.9.2	Immunostaining Adhesions inside the microfluidic channel . . . . .	88
<b>3</b>	<b>Substrate Mechanics and Cell Contact in Epithelial Cell Motion</b>	<b>95</b>
3.1	Introduction . . . . .	95
3.2	Materials and Methods . . . . .	96
3.3	Coupling of monolayer and bulk . . . . .	100
3.4	Correlated Dynamics follow a second-order transition with substrate viscoelasticity . . . . .	101
3.5	Substrate Viscoelasticity inversely modulates positional and dynamic correlation . . . . .	102
<b>4</b>	<b>Motion of Epithelial Sheets as a function of Population Size</b>	<b>119</b>
4.1	Introduction . . . . .	119
4.2	Materials and Methods . . . . .	120
4.3	Dynamics vary only with density, not population . . . . .	123
4.4	Confinement on Substrates of Varying Rigidity . . . . .	124
4.5	Appendix . . . . .	124
4.5.1	Free Space sufficient for generating "Purse-String" . . . . .	124
4.6	Protocols . . . . .	126
4.6.1	Preparing Aldehyde Terminated PDMS Surfaces . . . . .	126
4.6.2	Stamping onto PDMS . . . . .	128
4.6.3	Ninhydrin Test for Primary Amines . . . . .	130
<b>5</b>	<b>Supplemental Studies To Sheet Motion</b>	<b>139</b>
5.1	Computational Methods . . . . .	139

5.1.1	Dynamic Monte Carlo Simulations . . . . .	139
5.1.2	Velocity Correlations and the Elastic Wave Equation . . . . .	141
5.1.3	Dynamic Structure Factor and Collective Modes . . . . .	142
5.1.4	Dynamic Susceptibility . . . . .	146
5.1.5	Modeling the Sheet as a 2D XY Ferromagnetic Material . . . . .	151
5.2	Cell Mechanics . . . . .	157
5.2.1	Cell Shear Modulus Calculation . . . . .	157
5.2.2	Controls . . . . .	167
<b>6</b>	<b>Conclusions and Review of the Initial Hypotheses</b>	<b>173</b>
6.1	The influence of free space in coordinated migration . . . . .	174
6.2	Density and Contact Dependence in Compliant and Non-Compliant Models . . . . .	175
<b>7</b>	<b>Future Work</b>	<b>177</b>
<b>8</b>	<b>Derivations and Tutorials</b>	<b>179</b>
8.1	Why Statistical Mechanics? . . . . .	179
8.2	Definitions . . . . .	181
8.3	How do we approach the construction of a S.M. problem? . . . . .	183
8.4	Important Principles . . . . .	185
8.5	Microcanonical Ensemble (N,V,E) . . . . .	187
8.6	The Canonical Ensemble (N,V,T) . . . . .	189
8.7	Freely Jointed Chain . . . . .	192
8.8	Worm-Like Chain . . . . .	196
8.9	Derivation of the Master Equation . . . . .	200
8.10	The Fokker-Planck Equation . . . . .	201
8.11	Fluctuation-Dissipation . . . . .	202
8.12	Basic Thermodynamics . . . . .	207
8.13	Useful Mathematics . . . . .	209
8.14	Thermodynamic Variables and the Partition Function . . . . .	210

8.15 Example: Proving the Ideal Gas Law . . . . .	211
8.16 Example: Proving Hooke's Law in an Ideal Polymer . . . . .	214
8.17 Example: Force-Dependent Equilibrium Constants(1) . . . . .	218
8.18 Example: Force-Dependent Equilibrium Constants (2) . . . . .	220
8.19 Good References . . . . .	221

# List of Figures

- 1-1 WOUND HEALING IN AN MDCK MONOLAYER. Wound closure in MadinDarby canine kidney (MDCK) epithelial cell monolayers. (ac) Phase-contrast micrographs of MDCK cells after wounding and microinjection with 2.5 mg/ml solution of OG dextran into the first three rows of cells around the wound margin (concentration in cells after microinjection is 1/10th that of the microinjected solution or 250 g/ml). Cells are shown (a) immediately after wounding and microinjection, (b) after 6 h, and (c) after 18 h. The scale bar represents 50  $\mu$ m. All figures for each treatment in this paper are representative of experiments performed in triplicate on at least three separate occasions (n=9). Figure and caption taken from [1] . . . . . 48
- 1-2 ACTIN PURSE STRING IN WOUND CLOSURE. Repair of in vitro wounds made in monolayers of the gut epithelial cell line Caco-2BBE is achieved by lamellipodial crawling or purse-stringing, or a combination of both. In this wound, one group of leading-edge cells is being drawn forwards by contraction of an actin cable (arrows), as occurs during embryonic repair, while other cells are clearly extending lamellae (arrowheads) and crawling forwards, as occurs during repair of an adult skin wound (image courtesy of J. Brock). Green staining is fluorescein isothiocyanate/ phalloidin-tagged filamentous actin; red staining is the nuclear dye 7AAD. Image and caption taken from [2] . . . . . 49

1-3	CELL SORTING. Sorting in mixtures of 7-day chick embryo neural retina (clear) and pigmented retina (black). (a) control culture after 2 hours (initial aggregate), (b) control culture at an intermediate stage of mixing, (c) complete sorting occurs in control culture after one day, (d) partial sorting occurs membrane ruffling and pseudopod formation are disrupted. Image taken from [3] . . . . .	50
1-4	DIAGRAM OF "MODEL" WOUND. Thin PDMS films with holes in the shapes of long strips are placed on a cell culture surface, and cultured with MDCK cells (top panel). After the cells have bound, the film is removed, leaving behind cells exposed to a virgin surface. The cells then move migrate out into free space (bottom panel). Cells are shown for (a) 90 minutes, (b) 13 hours, (c) 25 hours, or (d) 37 hours after removal. This is the predominant, and most widely accepted model thus far. Image taken from [4] . . . . .	51
1-5	MOVEMENT OF THE INTESTINAL EPITHELIUM. Histoautoradiographs of small intestine at length 33% after 1 month of exposure (270). A, d1; B, d2; C, d5 after Pu ingestion. Image and Caption taken from: [5] . . . . .	52
1-6	HISTOLOGY OF THE SMALL INTESTINE. Histological Image of the villi of the small intestine. Taken from Kansas University Medical Center ( <a href="http://www.kumc.edu/instruction/medicine/anatomy/histoweb/">http://www.kumc.edu/instruction/medicine/anatomy/histoweb/</a> )	53
1-7	EPITHELIAL CELLS OF THE SMALL INTESTINE. Epithelial cells of the small intestine are columnar, and have no visible actin-based extensions, such as lamellipodia, filopodia, or pseudopodia. Taken from Kansas University Medical Center ( <a href="http://www.kumc.edu/instruction/medicine/anatomy/his">http://www.kumc.edu/instruction/medicine/anatomy/his</a>	



1-8 CADHERIN IN THE INTESTINE. Distribution of E-cadherin and  $\beta$ -catenin in fetal (AC) and adult (DF) human small intestine. Frozen sections of fetal intestine between 18 and 20 weeks of gestation were costained with a rabbit antibody to E-cadherin and a mouse anti- $\beta$ -catenin. The secondary antibodies, anti-rabbit conjugated to rhodamine, and anti-mouse conjugated to FITC, allowed the detection of E-cadherin (A and D) and  $\beta$ -catenin (B and E) independently. Overlays of both stainings (C and F) show the differential localization of the two proteins. Numbers in overlay pictures point to individual cell position in the crypts, position 1 indicating the bottom. Scale bars = 15  $\mu$ m. Image and Caption taken directly from [6] . . . . . 54

1-9 CADHERIN IN THE INTESTINE. Quantitation of E-cadherin (A),  $\beta$ -catenin (B), and the difference E-cadherin minus  $\beta$ -catenin (C) fluorescence stainings shown in Fig. 1. Quantifications were performed as described in Materials and methods on native images. Graphics present results obtained with four crypt/villus axes for 10 fetal and 7 adult tissues. Cell positions in the crypt are indicated by the number below the histograms. Bars 1620 represent means of cells at positions 1620 from each crypt side; these values were used as references for statistics ( $*p < 0.05$ ,  $**p < 0.02$ ). Image and Caption taken directly from [6] . . . . . 55

1-10 LAMININS AND INTEGRINS IN THE INTESTINE. Distribution of laminins and their corresponding integrins along the crypt-villus axis of the adult human small intestine. Laminin-1 ( $\alpha1\beta1\gamma1$ ) and laminin-2 ( $\alpha2\beta1\gamma1$ ) show complementary locations while laminin-5 ( $\alpha3\beta3\gamma2$ ) is restricted to the villus. Among integrins,  $\alpha6\beta4$ , which can bind to these three laminins, is distributed uniformly, while the basal distribution of  $\alpha3\beta1$  in intestinal cells coincides with the location of its specific ligand, laminin-5. In contrast, the laminin-1 binding integrin  $\alpha7\beta1$  is primarily expressed in the differentiating compartment. Image and Caption taken directly from [7]. . . . . 56

2-1 DIAGRAM OF MICROFLUIDIC SYSTEM. (A). Three inlets lead into a main channel, each 500  $\mu\text{m}$  wide, and 100  $\mu\text{m}$  high. When the volumetric flow rate that retracts fluid into the channel from the inlets is greater than 10  $\mu\text{L}/\text{min}$ , the flow is laminar, and the fluid from the three inlets flow side by side, separated over short distances into the channel, (B). The trypsin channel can either be at the side, or in the middle. (C) All migration experiments utilize a flow of 30  $\mu\text{L}/\text{min}$ . At this rate to enzymatically cleave cells with trypsin, carrying the away with the flow. After they have been removed, media is switched to the trypsin inlet, and the flow is reduced to 0.5  $\mu\text{l}/\text{min}$ , and we image the movement of the viable cells. . . . . 68

2-2	DIMENSIONS AND FLOW IN THE MICROFLUIDIC CHANNEL. 3D Confocal Image of the microfluidic channel, with three separate fluid streams (all cell media, at a volumetric flow rate of 30 $\mu\text{L}/\text{min}$ ), with two separate fluorescent dyes, 568 Alexa Fluor (inner stream) and 647 Alexa Fluor (outer streams). The shear, $\tau$ , across the cell monolayer varies with the inverse square of the channel height (approximately, as we cannot say $w \gg h$ ), and the inverse of the width. The initial flow used to separate the laminar flows, yields an initial shear stress of $4.4\text{dyn}/\text{cm}^2$ , which is held for 5-10 minutes. After the cells have been cleaved from the channel, the flow is reduced, and the shear drops to $0.073\text{dyn}/\text{cm}^2$ . This flow is chosen to be arbitrarily small, such that the shear stress is negligible, but yet fresh media is constantly being delivered to the cells. . . . .	69
2-3	MEAN CELL VELOCITIES FOR WOUND AND MODEL WOUND. Cells are stained with 1:1000 CMFDA, and imaged over the course of 12-36 hours, on either a Mattek Dish (Wound Healing Assay, denoted WH), or inside the microfluidic channel (having isolated free space alone, with no cell damage, denoted as FS). The mean velocities for cell motion over this time are shown for experiments with no free space (control), or with denudation at low and high densities. Also at high density, 200 $\mu\text{g}$ of anti E-cadherin antibody was added. The mean velocities are significantly increased when cell contact is blocked. . . .	70
2-4	HIGH DENSITY MOVEMENT AFTER ENZYMATIC DENUDATION. (A). Brightfield image of 0.05% Trypsin cleaving cells from the left hand side of a 500 $\mu\text{m}$ wide channel. At high densities, fingering instabilities often occur, and result in little net movement after (B) 0, (C) 1day, (D) 1.5 days, all stained with DiI, a calcium stain. The instability itself is highly motile in the direction perpendicular to, but not parallel to the axis of initial penetration. . . . .	71

2-5	LOW DENSITY MOVEMENT AFTER ENZYMATIC DENU- DATION. At low density, there is much faster net movement, and the reoccupa- tion of free space, although principally, cells will tend to scatter, rather than more uniformly, or form secondary structures, like the fingering instability. Images are taken after (A) 0, (B) 1 day (C) 1.5 days. . . .	72
2-6	E-CADHERIN AT DIFFERENT DENSITIES. E-cadherin staining from enzymatically denuded microfluidic experiments, taken at different den- sities. (A) 25x image of a cleaved (T=0) sheet inside of a channel, with an intermediate density. Within this fully confluent sheet, there are regies of both high density and low density, as can be seen by the het- erogeneous expression of E-cadherin. Similarly shown at 100x, at both low (B) or high (C) densities. . . . .	73
2-7	CADHERIN TIME COURSE. E-cadherin staining on samples taken (A) 0 hrs, (B) 6 hrs, or (C) 12 hours after being denuded by phase separated flow. Fingering instabilities arise slowly, due to the clear persistence of cadherin at high densities at the leading edge (arrows in (C)). . . . .	74
2-8	LATENCY IN MIGRATION FOLLOWING PHYSICAL WOUND. Ensemble averaged real time velocity correlation function for wound (WH) (A) and model wound (FS) (B) experiments. The red plot is the leading edge cells, followed by cells 50 $\mu\text{m}$ (gray) and 100 $\mu\text{m}$ (black) behind the leading edge. Both models show a separation of timescales for the onset of correlated behavior, although there is a significantly greater latency for the the submaginal cells in the model wound system than the wound healing assay. This is indicated by the sudden jump in correlation for the gray and black curves, after some time delay. . .	75

2-9	MEAN COSINE FOR LOW DENSITY SHEETS. Movement for sub-confluent sheets (A,C) is generally random, either progressing directly to zero post denudation, or constantly oscillating back and forth. The yellow dots are cells at the beginning of the time course that will eventually persist for $\langle \cos\theta \rangle > 0.3$ . At low density, they are dispersed throughout the sheet, while at intermediate to high densities, they are relegated to the periphery. For sheets of increased density (B,D), there is a mean direction, with most cells moving out into free space. . . . .	76
2-10	MEAN COSINE FOR HIGH DENSITY SHEETS. As the density of the cell monolayers reaches a maximum (A,C), nearly all directed movement is ablated. Cell movement is relegated purely to the periphery, with virtually no net directed movement in the bulk. When epithelial E-cadherin is blocked with monoclonal antibody (B,D), this effect is reversed, and even at high density, highly coordinated, directed movement is observed. In fact, the transition to coordinated movement is highly linear in time, as is its subsequent randomization when the density evens out (when both sides of the denudation meet each other).	77
2-11	DYNAMICS OF THE BORDER. The rate of re-epithelialization of the free space depends highly on density, being slow at both very low density, where cells scatter, and very high densities, which are retarded by cell contact. This is evident in the slopes of the recovery of this area (A). This can be seen in the slope plotted for wounds (WH) and "model" wounds (FS) at different densities (B). Both methods of denudation, the wound (gray), and the model wound (black) show this same dependence, although the speed of recovery is faster in the wound.	78
2-12	GRADIENT IN CONTRACTILITY. 200 $\mu$ M blebbistatin was used to make the left side of the monolayer non-contractile, by decreasing the affinity of Myosin II for filamentous actin (A). The right side is untreated. The results show that there is no directed movement by the untreated cells in preference for the non-contractile side (B). . . . .	78

2-13 GRADIENT IN APOPTOSIS. 0.0875% $H_2O_2$ was delivered to the left side, to induce apoptosis (A). This was imaged by a live/dead stain over 12 hours. (The tracked data in (B) however, was over roughly 24 hours, at half that concentration (0.042%)). . . . .	79
2-14 (A) Live Dead Stain with the middle channel filled with paraformaldehyde, and ran for just 2 minutes. The right side remains alive, but only for a short period of time. Fixing one side of the cells, even with no diffusion to the right, still killed the cells on the right hand side. There is likely a cell-cell communication signal that makes cell death proceed quickly across the entire length of the sheet. Thus, there was no chance to observe any migration in the viable population. (B) Brightfield image of both fixed and unfixed cells. . . . .	83
2-15 FUNCTIONAL BOUNDARIES. (A) Viable cells interface with apoptotic cells (red: apoptotic, green: viable), and (B) Motile cells interface with Non-Motile cells (Gray: Motile, Red: Non-motile). In neither case to the fully functional, viable cells push. No extension of border. . . .	83
2-16 CYTOCHALASIN D. The left channel was filled with 5 $\mu$ M cytochalasin D, creating a gradient across the lateral axis. The cytochalasin has a dye that emits at 468nm, and the right hand side was filled with normal medium, with 1:10000 DiI. Thus the red side has an altered cytoskeleton, with its actin unable to polymerize. The right hand side is normal. There was also no gradient in migration observed here. . .	90
2-17 LIVE/DEAD IN MICROFLUIDICS. After the trypsin cut, all of the cells are alive. (A) brightfield, (B) calcium dye . . . . .	90

2-18 MEAN COSINE. Calculation of the mean cosine. For equilibrium (no free space) movement (A), the cosine of the angle between vectors separated by an elapsed time, $\tau$ are averaged for the ensemble of trajectories over all t (B). That allows us to characterize the PDF for the angle of movement (C). If movement is non-equilibrium, as in wound healing and microfluidic denudation studies, it is calculated in real time, as the cosine of the angle between successive vectors (D,E). . . . .	91
2-19 DENSITY DEPENDENCE. The density dependence of the mean cosine calculation for equilibrium movement. As the density is increased, the correlation lengthscale of the angle between successive vectors during the migration of cells within a sheet, decreases. With the smaller the magnitude of the scaling exponent, the longer the paths will persist as straight. . . . .	92
2-20 LEADING EDGE CELL MORPHOLOGY. Morphology of a leading edge CMFDA-stained cell in front of a fully confluent sheet, imaged at 100x. Grid = $2\mu\text{m}$ . . . . .	93
2-21 SUBMARGINAL CELL MORPHOLOGY. Morphology of a submarginal GFP-cell in a fully confluent sheet, imaged at 100x. Grid = $2\mu\text{m}$ . Z slices are at 0.8um, 2.8um, and 10.8 um from the surface. . . . .	93
2-22 SURFACE PROTEIN REMOVAL. The denudation of cells, whether by physical scratching (A) with a 1ml pipette tip, or by enzymatic cleavage (B), removes surface protein (FN+FITC Collagen). In both cases, the new protein is added by the medium (that contains 10% FBS). 94	94
2-23 RETENTION OF ADHERENS JUNCTIONS DURING SHEET MOTION. During Wound Healing, as the sheet moves forward, the leading edge displays both focal adhesions (A, characteristic to single cell movement), as well as maintaining adherens junctions (B, characteristic to sheets). This is a fixed sample, stained with rhodamine-phalloidin. . .	94

3-1	<p>BASAL LAMINA ANALOG. Rheology of Matrigel (red), and 1/80 PDMS (black). Storage (.), Loss (o) Moduli. For this composition of PDMS, the rheology nearly matches that for Matrigel, for low frequencies. We stop our comparison at <math>10^{-1}</math> radians/s, as below this frequency, we are uncertain concerning the rise in <math>G'</math> and <math>G''</math> . . . . .</p>	104
3-2	<p>SURFACE PROTEIN AS A FUNCTION OF STIFFNESS. FITC-stained gelatin bound to fibronectin, attached nonspecifically (A-C) or covalently (D) to PDMS in a ratio of (A) 1/10, or (B,C,D) 1/80, which is the critical combination of stiffness and wettability that characterizes the most correlated state, and is thereby marked with a red star. . . . .</p>	105
3-3	<p>CELL TRAJECTORIES. Trajectories of dense cell populations on non-compliant (1/10) low density (A) and high density (B) or compliant (1/80) high density (C) surfaces. At low densities on non-compliant substrates, the trajectories are very coherent and coordinated. High density generally ablates this coherence on non-compliant substrates, but small domains of highly coordinated movement persists when the substrate is compliant. . . . .</p>	106
3-4	<p>COUPLING OF CELL MOTION AND BULK MOTION. Velocity autocorrelations for cell movement (black) and bead displacement (gray) in substrates of varying viscoelasticity. As the stiffness of the surface dips below 67.7 Pa, the timescales converge, with the substrate movement mirroring the cell movement. . . . .</p>	107



3-5	DECOUPLING OF CELL MOTION AND BULK MOTION. (A) Cell autocorrelation on 1/80 PDMS, with fibronectin covalently linked. (B) Cell autocorrelation on 1/80 PDMS, with covalently linked fibronectin, and 200 $\mu$ g anti-E-cadherin antibody to block cell-cell contact. The persistence of cell motion is not altered on this non-compliant substrate with the removal of cell-cell contact, but the correlation is no longer conferred to the substrate (same bead scaling as 1/10 PDMS composition). . . . .	108
3-6	COUPLING BETWEEN CELL MOTION AND BULK AS A FUNCTION OF CELL CONTACT. Velocity autocorrelations for cell movement (black) and bead displacement (gray) on both hard (and elastic) and soft (and viscous) substrates. For hard, elastic substrates, the absence of cell-cell contact, does not alter the persistence of single cell motion. However, on soft substrates, blocking E-cadherin separates the timescales between the cell motion and the persistence, as well as decreasing the magnitude and scaling of the autocorrelation function. . . . .	109
3-7	PERSISTENCE AS A FUNCTION OF DENSITY. Both deformable (gray) and non-deformable (black) substrates have roughly the same scaling behavior for all highly confluent densities. Cell motion persists for longer (and hence have a lower power law exponent) when the density is low, which is not possible on deformable substrates, as cells will compact. . . . .	110
3-8	DISTINCT VELOCITY CORRELATIONS. Mutual Velocity Correlation Functions (1hr), for dense cell populations on 14.4 Pa (light gray), 287 Pa (med gray), and 35 kPa (black) substrates. . . . .	111

3-9	SECOND ORDER TRANSITION IN MUTUAL CORRELATION. Taking the scaling exponent, $\alpha'$ , of the mutual velocity correlation function for each value of $ G $ , maps out a continuous transition from the non-compliant and less correlated ( $\sim 1/r^{1.0}$ ) to the compliant and more correlated ( $\sim 1/r^{0.3}$ ). The inset is the mean velocity of the cells, with the velocity of the beads subtracted, as the instability causes a net drift. This relative velocity is constant for all measured moduli. . . . .	111
3-10	VAN HOVE CORRELATIONS. (A) radial distribution function for two systems, compliant (gray) and noncompliant (black). (B) Timescale of the evolution of the spring and damping constants, characterized by time evolution of their ratio, $\zeta = \kappa/\eta \sim t^{\tau/\tau^*}$ . (C) Time-scaling of beads in PDMS. (D) Relationship between timescale of cell organization and timescale of bead displacement. . . . .	112
3-11	PDMS RHEOLOGY. Rheology of PDMS of different curing agent concentrations. $G(\omega)$ dark, $G'(\omega)$ light, and follow: 1/10, 1/20, 1/40, 1/80 (red) and 1/160. . . . .	113
3-12	STRUCTURAL INSTABILITY. The onset of the most correlated state on compliant (1/80) PDMS is also accompanied by holes that open up in the sheet, which can grow in time. (A) 10x, (B) fluorescence image of E-cadherin on a 1/80 PDMS sheet. On the same sample, local tension induces these instabilities, which retain functional E-cadherin around the circumference (C) fluorescence, (D) brightfield. . . . .	114
3-13	SHEET REMAINS FLAT. (A) 25x, 3D image of stained nuclei on nearly pure prepolymer (1/200). For long times, the cells retain their sheet-like character, although scattering is possible by moving underneath other cells (3D reconstruction and contour plot, B). . . . .	115
3-14	3D MORPHOLOGY FOR DIFFERENCE STIFFNESSES. Cells on non-compliant surfaces, $ G  >  G^* $ , (A) are spread, while cells on compliant surfaces, $ G  <  G^* $ , (B) create long projections and have less interfacial area with the surface (grid = $2\mu\text{m}$ ). . . . .	115

3-15	CONTROLS FOR THE VAN HOVE CORRELATION FUNCTION. Dynamic Monte Carlo simulation (A) of the same size image as most experiments, (D), at high density yields the RDF in (B) and spectrum in (C). . . . .	116
3-16	FIBRONECTIN ADSORBED TO PDMS. (1) 0.4 mg/ml, (2) 0.2 mg/ml, (3) 0.1 mg/ml stained fibronectin on 1/10, 1/60, and 1/160 PDMS, spun onto Mattek dishes. On the 1/10, and 1/60 PDMS, the fibronectin is rigidly adhered. On the 1/160 plates, where the PDMS is nearly purely viscous, the fibronectin does not stick, and instead is diffuse across the plate. . . . .	117
3-17	DYNAMIC INSTABILITY. On compliant substrates, ( $1/80$ ), the sheet will slowly begin to aggregate. This results in the deformation of the substrate over millimeters (A). Structural inhomogeneities appear during the collapse, such as the appearance of holes in the sheet, and invaginations (B,C). . . . .	118
4-1	STAMPED FIBRONECTIN. 1mg/mL Fibronectin transferred non-specifically to 1/10 PDMS spun onto a Matek dish, and stained with 1ug/ml FITC-pig skin collagen. . . . .	122
4-2	CELLS BOUND TO STAMP. Brightfield image of Mouse Mammary Epithelial Cells bound nonspecifically to 1/10 PDMS. . . . .	122
4-3	LOW DENSITY CELL POPULATION. 1/10 PDMS treated with 5 min $H_2O_2/HCl$ , 10% PEG-amine, to generate the reactive/passivated surface. 1mg/ml fibronectin added to stamp and transferred. Mouse Mammary Epithelial Cells bound, and stained with 1/1000 CMFDA. . . . .	131
4-4	LOW DENSITY CELL TRAJECTORIES. Trajectories of cell movement on stamped pattern for the low density system. Low density epithelial cell populations under confinement are marked for their adherence to the boundaries, and high speed. . . . .	132

4-5	HIGH DENSITY CELL POPULATION. High Density of Cells, identically treated as 4-3 . . . . .	132
4-6	HIGH DENSITY CELL TRAJECTORIES. Trajectories of cell movement on stamped pattern for the high density system. More highly dense systems also show preferences for the boundaries, although the effect is significantly less pronounced than the lower density. . . . .	133
4-7	PROBABILITY DENSITY FUNCTION FOR CELL VELOCITIES (LOW). Probability Density Function for the velocity of cell trajectories in low density populations with diameters 50 $\mu\text{m}$ (red), 150 $\mu\text{m}$ (gray), and 250 $\mu\text{m}$ (black). Each overlaps, and contains the same non-gaussian character, and slight fast subpopulation. . . . .	133
4-8	PROBABILITY DENSITY FUNCTION FOR CELL VELOCITIES (HIGH). Probability Density Function for the velocity of cell trajectories in highly dense populations with diameters 50 $\mu\text{m}$ (red), 150 $\mu\text{m}$ (gray), and 250 $\mu\text{m}$ (black). Each overlaps, and contains the same non-gaussian character, and slight fast subpopulation. . . . .	134
4-9	MUTUAL CORRELATION FUNCTION FOR SEPARATE POPULATIONS. Mutual Velocity Correlation Functions for the separate populations as defined by the spatial patterning. This function isn't really valid above the half-width of the patterns, which is 50 $\mu\text{m}$ , but nevertheless, illustrates an important conclusion. There is no real difference in the level of correlated activity. (red: 50 $\mu\text{m}$ inner radius, yellow: 150 $\mu\text{m}$ inner radius, green: 250 $\mu\text{m}$ inner radius, blue: 350 $\mu\text{m}$ inner radius. The modulus of the PDMS is 492.2 Pa, with $G''=154.5\text{Pa}$ , and $G'=470.2$ . . . . .	135

4-10	STIFFNESS ALTERATION BY OXIDATION?. Twelve minute plasma oxidation of a 1/10 PDMS surface, and subsequent non-specific stamping of fibronectin (A) 10x Fluorescence image of the fibronectin, (B) brightfield 5x image of cracks throughout the dish. Stamping on surfaces of different stiffness was not pursued, largely because we were unsure whether or not by oxidation of the PDMS surface, we were altering the stiffness as well as the chemical composition. Then we have both the effect of the covalent attachment as well as the stiffness to contend with when analyzing the movement of the cells. . . . .	136
4-11	ACTIN CONTRACTILE BUNDLES IN PSEUDO PURSE-STRING. 1:200 rhodamine-phalloidin was used to stain the filamentous actin bundles in a pattern of mouse mammary epithelial cells. It shows that there is a large concentration of actin bundles arranged radially, and preferentially towards the center and the inner diameter of each ring. Thus, the formation of these bundles is not dependent upon the wound, as in the "purse-string" closure of a small wound, but is sufficiently explained by free space. . . . .	136
4-12	10x image of fibronectin stamped onto two separate samples, PDMS surfaces of a crosslinker/prepolymer concentration 7/400. The surfaces were treated as described above, with FITC-Pig Skin Gelatin as contrast. Collagen is good as a contrast agent, but also adheres cells more quickly than fibronectin. This can be a valuable parameter, as even given the cell exclusion chemistry, the longer that cells sit on the surface, the more likely it is they can still bind the surface where you do not want them. . . . .	137

5-1 DYNAMIC SUSCEPTIBILITY. Using a technique quite common to granular physics, we seek to identify timescales involved with the exchange of neighbors. As cell monolayers that move uniformly versus those that scatter may have the same magnitude of their velocities, we wanted an order parameter that would be able to distinguish between the two. Here, we show the results of three simulations. In the top row, there is a crystalline system with low displacement, and nearly no neighbor exchange. Therefore the order parameter barely dips, and there is no identifiable timescale by the susceptibility parameter,  $\chi$ . As the temperature of the system is increased (middle row), there is now a finite timescale, as thermal energy is sufficient to drive the scattering of each of the particles. Taking the same density, but biasing the movement (bottom row), we get the the magnitude of  $\chi$  decreasing, reflecting the increased uniformity, as each cell has a preferred motion. As this system could not be easily compared across densities, we opted for just the mean cosine as a superior method. . . . . 150

5-2 DYNAMIC SUSCEPTIBILITY PREDICTS A SECOND ORDER TRANSITION. The location of the peak in the  $\chi$  parameter,  $\tau^*$ , for the movement of monolayers on substrates of varying viscoelasticity predicts the same transition as does the divergent power law lengthscale calculated in Chapter 2, from the 2pt. velocity correlation function. The parameter  $\zeta$  is identical to  $\alpha'$  from Chapter 2, but only for very high densities. . . . . 156

5-3 DIAGRAM OF MUTUAL 2PT CORRELATION FUNCTION. The correlation function whose power law exponent is used to outline the transition from uncorrelated to correlated behavior, is taken as the product of the velocities in the directions that connect them, in the radial, perpendicular direction. . . . . 156

5-4	DIAGRAM OF THE RADIAL DISTRIBUTION FUNCTION. Each cell is at the origin of its own radial coordinate system. In successively larger intervals, at a distance, $r$ away from the origin, the density of cells is counted. This function is solidly periodic for crystalline materials, oscillatory for weakly interacting or dense systems, and flat for non-interacting and very low density systems. . . . .	158
5-5	HARD DISK TRAJECTORIES. Trajectories of 300 hard disks. The potential is either 0 or infinity, and are walked around a lattice, and captured at 80 time points. . . . .	158
5-6	VAN HOVE CORRELATION OF HARD DISK SYSTEM MIMICKING CELL MOVEMENT. We use dynamic monte carlo simulations to reproduce cells in the same quantity and with the same dimensions as the cells we image at 25x. After collecting the trajectories of each <i>in silico</i> cell, we can calculate a control for the van Hove correlation function. At $\tau = 0$ , there is significant order, out many cell diameters. This correlation is lost quickly over time, however. . . . .	159
5-7	VAN HOVE CORRELATION OF LENNARD-JONES SYSTEMS MIMICKING CELL MOVEMENT. Lennard-Jones systems make use similar short-range exclusion as hard disk systems, but also have a very long ranged attraction. Using the canonical ensemble described in Chapter 8, we can lower the temperature to see the emergence of long ranged correlations in the van Hove correlation. . . . .	160
5-8	THE DYNAMIC STRUCTURE FACTOR FOR THE HARD DISK SYSTEM. The two-dimensional fourier transform in time and space peaked at $2\pi/0.35 = 18 \mu\text{m}$ , the diameter of a single hard disk. . . .	161
5-9	THE STATIC STRUCTURE FACTOR FOR A SHEET ON A VISCOELASTIC SUBSTRATE. The fourier transform of the radial ditribution function, showing a peak at the principal cell-cell spacing. This is the only relevant lengthscale. . . . .	162

5-10	THE DYNAMIC STRUCTURE FACTOR FOR A SHEET ON A VISCOELASTIC SUBSTRATE. The same two-dimensional fourier transform was calculated on the van Hove correlation function calculated for the movement of cells within a plane, for every separation distance $r$ , between cells, and every elapsed time, $\tau$ , during the timecourse of the imaging. There are no significant collective modes, what would be seen as diagonals in the Dynamic Structure Factor. The only peaks remain for most time, and represent the characteristic lengthscales of the separation distances between cells. . . . .	163
5-11	2PT VELOCITY CONTROL. The $C_{rr}$ has a $1/r$ decay, and the magnitude is much greater along the mutual direction that connects two beads, than in the parallel direction, or crossing parallel and perpendicular. . . . .	164
5-12	MEAN-SQUARED DISPLACEMENT FOR SINGLE ENDOCYTOSED PARTICLES. $0.5 \mu\text{m}$ rhodamine coated, carboxylated, internalized microspheres were imaged over 60s in mouse mammary epithelial cells cultured on coverslips. Each line is a separate microsphere, located in a distinct local mechanical, microenvironment. . . . .	168
5-13	ENSEMBLE AVERAGED MSD FOR CELL ENDOCYTOSED PARTICLES. $0.5 \mu\text{m}$ rhodamine coated, carboxylated, internalized microspheres were imaged over 60s in mouse mammary epithelial cells cultured on coverslips. The plot is the ensemble average of all of the different microspheres, so that we might fit it to a power law, and calculate the mean diffusivity of the particles. . . . .	168
5-14	POWER LAW SCALING FACTOR FOR MSD. At short times, the embedded microspheres are often confined by the cellular cytoskeleton, and thus are "sub-diffusive" ( $\alpha < 1$ ), unable to sample space at the rate that is expected by diffusion. As more time elapses between frames however, the bead is able to break free, and diffuse freely ( $\alpha \sim 1$ ) . .	169



5-15	FREQUENCY-DEPENDENT SHEAR MODULUS FOR MOUSE MAMMARY EPITHELIAL CELLS. From the MSD, the particle size, and the temperature, we can calculate the frequency-dependent shear modulus. $G'$ is the loss modulus, an indication of how the cell stores elastic energy that is applied. $G''$ is the loss modulus, what indicates how the cell dissipates energy applied to it. Clearly from this figure, we can see that for nearly all timescales, the cell is more viscous than it is elastic.	169
5-16	MEAN ELASTIC MODULUS FOR DIFFERENT EPITHELIAL CELLS. Mean Elastic Modulus, for both mouse mammary epithelial cells, as well as Caco-2 colon epithelial cells. The mean Elastic modulus for the mammary epithelial cells, what we use throughout the experiments in this thesis, is $0.5631 \pm 0.0903$ Pa, or $5.631 \text{ dyn/cm}^2$ ( $n=3$ ). The mean Elastic Modulus for the colon epithelial cells, which are more likely more similar to the intestinal epithelium, to which we draw many analogies, is $0.1915 \pm 0.0464$ Pa, or $1.915 \text{ dyn/cm}^2$ ( $n=3$ ). Both measurements are taken at 1 Hz.	170
5-17	BEADS IN GLYCEROL. $1 \mu\text{m}$ beads in a 50:50 mixture (by volume), imaged over 100 seconds. The trajectories are color-coded, with dark being old, and light colors being more recent.	170
5-18	MEAN-SQUARED DISPLACEMENT FOR A 50:50 GLYCEROL/WATER MIXTURE. Perfectly linear scaling for the MSD, over nearly all timescales. The only limitation is the ability to track the beads for every frame, as the beads can diffuse out of the plane.	171
5-19	POWER LAW SCALING FACTOR FOR GLYCEROL MSD. The mean-squared displacement scales as $\tau^{1.0}$ for nearly all timescales, confirming that all motion is strictly diffusive.	171
5-20	VISCOSITY OF A 50:50 GLYCEROL/WATER MIXTURE. The viscosity of the 50:50 Glycerol/Water mixture is $\sim 3 \text{ mPa s}$ , as measured in <i>Properties of Ordinary Water-Substance N.E. Dorsey, p. 184., Hafner Publishing Co., New York (1940)</i> .	172

8-1	Particles occupy right side, membrane ruptures, and the volume available to the system has increased . . . . .	212
8-2	Length versus time traces of the RNA hairpin at various constant forces in 10 mM Mg21 . . . . .	220

# Chapter 1

## Introduction

### 1.1 *In vitro* models of Sheet Motion

The canonical description of cellular motility is defined at the level of a single cell, in the protrusion, contraction, and detachment of membrane lamellipodia or filopodia [8, 9]. The intracellular machinery that drives the cell forward is largely actin, coupled with the stabilization of dynamic, multiprotein plaques at the surface, called focal adhesions. There is extensive knowledge of the mechanisms involved - the key intracellular molecular components, both in terms of the proteins that link together to comprise the machinery, as well as the molecules responsible for the signaling cascades that drive the system forward. The morphologies of migrating cells have been detailed in a wide variety of cell types, for varying conditions and dimensionality, from the flattened to the amoeboid [9]. In addition, there is large and growing knowledge of the external, physico-chemical factors that modulate adhesion. The adhesivity of the surface, as defined by the receptor-ligand binding affinity [10], or the quantity and availability of surface ligand, is a principal variable. The mechanical properties of the substrate, the time-dependent deformation characteristics have also emerged as influential in the determination of movement [11, 12, 13] and geometry [14, 15]. Cells also respond to gradients in these parameters. Spatial asymmetry in the surface localization of adhesivity [16, 17], as well as in the compliance of the surface itself [18, 19], will induce asymmetry in motion, with preference for the more adhesive and

the less compliant (following a bimodal relationship).

Thus, despite the abundance of detail in the mechanisms that determine single cell motion, little is understood of how coherent patterns of movement can emerge when they migrate as groups. It is still unclear how the introduction of cell-cell contact contributes explicitly to coordinated movement *en masse* in any of the aforementioned scenarios, despite the ubiquity and importance of this phenomenon in a wide variety of physiological processes, from development in the embryo, to regulation and homeostasis in the adult. Equally as varied, are the manners in which the sheets have been observed to move. In embryonic development, epithelial sheet fusion occurs in the ventral enclosure of *Caenorhabditis elegans* [20, 21], and dorsal closure of the *Drosophila* embryo [22, 23, 24, 2]. In certain wounded scenarios, such as in the stratified epithelium of the cornea [25, 26, 27], cells have been shown to slide as a contiguous sheet [27]. In normal adult tissue, the unobserved (but experimentally verified) uniaxial movement of the intestinal epithelium constitutes the fastest turnover of tissue in the body [28, 29, 30]. Thus, the coordination and self-similarity in the movement of cells in each of these cases is extraordinary, despite (or perhaps because of) the retention of their cell-cell contact.

The cell-cell contact in epithelial tissue, for example, is moderated by E-cadherins, calcium-dependent transmembrane proteins that are anchored intracellularly by actin-based *adherens* junctions [31]. These junctions are belts of filamentous actin, around the periphery of each cell, which is known to provide the structural integrity of the cell (cadherins are also bound to hemidesmosomes, which are anchored to intermediate filaments, with less well studied physical properties). Given that each cell is adhered to each other by these strong interactions, yet they each have their own focal adhesions that drive locomotion, how does one influence the other? It has been shown that increased expression of E-cadherin slows the migration of *in vivo* epithelia [32]. Although, it has also been associated with a reduction in proliferation and an increase in apoptosis. As a result, its contribution to the dynamics of the sheet has

still not been isolated (nor imaged directly, as these are based on histological studies of sacrificed mice). Thus far, efforts to understand collective migration of epithelial cells at all, limit themselves to (1) characterizing the extent that the movement is collective (tracking cell motion in time, then using mathematical analyses to quantify its correlation), and (2) correlating movement to distinguishing morphological characteristics. And, as the predominant method for inducing coordinated sheet motion is through the denudation of confluent sheets in culture, *in vitro* efforts center on the role of free space and cell damage in inducing it[33, 4].

### 1.1.1 Wound Healing

As previously stated, the predominant method for generating coordinated group motility in culture, is by denudation of space, such as what is found in the classical wound healing assay. The most common method for wounding, is to physically scratch the surface denuding the sheet (Figure 1-1), and cells on either side of the scratch will move to close the gap. The cells in the front of the denuded sheet, called the leading edge, produce large, clear actin-based extensions that actively search their environment, and are extended in the direction of the edge. The cells behind the leading edge, termed sub-marginal cells, are still confined, and have only been shown recently to extend mild lamellopodium along their basal surface in between their neighbors, in the direction of the wound[34]. Thus, there is massive, coordinated motion along the leading edge, but it does not penetrate deep into the rear of the sheet. In an alternative, mechanistically distinct method, when the wound in an epithelial sheet is small and circular, closure proceeds by what has been called an actin 'purse string' (Figure 1-2), [2]. During this event, the cells at the periphery of this small wound, organize large actin filaments that extend around the circumference of the wound. These filaments are anchored by the adherens junctions, and are linked between cells by cadherins. Thus, short range coordinated movement in this sense is mediated by lateral junctions, and contractions that extend further than the lengthscale of a single cell. As both processes involve the physical denudation

of the sheet, from these techniques it would be impossible to know with certainty whether the movement resulted from the opening of free space, or from the induced cell damage, and release of factors into the medium, or through gap junctions, the intercellular communication channels. Thus, while there is coordinated movement, and cells all move perpendicular to the direction of the wound to initiate closure, causality is obscure, and there is an inconsistency with what should exist in the natural epithelium, that cells in the rear (which are in the vast majority of the population) are not very motile. Nevertheless, this is the standard model, as this is the only method (or its variants, described below) in culture that is known to force cells to move in a directed, uniform direction (after previously moving randomly) or "break symmetry".

### 1.1.2 Model Wounds

As an attempt to address this 'damage vs space' dichotomy, other studies have focused on creating removable barriers to denude the sheet, thereby creating a 'model wound'. Either by the placement of non-adhesive PDMS blocks, or by the removal of stencils (Figure 1-4), various studies claim to be able to discern that the onset of collective migration is sufficiently explained by the availability of free space. By these methods, the implication is that if scratching can be avoided, then there will be no induced damage, and no signal to instruct the sheet to migrate forward. This assumption is inherently flawed however, as will be shown in the chapters that follow, that these methods still do induce damage - only less. The application of physical force to remove cells, will always result in the induction of some kind of signal, either by the death that results, or by the transmission of physical force into a variety of known mechanotransduction signals among the remaining viable cells. Therefore, the issue of free space as it pertains to the onset of collective migration remains unsolved, given that we assume it is a parameter relevant to *in vivo* studies. Further, these studies still suffer from the latter of the two aforementioned issues, which is that submarginal motility is still not explained.

As there is an apparent lack of submarginal motility, some studies have tried to conclude that this is due to a lack of traction, by experimentally measuring the migration-induced deflection of high density arrays of micro-fabricated pillars[35]. This is a similar approach to the 'denudation models', explicitly using the default assumption that sheet motion must be entirely based on traction against a non-compliant substrate. They compare the traction exerted by isolated cells and cells within a sub-confluent monolayer. As expected, cells within the monolayer exert less traction than isolated cells - completely confluent cells exert none (compare to fully confluent, polarized epithelia). Moreover, the tractional stress is greatest at the cell edge, both of an isolated cell and cohered cell at the boundary. This is consistent with other experiments that measure the speed of cells in the sheet and at the edge [33]. These results are not surprising, as they mirror what is observed by imaging the denudation models. The leading edge cells have actin-based searching machinery, which is clearly visible by light microscopy. The cells further towards the rear do not appear to have similar machinery. However, this experimental system is extraordinarily relevant, in that it sums up the assumptions and inadequacies of the models before it. It makes most clear the central assumption of each of the models that (1) the denudation of space on non-compliant surfaces (continuous or not) is required to induce motion, and (2) that traction of all or part of the population is the principal physical mechanism for that motion.

The explanation for this lack of movement, which is put forth explicitly in the micropillar study, but inferred in many others, is that the cells are in a dynamic balance of pushing and pulling, and therefore there is no net movement on these epithelial islands suspended by pillars. Inverting this inference, the denudation models would therefore have a net movement, because now there is an imbalance. The implicit arguments of each of the above studies, is that only this imbalance breaks symmetry (i.e. post denudation). However, as we understand that whether we are talking about the contiguous sliding of a wounded cornea, or the renewal of the intestine, motion is required from more than just the first couple of rows of cells. Thus net movement is

achieved over long lengthscales, presumably much longer than what can be accounted for by an imbalance in physical cell contention. This being the case, moving forward, we can accept reduced submarginal motility and either continue to *force* an analogy of this model back onto *in vivo* scenarios, or abandon the model system that causes this migratory phenotype in the first place.

To expand on the second assumption in the aforementioned studies, what encourages the idea that cells are in a dynamic state of pushing and pulling, is the assumption that cells in a sheet will migrate using the same mechanism as single cells - only together. They are either in contention, or they cooperate. Free space makes them cooperate, because as the imbalance at the leading edge encourages those cells to walk forward, the cells in the rear can move in step. And, while this may be true for the situations in which they are currently observed, where traction against a non-compliant substrate is the only option for coordinated migration, there is sufficient reason to doubt this as an *in vivo* mechanism. First, we expect longer lengthscale migration than what denudation yields. Further, there is a discrepancy between morphologies that we see *in vivo* (often columnar *in vivo*, spread in culture; Figure 1-9), with those that we see in these experiments. From a separate perspective however, there is doubt, because there are a variety of additional variables that these methods view as obstacles to movement, foremost among them being cell-cell contact (i.e. constraining cells that desire autonomy, causing no net motion). Thus, to explain the movement of tissue, we should depart from these models, and focus on what makes it tissue, which is the multicellularity from the cell-cell contact.

### 1.1.3 Cell Sorting

Along this direction, for studying movement of the epithelium as tissue, we draw our nearest analogies to embryonic development, where tissue movement is in part explained by the competition between cohesion and adhesion, the tensions generated between cells versus those generated at the cell-matrix interface. This phenomenon



is detailed by the differential adhesion hypothesis (DAH)[36, 37, 38], which generally states that mobile cell aggregates organize themselves and move in order to minimize their interfacial free energy (Figure 1-3). This has appropriately described the equilibrium spatial distribution of initially heterogeneous cellular aggregates by the differential expression of **cell-cell** adhesion molecules - a perspective which accurately captures the role of cell-cell contact in the spatial integration of varied adhesive stresses that drive non-equilibrium movement (e.g. sorting) on the way to the equilibrium structure. In experiments on mixed populations of neural retinal and pigmented retinal cells, over time, cells in the mixed population will aggregate with their own cell type, in the end sorting and recovering the two original tissues [3]. Each cell type has different cell-cell adhesion receptors which prefers homophilic interaction, and thus by the DAH, cells search space in preference of self, minimizing their own free energy. What is particularly notable, and further underscores the role of cell contact in largescale movement, is that this movement can still occur in the absence of a functional actin cytoskeleton. When cytochalasin B was added to the initially mixed aggregate, all filopodia and pseudopodia, the actin 'search' machinery described earlier, is ablated, and the mixtures are left with only their mutual cell adhesions, and random fluctuations in shape. Still, these two populations sorted, although the sorting was incomplete. The cell populations never fully reach the configuration observed before their ability to search actively was eliminated. In polarized epithelia, there are also no distinguishable pseudopods or membrane ruffling, and so either active search does not exist, or at the very least, it does not exist in the same form. Thus, there is a cell-cell mediated phenomenon, not dependent on (although facilitated by) actin-based motility, that can account for large scale coordinated motion. Noticeably, this type of coordinated motility is within a cellular aggregate, and not on a non-compliant substrate. While the conceptual framework for differential adhesion has been presented as a description of cell sorting in heterogeneous aggregates, we merely use this as a springboard to motivate a simpler extension of this theory, that cell-cell contact may play an elevated role in coordinated cell motion of the epithelia (cornea, kidney, colon, etc) rather than being a connection for pushing

and pulling, that it contributes (in the previous example energetically) to the movement of cells over long timescales and long lengthscales. I therefore use this general relationship, the mechanical balance between cell-cell and cell-matrix adhesions (preference towards the former), as the primary target for measurement in our studies of the mechanics of the epithelium, using the intestinal epithelium as a reference system.

The intestinal epithelium is a cellular monolayer that is folded into crypts and villi that form invaginations and projections into the intestinal lumen for the purpose of absorbing nearly all of the body's nutrients (Figure 1-8). Roughly half of the cells in the intestinal tract rapidly proliferate at the bottom of the crypt, and migrate against the basement membrane (Figure 1-5) to the top of the villus, while they mature into either absorptive or secretory cells. At the tip of the villus, mature cells undergo apoptosis [39], completing a lifecycle on the order of  $\sim 3.3$  days for mouse ([40]). In this time, cells move at roughly 1-1.5 cell diameters per hour, ranking them among the most motile cell types, renewing the lining of the intestinal epithelium faster than any other tissue. Further, the importance of this movement as a physical process is underscored by the fact that they are all mutually adherent. They migrate collectively, forming and breaking adhesions with the basal lamina and each other in a way that characterizes a motile sheet. Astoundingly, this non-equilibrium process is stable, as the rates of proliferation, predominantly at the bottom of the crypt, balance the cell death that occurs at the tip of the villus. The motility of cells is precisely balanced with their lifecycle, to generate a dynamic equilibrium state. Thus, this presents an interesting model for migration (and reference for our experiments), as it has coordinated, directed movement of a monolayer, with no wounds, and a unique combination of boundary conditions intricately tied to the movement itself.

## 1.2 Summary of Open Questions

While there continues to be debate in the epithelial cell motion community regarding the mechanisms of coordinated migration surrounding *in vitro* models of wound

healing, there has been a separate community that has been exploring from a more biological basis, the concerted movement of *in vivo* epithelial cells for decades, in particular of the intestine. Their analyses have focused more on intercepting causal roles for adhesion and cell-contact in the movement of contiguous sheets *in vivo*, by alteration of the expression profile of key molecules (i.e. E-cadherin), and the manipulation of cellular processes (i.e. cell division). From this, they have generated an almost orthogonal set of hypotheses for group sheet motion (contrary to the traction-based push/pull dogma from *in vitro* wound healing literature), unavailable to be tested by the contemporary, aforementioned *in vitro* analyses. Thus, in my work I address some of these hypotheses, by incorporating some of their *in vivo* tests, into my *in vitro* experiments.

The most predominant conjectures for mechanisms behind the movement of the intestine are summarized by J.P.Heath in an article entitled: *Epithelial Cell Migration in the Intestine*, [29]. They are listed here, with an editorial on their physical plausibility.

(1) Basement membrane flow. The basement membrane, the thin, network of fibrous protein to which the epithelium adheres, is itself produced by cells, and passively moves upwards, displacing the sheet.

On its own, this argument is hardly plausible, given that the basement membrane is not active, nor is it likely to support the stresses required to displace the epithelium. Further, anti-laminin antibodies that were introduced into the basement membrane showed no net movement [41]. However, we are still interested in this potential mechanism, as the sheet may be destabilized with respect to the basal lamina, and not firmly adhered to it, serving as somewhat of a lubricant, so that stresses between cells are not dissipated through the basal lamina. We motivate this possibility as various diseased states (i.e. epithelial sheet detachment in diarrhea) support the idea that the sheet and basement membrane are separate entities, and cells are not rigidly

adhered in an individual fashion, but slide with respect to each other or a common, third substratum (i.e. lamina propria).

(2) Mitotic Pressure. Noticing that there is a specific asymmetry along the crypt-villus axis, with movement away from where cells divide (towards the tip), encourages the hypothesis that it is the force of division that pushes on the other cells, moving them forward, towards the tip of the villus [42]. There is little known regarding the actual forces involved in mitosis, although the potential for displacing neighbors may in fact be possible, but not likely if also adhered to a rigid, non-deformable substrate.

The hypothesis that cell division generates localized pressure gradients and displaces the sheet also contradicts the idea that the epithelial sheet is rigidly adhered to the substratum. Pressure gradients should be transmitted to the substrate, not other cells if they maintain stable basal adhesions. A pressure gradient as the inspiration for motility has its own inconsistencies however. Foremost among them, is that the lengthscales associated with movement are much larger than the lengthscales that can be expected to transmit stress in a viscous, dissipative medium (as there is plenty of evidence as to the viscoelasticity of biological matter). Thus, we question the necessity of the stability/contractility dogma of cell migration in light of the physical paradox it presents, as well as its compatibility with how to transmit stress in a fashion capable of translating a sheet over long lengthscales. To this point, there is also an apparent lack of actin-based extensions in polarized epithelia from *in vivo* histological sections, such as what is found in the digestive tract, kidney, and glands such as the thyroid.

(3) Active Movement. In the event that there is no higher order movement, either the *en masse* displacement of the sheet by division, or movement of the substrate itself, the remaining argument is that the cells walk autonomously, but do so in an extraordinarily coordinated fashion. This is the default hypothesis, as this is what we know from the *in vitro* analyses, on non-compliant substrates (i.e. denudation

experiments). This hypothesis is not fully accepted however, again, due to the lack of the traditional markers of single cell motility that are observed by histological sections. For example, cells of the intestinal epithelium are columnar, and therefore do not appear to have the same actin-based extensions that are used for search space, such as lamellipodia and filopodia (1-9) These are hallmarks of the "central dogma of cell migration" (protrusion, adhesion, contraction) as we understand it from cell culture. Among the issues that remain unsolved and perplexing regarding the coordination of cell movement, are how they negotiate their adhesions with the surface, while maintaining their contacts with each other. From single cells, we know that on what are traditionally called soft surfaces ( $< 1\text{kPa}$ , but depending strongly on cell type), adhesion complexes are transient - their formation involves the recruitment of individual molecules to localized regions at the cell surface which bind the substrate in a tension-dependent manner (Likewise, as cell adhesions are destabilized on soft media, they are known to not only migrate, but are highly motile ( $\sim 10\mu\text{m}/\text{hour}$ )). Surfaces that cannot support tension are therefore weakly adherent, and cells are only lightly tethered, incapable of spreading or generating traction for movement [43]. In contrast, stiffer substrates ( $> 1\text{kPa}$ ) sustain stable adhesions, which encourage cells to spread over the surface to minimize their own adhesive free energy or actively search their environment with actin-based contractile machinery. While it is not known whether or not the basal lamina that most non-stratified (single layer) epithelial cells interface with pertains to the regime where adhesions are stabilized or destabilized, there are a number of arguments that can be made that long lengthscale, correlated motion likely occurs in preference of a destabilized state (monolayer and lamina are somewhat separate), and therefore cells within the sheet must depart from the canonical description of cell motility. They generally hinge on the issue of how stresses can propagate through elastic and viscous media. The complexity is further compounded considering the stability of both adhesions is balanced in a fashion that presumably facilitates movement of the sheet and within the sheet.

### 1.3 Summary of Testable Hypotheses

To summarize the previous section, the modern *in vitro* denudation assays as models for *in vivo* sheet movement share few similarities with what is known (however little) of *in vivo* sheet movement (i.e. submarginal motility). Further, aside from their applicability, it is still unclear what drives the motion specific to these models (i.e. free space vs cell damage). A separate set of hypotheses for *in vivo* motion of the intestine, may provide additional insight into designing *in vitro* experiments that more closely resemble *in vivo* motion. These include the influence of the substrate (in an active role) as well as the role of cell division. Thus, we first begin by resolving some of the outstanding issues with the denudation models, and then explore coordinated migration of an epithelial sheet guided by the hypotheses put forth by Heath and others [42, 29].

1) Wounds and 'model' wounds are the accepted standard for reproducing coordinated sheet motion. While we later refute these as models as appropriate for representing *in vivo* scenarios, we can first attempt to resolve their internal issues. Assuming that the current wound, or 'model' wounds are acceptable, how do we separate the influence of free space from cell damage and signaling on migration after denudation?

The denudation models accept the third argument made by Heath. In the absence of any contiguous sliding, folding, or other higher order movement, it may be that each individual cell is propelled only by its own cytoskeleton and adhesions that are made with the surface, and cells just coordinate their steps in a very finely regulated fashion. Again, while this is possible, it would be hard to verify, as from standard histological sections (Figure 1-6), we do not see the standard actin based projections that accompany fast movement. Nevertheless, on soft matrices, we understand that basal adhesions are destabilized, and thus focal adhesions are smaller, and may not be easily seen by standard imaging methods.

We approach the creation of this damage free denudation by the use of multi-phase flow in microfluidics. Microfluidics allows us to take advantage of the ability to both culture epithelial sheets inside microfluidic channels, as well as precisely control the temporal and spatial properties of the fluid. Thus, we introduce the first non-physical denudation method, which is cleavage of a portion of an epithelial sheet by the localized delivery of trypsin, the same enzyme solution used for passaging cells. This is flowed side-by-side with regular media, and the fluids do not mix over short lengthscales, and thus we can selectively remove cells, without inducing any cell damage. Then, by brightfield and fluorescence microscopy, we can watch remaining cells recover the free space. Again, this is to address the unresolved issue of the origin of coordinated migration given the current models. We term the denudation an "Initial Boundary Condition" (due to the temporary open boundary across the sheet), and thus this study can be found in Chapter 2, entitled: Initial and Boundary Conditions in the Collective Migration of Epithelial Sheets.

2) The first of two primary arguments against wound and 'model' wounds is that it centers on denudation to break symmetry in the first place. Can symmetry be broken without introducing free space? An argument can be made for wounded scenarios, as there is indeed open space, such as in the epithelia of the skin and the cornea, but for non-damaged systems, such as the natural movement of the epithelia of the intestine, where there is none. Can we reconcile coordinated, directed motion, when there is no leading edge? Similarly, as the current models for reproducing sheet motion recapitulate movement only in cells nearest the free edge, is there an *in vitro* assay that can generate coordinated motion uniformly across the population?

To address this issue, we can revisit the first hypothesis outlined by Heath, that the basal lamina may play more of a role in facilitating the movement of the sheet than previously thought. The basal lamina, is a network of fibrous proteins, which from extracts and cellular secretions of extracellular matrix, we understand to be very

soft, with a gel-like consistency. It is possible that the mechanical properties of the substratum may contribute to the coordinated migration of the sheet, and therefore may be a new avenue for exploring symmetry breaking in the absence of free space. While there have been numerous studies that have looked the effect of cell motion on substrates of varying stiffness, first, these substrates are predominantly elastic, even with a very low shear modulus. To my knowledge, there have been no quantitative studies of confluent epithelial sheet motion on substrata that have a significant loss modulus (i.e. highly viscous). Thus, we propose that as it is known that cells on soft substrates do not develop strong, stable adhesions, this facilitates destabilization of the sheet with respect to the surface, and that simultaneous, strong cell-cell contact is responsible for movement within the sheet, in a fashion not unlike the sorting of aggregates, or the 'purse-string' closure of small, circular wounds (i.e. lateral tension as opposed to basal traction). Thus, in the experiments that follow in Chapter 3, entitled: Substrate Mechanics and Cell Contact in Epithelial Cell Motion, we show that the level of correlated cell motion is indeed a function of the viscoelasticity (emphasis on viscosity) of the substrate, and that as the shear modulus of the substrate decreases, cells are no longer making strong adhesion to the substrate, that the sheet is no longer stable as a sheet. It begins to slowly aggregate, and resembles sheet sliding.

3) The second argument, that mitotic pressure might drive the forward movement of cells by pushing, illustrates a much broader issue that is inferred repeatedly in nearly all the literature surrounding the movement of epithelial cells (in particular the denudation models). As previously stated, propensity for cells to push or pull each other has been cited as the reason why in wound or model wound experiments, that 'follower' cells, the ones immediately behind the leading edge (submarginal, but barely) can move. Some have implied that division at the rear contributes the density gradient that pushes cells forward. Thus, the basic question, of which the force of mitosis is only a small part, is that, is the displacement that we observe among cells in a sheet a result of pushing or pulling?



This hypothesis proposed by Heath and others ([29, 42]) is based on the asymmetry observed along the crypt-villus axis of the intestine. Cell division is localized to the crypt. There, cells do not move, and are known to reproduce to balance the apoptosis of cells that is localized to the tip. Based on this asymmetry, it might have been reasonable to assume that since cells migrate in the direction opposite to where they divide, that it is the force of division that pushes them there. There have been other studies that have shown that cell division is indeed not necessary for cell migration to occur ([44]), but this nevertheless highlights a large issue: is it possible that cells can be displaced by gradients in function or viability? There have been numerous studies that have been able to introduce asymmetry into the medium, or into the substrate. There is chemotaxis [45], haptotaxis [16], and durotaxis [18, 19]. They have been employed in order to understand migratory response to stimuli with spatial asymmetry. However, thus far, there are very few studies that create gradients in cellular function amongst cells as integrated into the same epithelial sheet. Again, drawing on analogies to the intestinal epithelium, within the same cohered sheet, there are a number of boundaries, including non-motile/dividing cells (base), motile/functional cells (middle), and apoptotic cells (tip). They encompass the entire lifecycle of the cell, of which migration is a key component. From the perspective of pushing and pulling, we are interested in one general question, if it is possible that a motile population may push or pull on a non-motile population. As in the the boundary between the middle and the base of the crypt. Thus far, no experiments have gradients in cellular function among cells within the same cohered population. Therefore, the present studies use microfluidics to recreate some of these gradients in cellular function, in order to evaluate how these conditions alter migration. We call these sharp gradients "boundary conditions", as we create interfaces in cellular function over a narrow range. These studies can again be found in Chapter 2. Although, our hypothesis is that in the absence of a compliant substrate, these gradients will not affect the migratory response of the viable/functional cells. The key ingredient to coordinated motion will be the ability to deform the substrate, which itself is significantly viscous.

Throughout each of these experiments, the end goal is to measure the dynamics of cell movement as a result of the applied boundary conditions and substrate mechanics, unifying the contemporary models of coordinated sheet motion with the hypotheses put forth by the biological community for how *in vivo* systems move. Thus, to add context to the dynamics that we measure (via tracking cell motion from fluorescence images), we also perform Dynamic Monte Carlo (DMC) simulations, where we recreate *in silico* cells, points on a grid that occupy a given size, and move at a predetermined speed, while obeying simple rules of thermodynamics and statistical mechanics (as outlined in detail in Chapter 7). This way, we can compare the dynamics of the *in vitro* system, with artificial systems, where we can, for example, add in the inter-particle potential ourselves. This is most useful in identifying what contribution to the dynamics of real cells is due to mutual exclusion. Hard Disk simulations, which have either a zero or infinite energy state, allow us to dissect the dynamics that arises from moving purely to avoid occupying the same space. Further, DMC simulations also serve as good controls, as we input the size and speed of cells, and thus we can be assured of the timescales and lengthscales that arise from the various correlation functions - functions that we use extensively on the actual cell motion (described in detail in Chapter 7 and 8).

## 1.4 Appendix

### 1.4.1 A note on adhesion in the intestinal epithelium

There are a number of adhesive gradients in the intestinal epithelium, not mentioned in the introduction, which we do not try and reproduce in our experiments. There are gradients in both cell-matrix adhesion molecules, as well as cell-cell adhesion molecules. Integrins and laminins for example (Figure 1-10) are known to be differentially expressed. We do not attempt to reproduce this however, because it is unclear if the *overall* adhesivity is differential across the crypt-villus axis. Laminins

1 and 5 for example, increase in expression towards the tip, but Laminin 2 decreases. Likewise, there is a similar problem with various integrins. Therefore, as we are not able to recreate so many simultaneous gradients, nor can we appreciate the magnitude of their expression levels and reintroduce them into a microfluidic channel in the first place, we decided to avoid this altogether.

E-cadherin is also known to be differentially expressed along the crypt (Figures 1-8, 1-9), which may contribute significantly to the motion of the sheet. Mediated by calcium binding, these homophilic molecules are known to modulate not only adhesion, but differentiation, proliferation, and signaling. Their expression is very low in the crypt region of the epithelium, and appears to increase with differentiation. Interestingly, beta-catenin, its intracellular binding partner in adherens junctions, is expressed equally throughout the basal lamina (1-8). As will be seen in the Chapters that follow, we indeed alter cell-cell contact, but do so with the introduction of antibody against E-cadherin. Thus, while we are interested in creating asymmetry in cell contact, the cost of doing is prohibitive, and we stopped at ablating all contact.

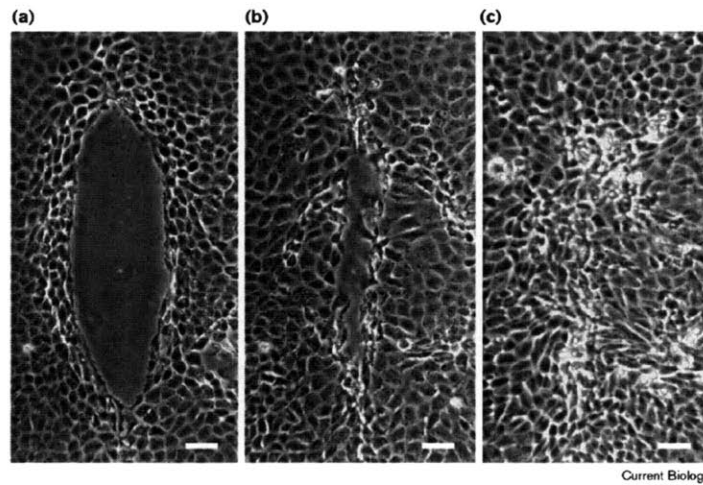


Figure 1-1: WOUND HEALING IN AN MDCK MONOLAYER. Wound closure in MadinDarby canine kidney (MDCK) epithelial cell monolayers. (ac) Phase-contrast micrographs of MDCK cells after wounding and microinjection with 2.5 mg/ml solution of OG dextran into the first three rows of cells around the wound margin (concentration in cells after microinjection is 1/10th that of the microinjected solution or 250 g/ml). Cells are shown (a) immediately after wounding and microinjection, (b) after 6 h, and (c) after 18 h. The scale bar represents 50  $\mu$ m. All figures for each treatment in this paper are representative of experiments performed in triplicate on at least three separate occasions (n=9). Figure and caption taken from [1]

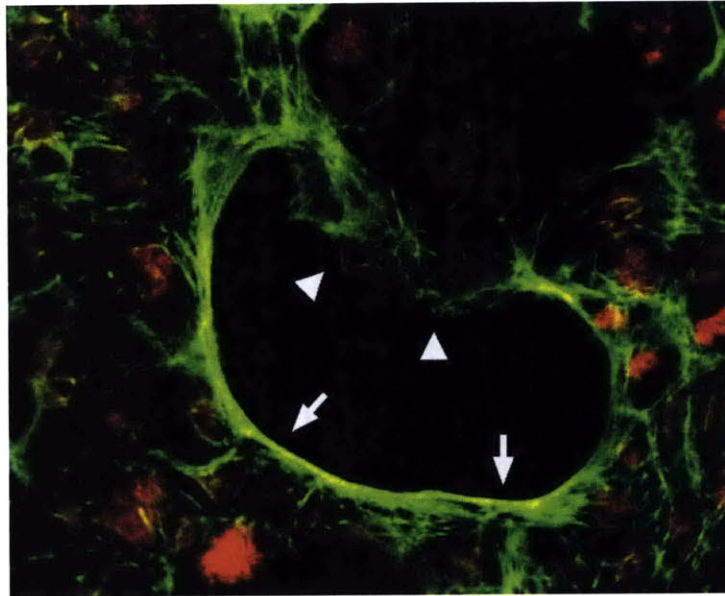


Figure 1-2: ACTIN PURSE STRING IN WOUND CLOSURE. Repair of in vitro wounds made in monolayers of the gut epithelial cell line Caco-2BBE is achieved by lamellipodial crawling or purse-stringing, or a combination of both. In this wound, one group of leading-edge cells is being drawn forwards by contraction of an actin cable (arrows), as occurs during embryonic repair, while other cells are clearly extending lamellae (arrowheads) and crawling forwards, as occurs during repair of an adult skin wound (image courtesy of J. Brock). Green staining is fluorescein isothiocyanate/phalloidin-tagged filamentous actin; red staining is the nuclear dye 7AAD. Image and caption taken from [2]

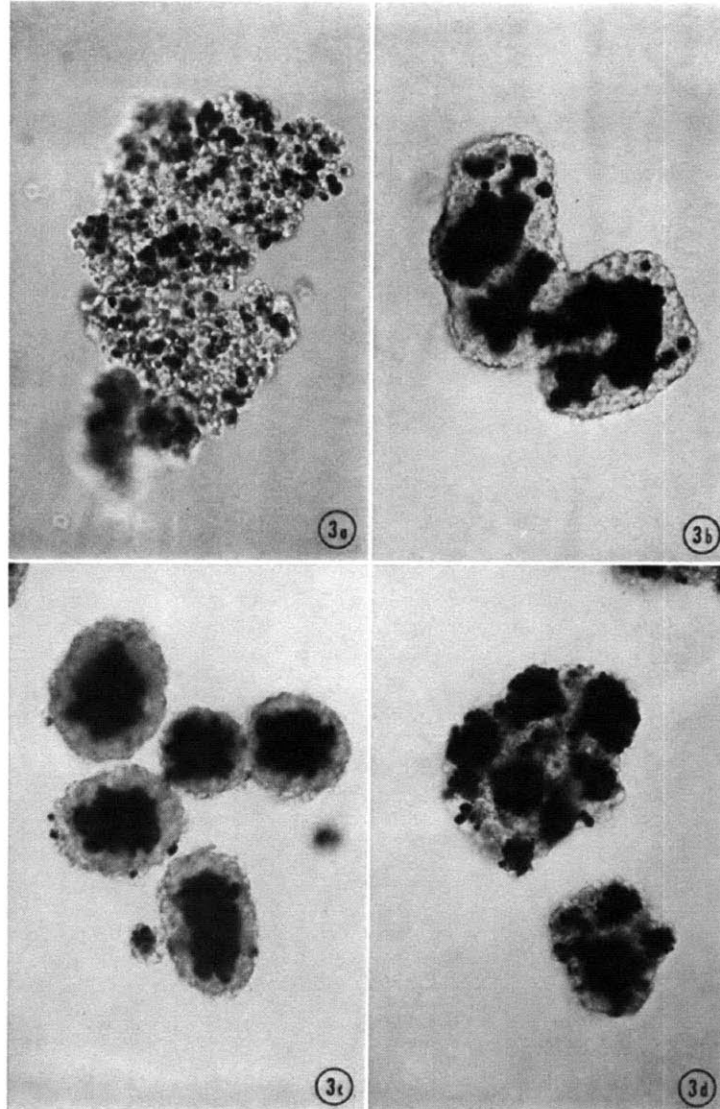


Figure 1-3: CELL SORTING. Sorting in mixtures of 7-day chick embryo neural retina (clear) and pigmented retina (black). (a) control culture after 2 hours (initial aggregate), (b) control culture at an intermediate stage of mixing, (c) complete sorting occurs in control culture after one day, (d) partial sorting occurs membrane ruffling and pseudopod formation are disrupted. Image taken from [3]

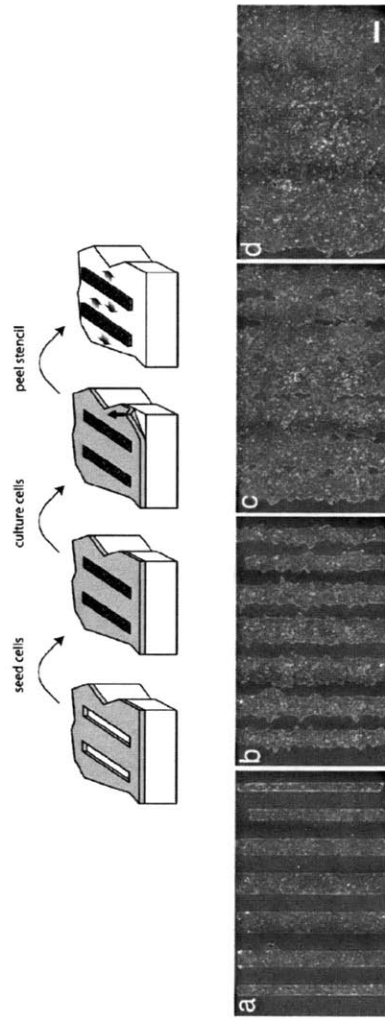


Figure 1-4: DIAGRAM OF "MODEL" WOUND. Thin PDMS films with holes in the shapes of long strips are placed on a cell culture surface, and cultured with MDCK cells (top panel). After the cells have bound, the film is removed, leaving behind cells exposed to a virgin surface. The cells then migrate out into free space (bottom panel). Cells are shown for (a) 90 minutes, (b) 13 hours, (c) 25 hours, or (d) 37 hours after removal. This is the predominant, and most widely accepted model thus far. Image taken from [4]



Figure 1-5: MOVEMENT OF THE INTESTINAL EPITHELIUM. Histoautoradiographs of small intestine at length 33% after 1 month of exposure (270). A, d1; B, d2; C, d5 after Pu ingestion. Image and Caption taken from: [5]





Figure 1-6: HISTOLOGY OF THE SMALL INTESTINE. Histological Image of the villi of the small intestine. Taken from Kansas University Medical Center (<http://www.kumc.edu/instruction/medicine/anatomy/histoweb/>)

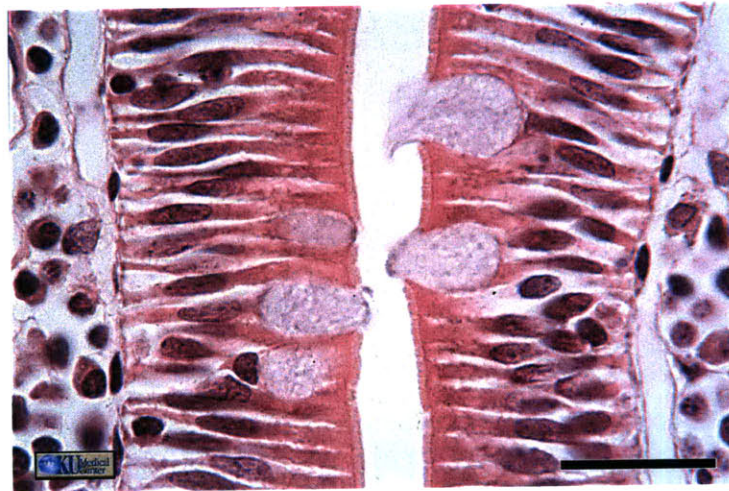


Figure 1-7: EPITHELIAL CELLS OF THE SMALL INTESTINE. Epithelial cells of the small intestine are columnar, and have no visible actin-based extensions, such as lamellipodia, filopodia, or pseudopodia. Taken from Kansas University Medical Center (<http://www.kumc.edu/instruction/medicine/anatomy/histoweb/>)

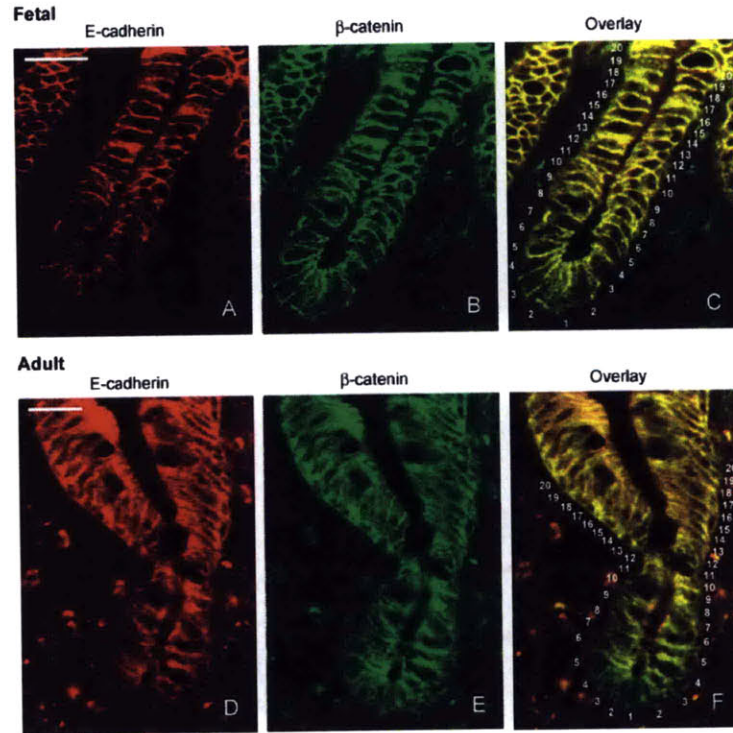


Figure 1-8: CADHERIN IN THE INTESTINE. Distribution of E-cadherin and  $\beta$ -catenin in fetal (AC) and adult (DF) human small intestine. Frozen sections of fetal intestine between 18 and 20 weeks of gestation were costained with a rabbit antibody to E-cadherin and a mouse anti- $\beta$ -catenin. The secondary antibodies, anti-rabbit conjugated to rhodamine, and anti-mouse conjugated to FITC, allowed the detection of E-cadherin (A and D) and  $\beta$ -catenin (B and E) independently. Overlays of both stainings (C and F) show the differential localization of the two proteins. Numbers in overlay pictures point to individual cell position in the crypts, position 1 indicating the bottom. Scale bars = 15  $\mu$ m. Image and Caption taken directly from [6]

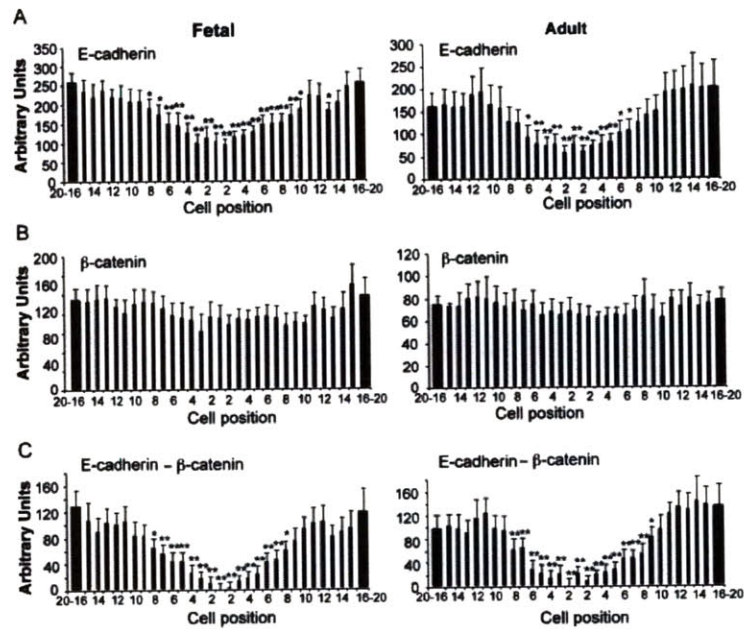


Figure 1-9: CADHERIN IN THE INTESTINE. Quantitation of E-cadherin (A),  $\beta$ -catenin (B), and the difference E-cadherin minus  $\beta$ -catenin (C) fluorescence stainings shown in Fig. 1. Quantifications were performed as described in Materials and methods on native images. Graphics present results obtained with four crypt/villus axes for 10 fetal and 7 adult tissues. Cell positions in the crypt are indicated by the number below the histograms. Bars 1620 represent means of cells at positions 1620 from each crypt side; these values were used as references for statistics ( $*p < 0.05$ ,  $**p < 0.02$ ). Image and Caption taken directly from [6]



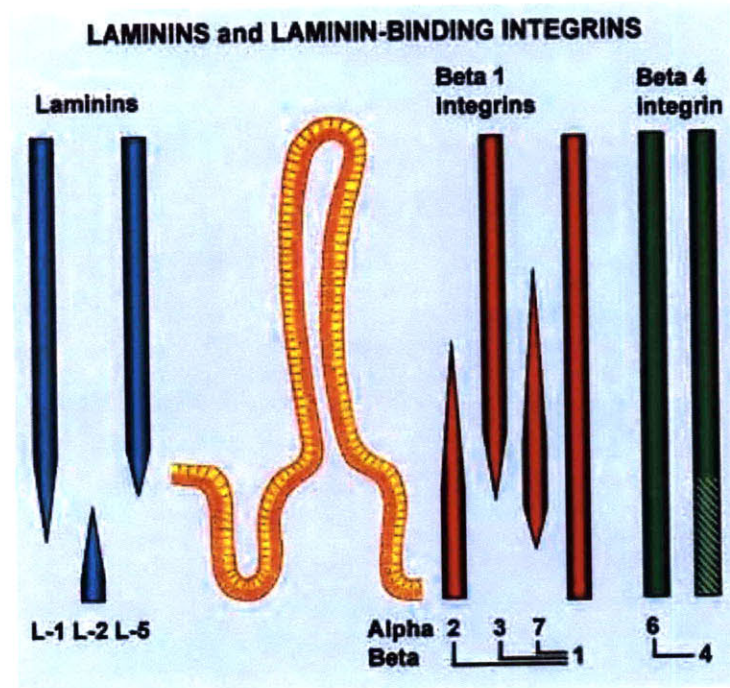


Figure 1-10: LAMININS AND INTEGRINS IN THE INTESTINE. Distribution of laminins and their corresponding integrins along the crypt-villus axis of the adult human small intestine. Laminin-1 ( $\alpha 1\beta 1\gamma 1$ ) and laminin-2 ( $\alpha 2\beta 1\gamma 1$ ) show complementary locations while laminin-5 ( $\alpha 3\beta 3\gamma 2$ ) is restricted to the villus. Among integrins,  $\alpha 6\beta 4$ , which can bind to these three laminins, is distributed uniformly, while the basal distribution of  $\alpha 3\beta 1$  in intestinal cells coincides with the location of its specific ligand, laminin-5. In contrast, the laminin-1 binding integrin  $\alpha 7\beta 1$  is primarily expressed in the differentiating compartment. Image and Caption taken directly from [7].

## Chapter 2

# Initial and Boundary Conditions in the Collective Migration of Epithelial Sheets

### 2.1 Introduction

Using a novel, microfluidic-based technique, we study how the coordinated migration of epithelial sheets respond to asymmetry; either in the creation of free space (i.e. a model wound), or by the generation of gradients in the capacity for cell movement, amongst a mutually adherent epithelial monolayer. First, this method allows us to present the only truly 'damage free' denudation, to determine the influence of free space on the onset of sheet migration. Further, we can recreate uniaxial gradients in chemical factors, that allows us to emulate the spatial localization of varied cellular functions that exist in the natural boundary conditions of the *in vivo* epithelia, such as the motile/mon-motile, or viable/apoptotic gradients that exist along the crypt-villus axis of the intestine. From this, we indeed conclude that enzymatic denudation (the first non-physical method) is sufficient to break symmetry and induce movement, but this movement is largely density dependent, limited to the leading edge, and more prone to scattering than its counterpart, the classical wound healing experiment. Fur-

ther, to address the default hypotheses that cells on rigid substrates are in a balanced state of pushing and pulling [29, 46], we imbalance this propensity, by the imposition of a gradient in cytoskeleton contractility, and show that no such mechanism exists, as defined by our microfluidic system. Finally, we control the level of cell-cell contact, to not only show that cadherin-dependent cell-cell adhesion is a hindrance to fast movement, but its ablation increases coordinated movement in a wound healing model.

*In vitro* analyses have largely focused on wounding as the denudation in culture by scratching, is known to induce sheet motion, in many ways analogous to what is observed in *in vivo* wounded and unwounded scenarios. This has sparked a number of studies that have aimed to separate the influence of the generation of free space, from the cell damage induced by the denudation [33, 4]. Regarding the mechanism behind this movement, it has been sometimes concluded, and often inferred, that this directed movement of cell sheets, either *in vitro* or *in vivo* results from a dichotomy of pushing and pulling [29]. One such argument is that leading edge cells, or cells closest to the free border, may pull on those behind. Similar arguments have been made in the past, for the much hypothesized movement of the intestinal epithelium. Thus, in this chapter, we seek to first, unequivocally decouple the influence of free space from cell damage in the onset of collective migration in a model wound, and using the same experimental system, introduce asymmetry across a confluent sheet, in the ability of cells to migrate, or even asymmetry in their viability, in a sense, mimicking the crypt-villus axis of the intestinal epithelium, a model for collective (and uniaxial) motion, with unique asymmetry, intricately tied to the movement of the monolayer. In this sense we both test this default push/pull dogma, and at the same time recreate a natural boundary to understand how a mutually adherent cell monolayer senses and responds to non-open boundaries.

The principal model for this and similar *in vivo systems* is the wound healing assay. When an epithelial monolayer grown in culture is scratched along the surface that damages the sheet, cells on either side of the scratch will grow and reproduce

to close the gap. The cells in the front of the denuded sheet, called the leading edge, produce large, clear actin-based extensions that actively search their environment, and are distended in the direction of the edge. The cells behind the leading edge, termed sub-marginal cells, are still confined, and have only been shown very recently to extend mild lamellopodium along their basal surface in between their neighbors, in the direction of the wound [34]. Likewise, cells at the front move more than those in the rear. From this description however, we do not know whether the driving impetus for movement is based on the creation of free space, or there is an induction in signaling from the damage of scratching that results in conveyance of a message to move. There have been many efforts that have attempted to separate the two, but all of which require a physical interaction with the epithelial sheet, some with an admittedly small, but still existent cell death at the border. Needless to say, scratched, or separated from potential adherence to PDMS obstacles, each of these aforementioned methods involved the application of force to the sheet [4, 33]. In this study, we utilize a microfluidic system that can take advantage of multiphase flow, and selectively remove cells enzymatically, in the same manner that cells are passaged. We can use the same setup to test the movement of cells when their neighbors are made immobile, or less viable due to apoptosis.

## 2.2 Materials and Methods

Mouse Mammary Epithelial Cells (CLS-1, ATCC) were maintained in Dulbecco's Modified Eagle's medium (invitrogen), supplemented with 10% fetal bovine serum at 37C and 5%  $CO_2$  in a humidified incubator.

Convergent, Y-shaped channels (similar to [47]) 500  $\mu\text{m}$  in width were created by standard soft lithography methods (Figure 2-1), and were plasma etched to size 0 glass coverslips (Figure 2-1). Fibronectin (1mg/ml and 0.2mg/ml) was added to the channels and incubated at 37C for upwards of 1 hour, and then washed out with

DMEM supplemented with FBS (10 %) and Penicillin/Streptomycin (1%). The epithelial cells were seeded at very high densities into the channels, and then washed a few hours after seeding. The media was replaced roughly in 12 hour intervals until the cells reached confluency. A Harvard Apparatus Syringe Pump was then used to retract 0.05 % trypsin (or 200uM Blebbistatin, 100uM Cytochalasin D, or 0.875 % Hydrogen Peroxide, in cell media) and media (trypsin in 1 of the 3 channels) at a rate of about 30ul/min from three, 1ml tips at each of the three inlets, serving as reservoirs. After cleavage of cells, additional media was added to the two tips initially containing media, to restrict the flow of trypsin, until the tip that originally contained trypsin could be replaced with another tip containing media. At this point, the flow was reduced to 0.5ul/min. 5%  $CO_2$  gas was fed into the central inlet tip, and the entire system was maintained at 37C in an enclosed chamber, for the entire experiment. When imaged, the cells were stained 1:1000 with CMFDA (MolecularProbes), 1:10000 DiI (MolecularProbes), and by brightfield, to ensure that the mode of motility is not determined, or limited by the contrast agent (in particular to verify scattering wasn't due to exposure). Further, to disrupt cell-cell junctions, we use antibody against E-cadherin (Invitrogen) [25]. Images were taken at 488nm or 568nm, every 5 minutes for up to 2.5 days on a Zeiss Axiovert 200M Confocal Microscope with a 25x oil immersion lens (Plan Neofluar 25x/0.80 1mm Korr DIC). Imaris (bitplane) imaging software and Matlab particle tracking software (<http://physics.georgetown.edu/matlab/>) were used to identify the centroids of the cells, by their peak intensity, and assemble time course trajectories.

The re-epithelialization in our denudation experiments proceeds nearly entirely through migration, and not cell division. Throughout the wound and model wound experiments, the epithelial sheets were grown to high confluence, generally greater than 2000 cells/ $mm^2$ . At this point, most of the cells are growth arrested, as a timecourse on the order of 12 hours will have less than 10 cell divisions, from an imaged population of approximately 300 (the low density sheets, which generally result in scattering, may have many more). Further, the cells used in these experiments,



mouse mammary epithelial cells, are only expected to divide once every 24 hours, up to 1000-2000  $cells/mm^2$  [48]. For our studies, we span the range of density, but coordinated movement is generally only observed above 2000  $cells/mm^2$ , and therefore most experiments are above this level.

## 2.3 Mathematical Analysis

The propensity to break symmetry, and move in a directed fashion is determined by finding the angle between successive vectors of individual cell movement, over an elapsed time,  $\tau$ , for equilibrium (no free space) measurements, to establish a baseline density dependence (Figures 2-18,2-19). Each vector is taken as the displacement that occurs in cartesian coordinates over every 25 minutes (to remove tracking errors that occur over short timescales).

$$\langle \cos \theta \rangle = \sum^N \cos \theta_\tau \quad (2.1)$$

For equilibrium measurements the ensemble average generally has the asymptotic form:

$$\langle \cos \theta \rangle \propto \tau^\alpha, \quad (2.2)$$

where  $\alpha \sim [-1.5, -0.6]$ , for the uncorrelated to the highly correlated cases.

Under non-equilibrium scenarios (denudation), the ensemble average depends on time, and is therefore calculated in real time.

$$\langle \cos \theta \rangle = \sum^N \cos \theta_{t,t+\tau}, \quad (2.3)$$

This metric is a sum over all trajectories,  $N$ , that exist for each point in time  $t$ , where the angle  $\theta$  is taken between the vector defined by  $t$  and  $t + \tau$ , generally set to be 25 min . The ensemble average will vary with  $t$ , generally marked by an initial increase towards 1, and an eventual decay to 0.

The velocity autocorrelation is the product of the initial speed and the speed measured at some time,  $t$ , averaged over all trajectories that exist for that time,  $t$ .

$$\langle \cos v(0)v(t) \rangle = \sum^N v(0)v(t) \quad (2.4)$$

We choose these two metrics, because while the magnitude of the velocity for each cell in the population depends strongly upon the distance from the leading edge, the angle of orientation between successive vectors in real space does not. Upon initial denudation, nearly all cells have already acquired a degree of directionality in the direction of the wound.

## 2.4 Free Space is Sufficient for Generating Collective Motion

Immediately upon denudation, either by scratching or trypsin, cells at the border break symmetry and penetrate into the newly created free space. What was an initially linear border (in both cases), extends outwards in time, and acquires a more complex profile. The manner in which this movement is induced, is dependent upon cell density (Figures 2-4,2-5). At low densities, cells catter, moving quickly and diffusively, and fill space primarily by cell division. Contrastingly, as the density is increased, there is a formation of a continuous border, defined by tight cadherin contacts (Figure 2-6,C.) that characterizes the movement into free space. At very high densities however, this motion is slow and less directed, with the formation of what has been described previously as a "fingering instability" [4](Figure 2-4)). The border is no longer straight, and there is the emergence of "leader cells" that penetrate into space faster than the others, but retain their cell contact. The generation of these projections, either broad or narrow, prevent the border from growing and advancing linearly.

Qualitatively, free space alone is enough to induce movement for both methods of denudation, although as a matter of degree, at high densities (e.g. most similar to *in vivo*), motion is slow, sometimes unstable, and limited to the leading edge for the enzymatic denudation, and not suitable for providing fast, uniform, and directed motion. The dynamics of the border are slowed, and the fingering instability, for example, often shows very little net movement overall, even over the course of days. The dynamics of the bulk of the population, the submarginal cells, is often marked by nearly no net movement, or significant directional persistence. This may account for the increased propensity for cells to scatter at intermediate to high densities, where that speed is recovered. Averaging in the runs that both scattered and moved uniformly at similar densities however, results in statistical equivalence in the velocity between the wound and model wound (Figure (2-3)).

#### **2.4.1 Dynamics of the border**

For both methods of denudation, the increase in area during re-epithelization proceeds logarithmically with time. Over short times however ( $\sim 12$ hrs), this movement is linear. The rate of epithelialization, the slope of this recovered area with time, shows a bimodal behavior (Figure 2-11). If the density of the sheet is very low, cells consistently recover the free space by scattering, where cell contacts are broken, and thus there is little to no increase in overall area. As the density is increased, the sheet becomes more likely to retain its contacts, while still moving quickly. However, as the density is further increased beyond this point, cell contact is clearly an obstacle to the recovery of free space. This general trend is evident in both the denudation by scratching, as well as the enzymatic denudation. However, at the intermediate density, the speed of recovery is much faster in the physical wound than in the model wound (given uniform motion amongst a cohered population, and not by scattering). Nevertheless, we presume these two mechanisms to be roughly equivalent, as differences in the magnitude of the velocities may also be a result of differences in culturing between cells grown on an open coverslip, immersed in media, and within a microfluidic device within continuous perfusion.

## 2.4.2 Dynamics of the bulk

It has been previously shown that the velocity of cells within the the bulk of a physically denuded sheet varies with penetration depth into the rear of the sheet. Shown in Figure 2-8, that there is a significant latency in the induction of movement amount the submarginal cells. The leading edge is highly correlated, which it retains for the length of the timecourse. For initial depths of 50 and 100  $\mu\text{m}$  into the rear of the sheet, correlated, high speed movement is not significantly lower than the leading edge, but waits until those in the front of the line move first. The enzymatically denuded sheet shows a similar latency as the physically wounded model. The magnitude of the correlation is much lower, and the length of this latency is much longer. The cells 100 $\mu\text{m}$  towards the rear take on the order of 2 hours longer to initiate movement.

While the magnitude of the velocity varies significantly with distance from the leading edge, the direction of movement generally does not, as all cells attempt to break symmetry and move (to whatever degree) in the direction of the wound. Sheets at different densities (regardless of denudation method) are differentially able to break symmetry, as monolayers below roughly 3000 *cells/mm<sup>2</sup>* have a rapid rise in  $\langle \cos\theta \rangle$ , and is retained until the density again approaches uniformity (Figure 2-9). Highly dense monolayers however, develop an initial directionality, which is eventually lost, in part due to the less persistent behavior in the rear population (again, evident in both models, but more pronounced in the model wound, Figure 2-10). There is nearly no net movement within the bulk, only at the periphery. The apparent density dependence in the resistance to fast, uniform motion however, is complicated by two variables, the crowding of neighbors, as well as the specific adhesive interactions between cells. We can separate these two effects, by blocking E-cadherin, the primary cell-cell junctional protein, highly expressed in epithelial tissues (Figure 2-10). Upon blocking of E-cadherin in a densely packed monolayer, there is a markedly increased speed, as well as uniformity and orientation (Figure 2-10,B). Generally, there is a separation of timescales associated with the onset of cell movement, as cells at the

border move quickly, and until they move from their initial positions, those in the rear cannot initiate movement. When cell-contact is blocked however, cells across the length of the sheet essentially move at the same time. Thus, it is cell contact, and not excluded volume, cell crowding that inhibits increased mobility in the non-equilibrium movement of the epithelial sheet. This is also consistent with other studies, where there is reduced motility of the epithelium of the intestine with the overexpression of E-cadherin [32].

## **2.5 Free Space is Necessary for Generating Collective Motion**

### **2.5.1 Closed Boundaries**

It has been argued that cells are in a dynamic state of compression and tension, and thus for a fully confluent cell monolayer, no net movement is observed. As we understand that the actin-myosin network of the cell is responsible for any given force, we choose to disrupt this network in a sharply graded fashion, along one axis of a fully cohered cell monolayer. Thus, there is now a boundary between cells that are able to contract their cytoskeleton, and those that cannot. At this interface, cell-cell contact is maintained, but there is now an imbalance in the capacity to generate force, in this sense similar to the open boundary in the denudation studies. If indeed there was balanced physical contention between cells in a normal monolayer, presumably cells at the boundary are now imbalanced.

The movement of non-treated, viable cells was assessed two ways, given a sharp gradient of  $200\mu\text{M}$  blebbistatin. First, the movement of cells was assessed while flowing the blebbistatin while simultaneously imaging cell movement in the non-treated population. Cells on one side of the sheet (treated side) are losing their contractility in real time, and we track the movement of cells on the other side. The second

method is introducing a pulse of the blebbistatin for a short period of time, waiting until their morphology has changed, and then removing the blebbistatin, lowering the flow, and watching the cells migrate (and this way having a low shear, see Appendix). In either scenario, the viable cells did not break symmetry, but moved as if there was no functional boundary between the viable, and the non-contractile cells (Figure 2-12). Thus, there was no apparent difference in their migratory pattern given this functional boundary. The same was observed for a viable/apoptotic boundary.

In the same fashion as the blebbistatin, the sharp gradient in hydrogen peroxide, induced apoptosis on one half of the sheet. The result in this scenario was that again, there was no induction of symmetry breaking. This is also interesting, given that in a few of the runs, after some period of time, the apoptotic cells get removed with the flow, such that there is now a free, and open boundary similar to the denudation studies, and still, cells did not penetrate into space. There were subdiffusive, and could not invade space. Therefore, it would appear that under no studies, where cellular function was altered along the one-dimensional gradient, without open space, was there any directed motion. Therefore, we conclude that collective migration, as we define by movement along a non-compliant substrate, requires free space.

## 2.6 Conclusions

The method of denudation in this study differs significantly from other efforts that focus on a direct physical interaction with the surface, either by the application and removal of a PDMS block or via stencils. The separation of fluids in a microfluidic chamber offers significant advancements over the aforementioned methods. For the first time, we can say with certainty that the creation of free space can be separated from potential cell damage (other methods are speculative, and rely on trypan blue as an estimate of cell death). This denudation occurs with the same level of definition, which can be altered by simply altering the flow. In addition, via this method, the process of denudation can be observed in real time. And finally, and most signifi-

cantly, this method is very versatile, and thus can be used to alter cellular behavior by the selective delivery of drugs and other small molecules.

We show unequivocally (with the first non-physical method) that free space is indeed sufficient to instigate coordinated, persistent motility. Enzymatic denudation yields the same general time and density-dependence as a scratched denudation. In both scenarios, at low densities, re-epithelialization requires breaking their cell-cell contact (clearly preferred mechanism), while at higher densities, space is recovered by the slow progression of a continuous border. The former mechanism appears to be a faster and more efficient, as at even higher densities, with blocked cell contact, cells adjust their direction and speeds more quickly and uniformly. In the absence of free space, but under imposed gradients of agents that alter motility, there is no gradient in motion. Thus, it would appear that free space may not only be sufficient, but necessary for coordinated, unidirectional movement.

## 2.7 Supplemental Information

### 2.7.1 Density Dependence for Equilibrium Movement

It is well known that increased density will reduce the motility of epithelial cells under equilibrium (no free space) conditions (Figure 2-19), although upon denudation, even non-equilibrium movement is constrained by density (Figure 2-4). When cells are less constrained by their neighbors, straighter paths will persist, and decay as a power law over an elapsed time,  $\tau$ . The exponent for this decay will vary from barely confluent monolayers to highly dense monolayers, from  $\tau^{-0.6}$  to  $\tau^{-1.5}$ . Qualitatively, the transition that occurs with density goes from paths that persist to completely ablated movement.

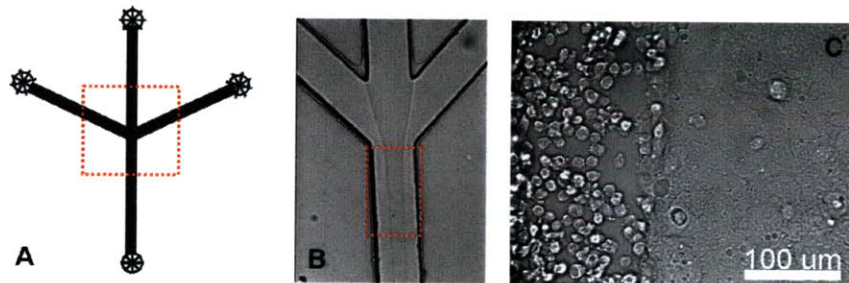


Figure 2-1: DIAGRAM OF MICROFLUIDIC SYSTEM. (A). Three inlets lead into a main channel, each  $500\ \mu\text{m}$  wide, and  $100\ \mu\text{m}$  high. When the volumetric flow rate that retracts fluid into the channel from the inlets is greater than  $10\ \mu\text{L}/\text{min}$ , the flow is laminar, and the fluid from the three inlets flow side by side, separated over short distances into the channel, (B). The trypsin channel can either be at the side, or in the middle. (C) All migration experiments utilize a flow of  $30\ \mu\text{L}/\text{min}$ . At this rate to enzymatically cleave cells with trypsin, carrying the away with the flow. After they have been removed, media is switched to the trypsin inlet, and the flow is reduced to  $0.5\ \mu\text{l}/\text{min}$ , and we image the movement of the viable cells.



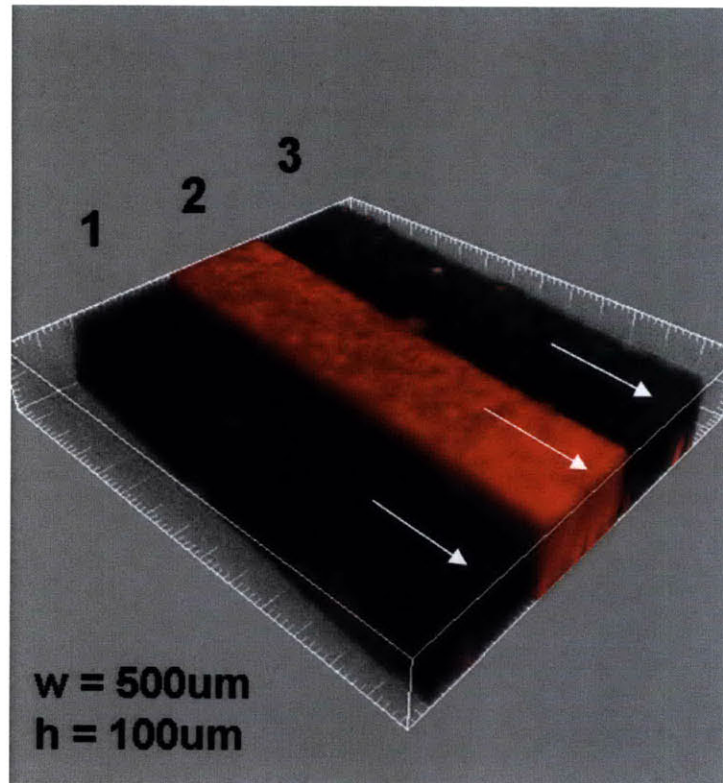


Figure 2-2: DIMENSIONS AND FLOW IN THE MICROFLUIDIC CHANNEL. 3D Confocal Image of the microfluidic channel, with three separate fluid streams (all cell media, at a volumetric flow rate of  $30\ \mu\text{L}/\text{min}$ ), with two separate fluorescent dyes, 568 Alexa Fluor (inner stream) and 647 Alexa Fluor (outer streams). The shear,  $\tau$ , across the cell monolayer varies with the inverse square of the channel height (approximately, as we cannot say  $w \gg h$ ), and the inverse of the width. The initial flow used to separate the laminar flows, yields an initial shear stress of  $4.4\text{dyn}/\text{cm}^2$ , which is held for 5-10 minutes. After the cells have been cleaved from the channel, the flow is reduced, and the shear drops to  $0.073\text{dyn}/\text{cm}^2$ . This flow is chosen to be arbitrarily small, such that the shear stress is negligible, but yet fresh media is constantly being delivered to the cells.

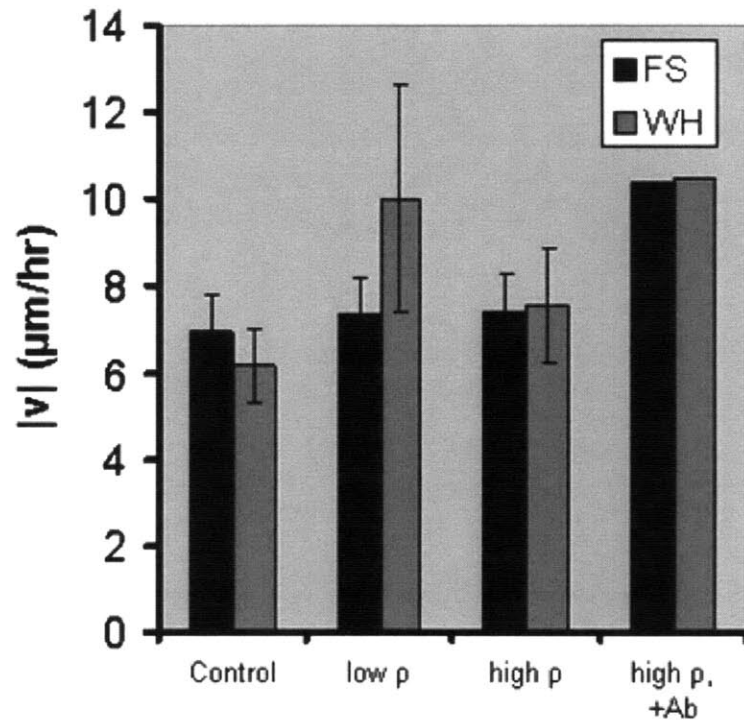


Figure 2-3: MEAN CELL VELOCITIES FOR WOUND AND MODEL WOUND. Cells are stained with 1:1000 CMFDA, and imaged over the course of 12-36 hours, on either a Mattek Dish (Wound Healing Assay, denoted WH), or inside the microfluidic channel (having isolated free space alone, with no cell damage, denoted as FS). The mean velocities for cell motion over this time are shown for experiments with no free space (control), or with denudation at low and high densities. Also at high density, 200  $\mu\text{g}$  of anti E-cadherin antibody was added. The mean velocities are significantly increased when cell contact is blocked.

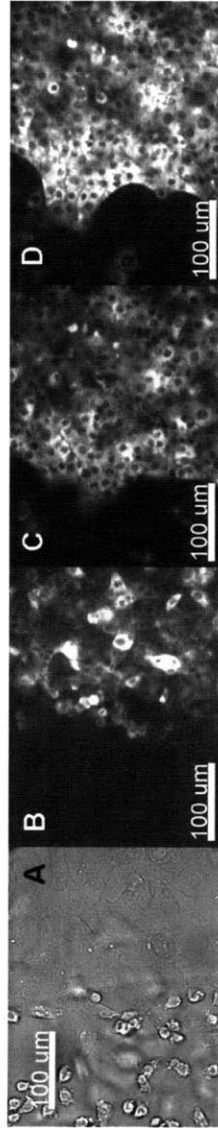


Figure 2-4: HIGH DENSITY MOVEMENT AFTER ENZYMATIC DENUDATION. (A). Brightfield image of 0.05% Trypsin cleaving cells from the left hand side of a  $500\ \mu\text{m}$  wide channel. At high densities, fingering instabilities often occur, and result in little net movement after (B) 0, (C) 1 day, (D) 1.5 days, all stained with DiI, a calcium stain. The instability itself is highly motile in the direction perpendicular to, but not parallel to the axis of initial penetration.

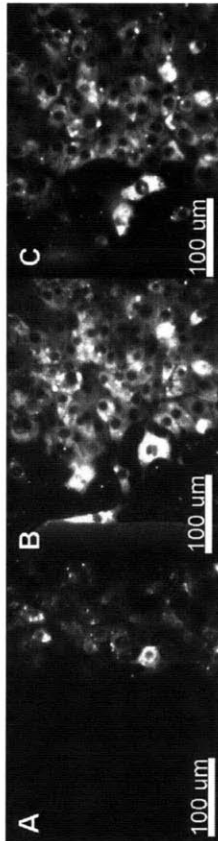


Figure 2-5: LOW DENSITY MOVEMENT AFTER ENZYMATIC DENUDATION. At low density, there is much faster net movement, and the reoccupation of free space, although principally, cells will tend to scatter, rather than more uniformly, or form secondary structures, like the fingering instability. Images are taken after (A) 0, (B) 1 day (C) 1.5 days.

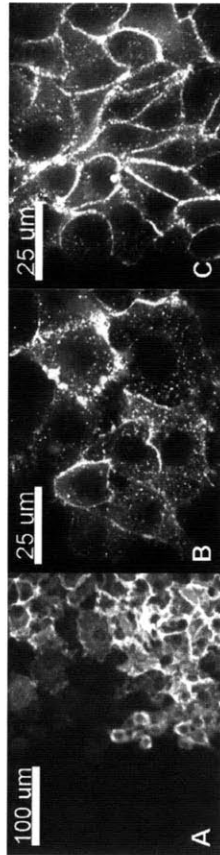


Figure 2-6: E-CADHERIN AT DIFFERENT DENSITIES. E-cadherin staining from enzymatically denuded microfluidic experiments, taken at different densities. (A) 25x image of a cleaved ( $T=0$ ) sheet inside of a channel, with an intermediate density. Within this fully confluent sheet, there are regies of both high density and low density, as can be seen by the heterogeneous expression of E-cadherin. Similarly shown at 100x, at both low (B) or high (C) densities.

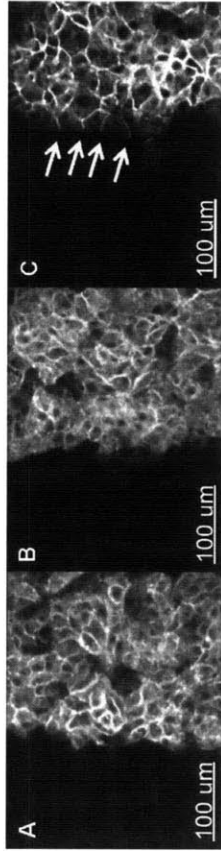


Figure 2-7: CADHERIN TIME COURSE. E-cadherin staining on samples taken (A) 0 hrs, (B) 6 hrs, or (C) 12 hours after being denuded by phase separated flow. Fingering instabilities arise slowly, due to the clear persistence of cadherin at high densities at the leading edge (arrows in (C)).

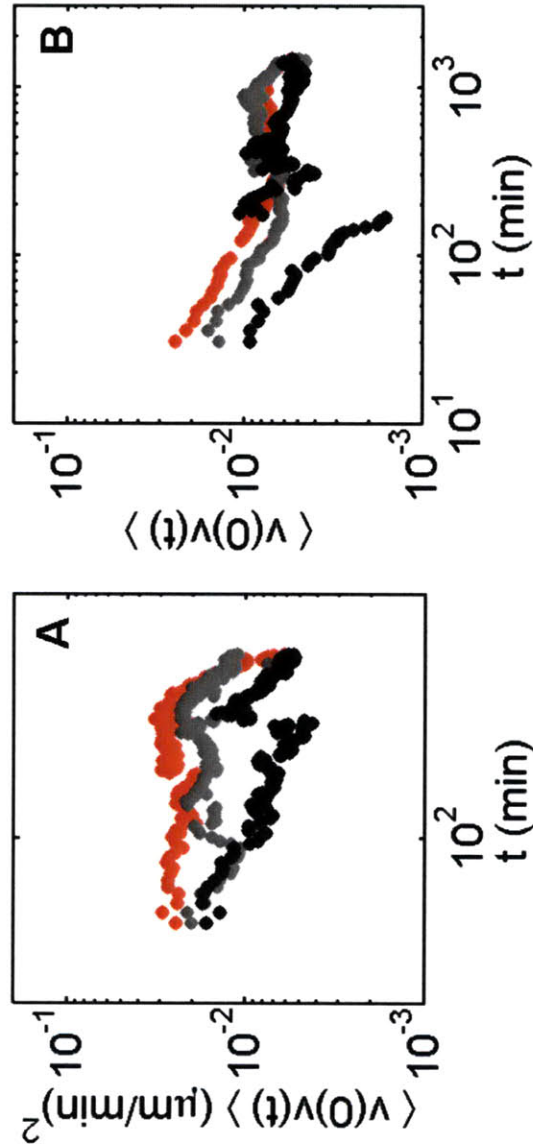


Figure 2-8: LATENCY IN MIGRATION FOLLOWING PHYSICAL WOUND. Ensemble averaged real time velocity correlation function for wound (WH) (A) and model wound (FS) (B) experiments. The red plot is the leading edge cells, followed by cells  $50 \mu\text{m}$  (gray) and  $100\mu\text{m}$  (black) behind the leading edge. Both models show a separation of timescales for the onset of correlated behavior, although there is a significantly greater latency for the the submarginal cells in the model wound system than the wound healing assay. This is indicated by the sudden jump in correlation for the gray and black curves, after some time delay.

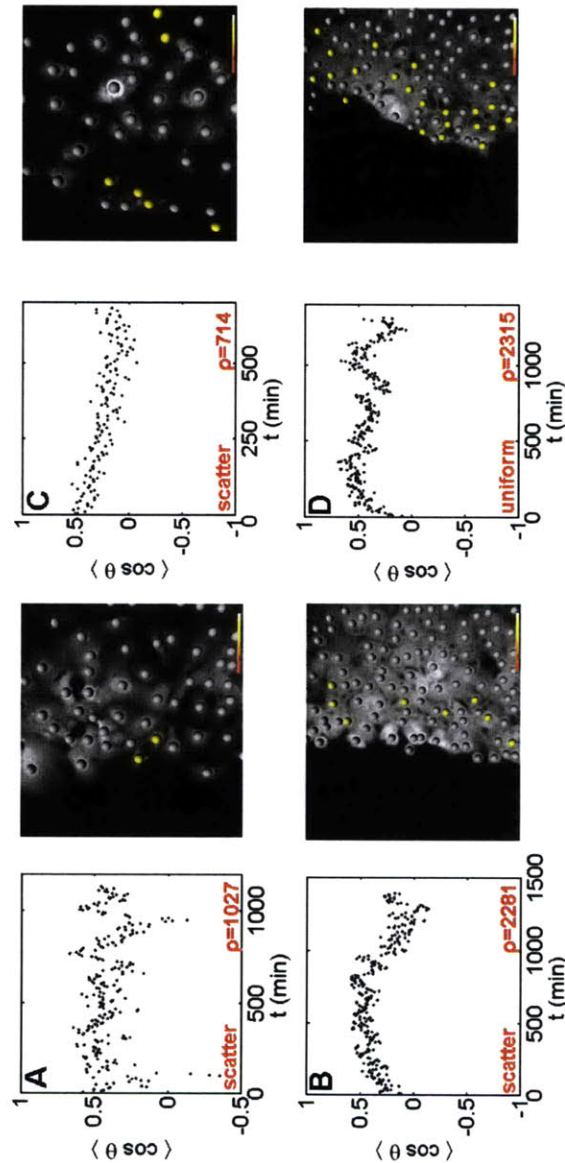


Figure 2-9: MEAN COSINE FOR LOW DENSITY SHEETS. Movement for sub-confluent sheets (A,C) is generally random, either progressing directly to zero post denudation, or constantly oscillating back and forth. The yellow dots are cells at the beginning of the time course that will eventually persist for  $\langle \cos \theta \rangle > 0.3$ . At low density, they are dispersed throughout the sheet, while at intermediate to high densities, they are relegated to the periphery. For sheets of increased density (B,D), there is a mean direction, with most cells moving out into free space.



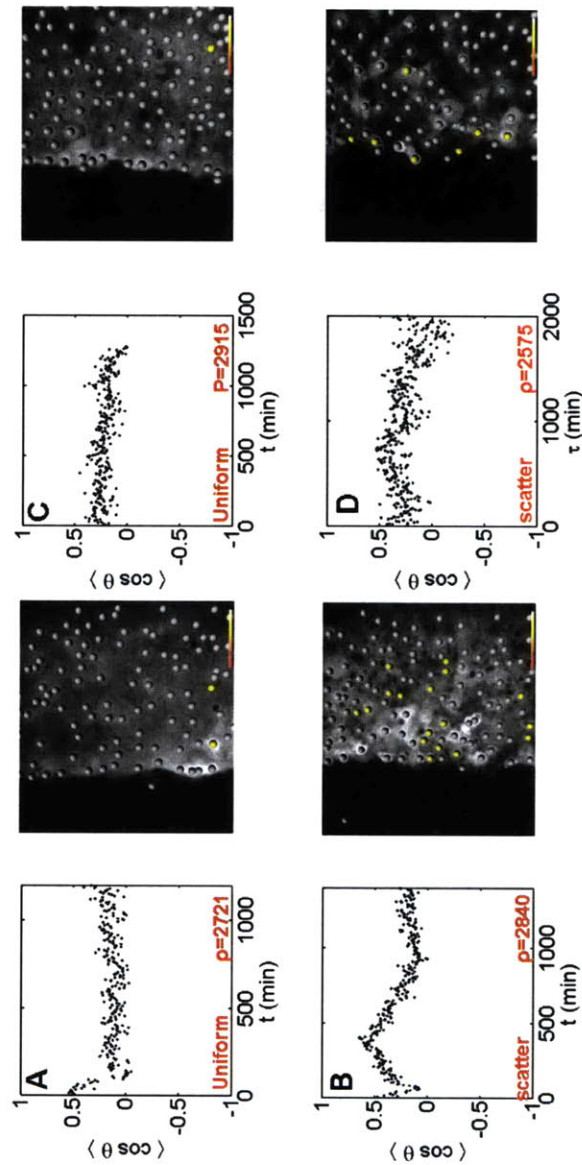


Figure 2-10: MEAN COSINE FOR HIGH DENSITY SHEETS. As the density of the cell monolayers reaches a maximum (A,C), nearly all directed movement is ablated. Cell movement is relegated purely to the periphery, with virtually no net directed movement in the bulk. When epithelial E-cadherin is blocked with monoclonal antibody (B,D), this effect is reversed, and even at high density, highly coordinated, directed movement is observed. In fact, the transition to coordinated movement is highly linear in time, as is its subsequent randomization when the density evens out (when both sides of the denudation meet each other).

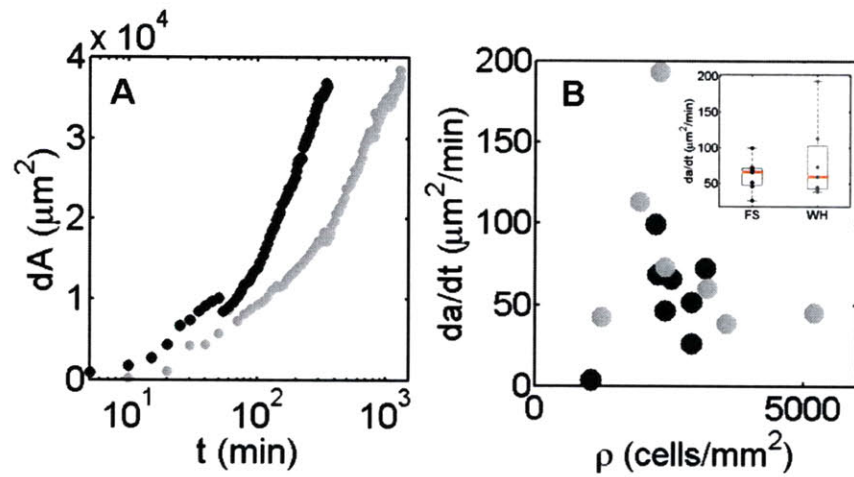


Figure 2-11: DYNAMICS OF THE BORDER. The rate of re-epithelialization of the free space depends highly on density, being slow at both very low density, where cells scatter, and very high densities, which are retarded by cell contact. This is evident in the slopes of the recovery of this area (A). This can be seen in the slope plotted for wounds (WH) and "model" wounds (FS) at different densities (B). Both methods of denudation, the wound (gray), and the model wound (black) show this same dependence, although the speed of recovery is faster in the wound.

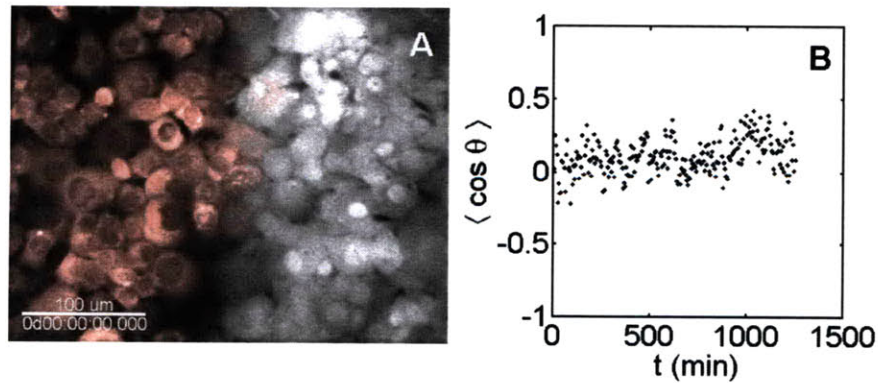


Figure 2-12: GRADIENT IN CONTRACTILITY. 200 $\mu$ M blebbistatin was used to make the left side of the monolayer non-contractile, by decreasing the affinity of Myosin II for filamentous actin (A). The right side is untreated. The results show that there is no directed movement by the untreated cells in preference for the non-contractile side (B).

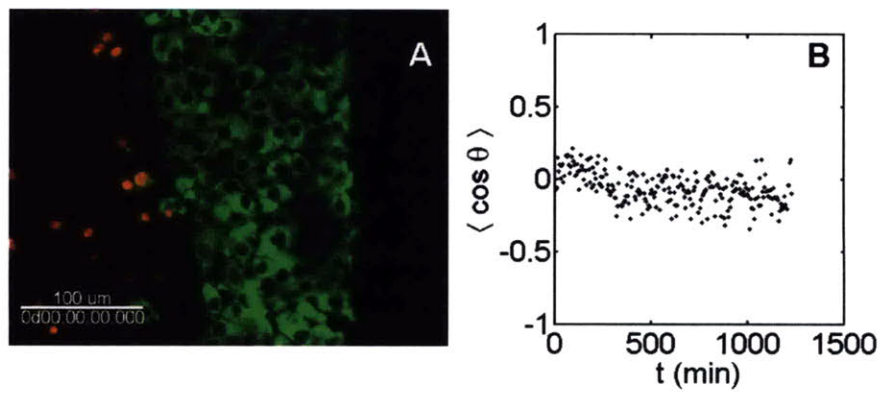


Figure 2-13: GRADIENT IN APOPTOSIS.  $0.0875\%H_2O_2$  was delivered to the left side, to induce apoptosis (A). This was imaged by a live/dead stain over 12 hours. (The tracked data in (B) however, was over roughly 24 hours, at half that concentration (0.042%).).

## 2.8 Appendix

### 2.8.1 Shear Stress in the Microfluidic Channel

The shear stress felt by the epithelial monolayer across the bottom of the microfluidic channel can be approximated by the Poiseuille model through parallel plates, where we assume that the length of the channel is much greater than the cross section of the channel (100  $\mu\text{m}$  tall, 500  $\mu\text{m}$  wide, 1 cm long).

$$\tau = -\frac{12Q\mu}{h^2w} \quad (2.5)$$

where  $Q$  is the volumetric flow rate,  $h$  is the height of the channel, and  $w$  is the width of the channel. The parameter  $\mu$  is the fluid viscosity. For the enzymatic denudation experiments,

1.  $Q_0 = 5 \times 10^{-4}$  mL/min
2.  $Q_f = 8.33 \times 10^{-6}$  mL/min
3.  $h = 0.01$  cm
4.  $w = 0.05$  cm
5.  $\mu = 7.339 \times 10^{-3}$  Poise

$Q_0$  is used to cleave the cells, and  $Q_f$  is used for the experimental run, where we track the movement of cells (no cell tracking during cleavage). Assuming the viscosity of the media and the trypsin are both the same, and equal to literature values above [49], we calculate a shear stress of  $\tau = 0.44$  Pa, or  $4.4 \text{ dyn/cm}^2$  for  $Q_0$ . When the flow was reduced, the shear stress dropped to  $0.0734 \text{ dyn/cm}^2$  for  $Q_f$ . While there isn't an overabundance of literature for flow with epithelial cells as there is with endothelial cells, some studies report that genes such as Erg-1, responsible for the activation of early response genes, such as mitogenesis and differentiation, are upregulated in HeLa cells, with as low as  $5 \text{ dyn/cm}^2$  shear, for 3 hours [50]. In lung alveolar epithelial cells, above  $30 \text{ dyn/cm}^2$ , it has been shown that a shear of  $30 \text{ dyn/cm}^2$  for upwards

of 4 hours increases the soluble fraction of intermediate filaments, implying that flow disassembles them [51]. Thus, we are well below this value for most of the entire timecourse experiments.

Yoon et al. [49], used a similar equation, but different by a factor of two:

$$\tau = -\frac{6Q\mu}{h^2w} \quad (2.6)$$

where they investigated the effect of shear on the deflection of intermediate filaments in Ptk2 kidney epithelial cells. For their calculated shear stress of  $\tau = 15 \text{ dyn/cm}^2$ , for the first two minutes, they showed an arrangement of intermediate filaments in the direction of flow, which subsided by 6 minutes. There was slight bending notices as late as 30 minutes after the onset (but still during) the flow. Thus, there is clearly very little problem with this level of shear on epithelial cells.

## 2.8.2 Alternate Gradients in Motility

There were a number of attempts to determine whether or not free space was necessary, and not just sufficient to initiating coordinated migration. If not pushing or pulling on the boundary, we were interested in observing just precisely how viable cells responded to non-functional neighbors, considering that they are all bound. Among these methods, include:

1. Fixing one half of the sheet with paraformaldehyde (Figure 2-14).
2. Inducing apoptosis in half the sheet, with a low concentration of hydrogen peroxide (Figure 2-15)
3. Making one half of the sheet non-motile with Cytochalasin D (Figure 2-16).

The paraformaldehyde was not pursued, as it induced apoptosis in surrounding cells, presumably due to its ability to diffuse through gap junctions. Both the induced apoptosis and impaired mobility via Cytochalasin proved valuable in understanding the contributing factors towards the onset of coordinated motion. As mentioned in this chapter, apoptosis ablates directed, invasive movement. And clearly, cytochalasin ablates movement altogether.

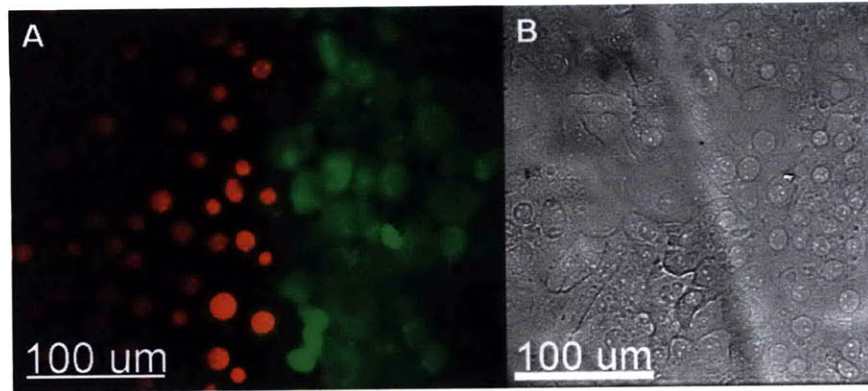


Figure 2-14: (A) Live Dead Stain with the middle channel filled with paraformaldehyde, and ran for just 2 minutes. The right side remains alive, but only for a short period of time. Fixing one side of the cells, even with no diffusion to the right, still killed the cells on the right hand side. There is likely a cell-cell communication signal that makes cell death proceed quickly across the entire length of the sheet. Thus, there was no chance to observe any migration in the viable population. (B) Brightfield image of both fixed and unfixed cells.

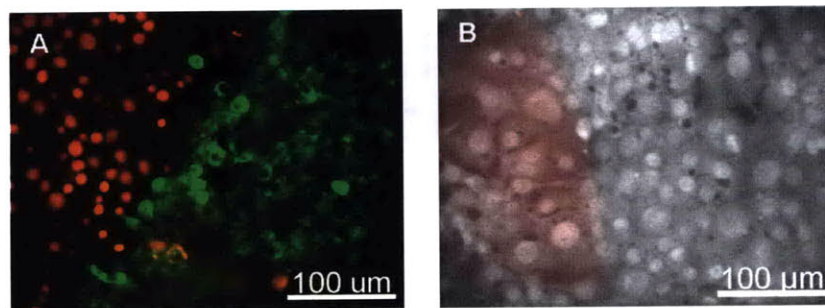


Figure 2-15: FUNCTIONAL BOUNDARIES. (A) Viable cells interface with apoptotic cells (red: apoptotic, green: viable), and (B) Motile cells interface with Non-Motile cells (Gray: Motile, Red: Non-motile). In neither case to the fully functional, viable cells push. No extension of border.

### **2.8.3 Viability in the Microfluidic Chamber**

There is no evident cell damage from the trypsinization of the cells inside of the microfluidic channel, as evident from a live/dead assay.



## 2.9 Protocols

### 2.9.1 Soft Lithography of 100 $\mu\text{m}$ high channels

I perform all of my lithography in the laboratory of David Weitz, in the department of Physics, at Harvard University (special thanks to Katie Humphry, a PhD student in Physics at Harvard, for both giving me access, and showing me how to do the lithography). Many of the settings will depend on your own equipment, in particular the UV source, and the plasma machine. Nevertheless, below is a basic outline of the procedures that I use for creating microfluidic chips.

#### Reagents

1. Transparency Mask
2. 2100 SU-8 Photoresist
3. 5" Silicon Wafers
4. PGMEA solvent
5. Isopropanol
6. Hotplates (65C, 95C), UV lamp, oven, Spincoat

#### Procedure

1. Pour about 3mL of SU8-2100 onto the 5" silicon wafer, place on the Spincoat. Make sure that when you are pouring, it doesn't fold back upon itself. This composition resist is very thick, and will trap bubbles, which will be hard to get out.
2. Spin at 2000 rpm, to get about 100  $\mu\text{m}$  thickness.
3. Remove the wafer from the spincoat by holding the edges, and place the wafer on a 65C hotplate for 5 minutes. Then switch over to the 95C hotplate, and leave it there for a minimum of 20 minutes. Afterwards, remove and place on aluminum foil to cool.

4. Place the wafer underneath the UV lamp, and place the transparency mask overtop. Make sure that it is conformal contact. If you have some transparent (quartz) parallel plates to hold them together, that would be better. Any gaps may show up as deformations on the photoresist.
5. For 100  $\mu\text{m}$  thick wafer, you will need an exposure energy of 240  $\text{mJ}/\text{cm}^2$ . Generally, a lamp will yield some fraction of this per second when placed a certain distance away from the source. The time of the exposure will depend on this distance, and clearly the energy of the lamp.
6. At the end of the exposure, you need to bake again. Again, for this specific thickness, about 5 minutes at 95C, and 10 minutes at 95C should be sufficient. While the wafer is baking, you should be able to see the mask designs starting to emerge. Allow to cool.
7. Once the wafer is cool, you can start developing. Submerge the wafer in a volume of PGMEA (in a glass dish), and gently swirl until you see all of the undeveloped photoresist come off. This should happen after about 10 to 15 minutes. At the end, you should wash it with isopropanol. If the wafer still has undeveloped photoresist on it, it will leave a white residue, and so you can just return it to the PGMEA. After washing with the isopropanol, you can air dry with filtered air, and the chip is done.
8. Place the mask inside of a plastic petri dish, and immerse it in 1:10 crosslinker/prepolymer PDMS.
9. Place the PDMS/master inside an oven, and bake at 65C for upwards of an hour.
10. When done baking, cut a square around the design, and pull out this piece of PDMS. Turn over, and cut out your design, so that it fits onto a coverslip. Now you have the chip.

11. Put transparent tape around coverglass to serve as a surface for the plasma machine. Then turn over the chip, so that it faces up, and place it, along with a coverslip on the surface and into the plasma machine. I exposure the chip and coverslip for about 45 seconds, and then sandwich them together. This forms a strong, permanent bond. Now the chip is fully bonded and ready for the experiment.
  
12. ALTERNATIVELY, send your .dwg mask drawing file to the Stanford Foundry, and order the master and chips! See: <http://thebigone.stanford.edu/foundry/>. It costs about the same as the mask that you had to order anyways, just to do the lithography yourself!

## 2.9.2 Immunostaining Adhesions inside the microfluidic channel

### Reagents

1. Paraformaldehyde
2. Triton-X
3. 10X PBS
4. Fetal Bovine Serum
5. Goat Serum
6. human, anti-mouse primary antibody (anti-E cadherin, or anti-Fak)
7. goat, anti-mouse secondary antibody

### Procedure

For fixation, we use 3.7% paraformaldehyde, as we have to use pipette tips as reservoirs, and so a methanol/acetone fixation would degrade the tip, and adulterate the sample. Prepare a stock, to be used within a month. Also, much of the incubation done is with pipette tips as reservoirs, and/or involve placing the chip in the incubator when it should be at a higher temperature, as the chip holds a small volume, and can dry out through the PDMS.

1. For making 100mL, 10mL 37% paraformaldehyde, with 1mL Triton-X (25%), 10mL 10x PBS, and 79.4mL of distilled water.
2. Take up 200  $\mu$ L into a tip, and plug that into the single inlet of the microfluidic chip. Insert three 200  $\mu$ L tips into the outlets to serve as reservoirs. Let this sit for 1 hour at 37C. You can place this into the incubator.
3. Rinse 1x with 1x PBS in the same fashion, at room temperature.
4. Block with 15% Replace the PBS with blocking buffer, 15%Fetal Bovine Serum in 1x PBS. Let this sit for 1 hour, at room temperature.

5. Introduce the primary, anti-E cadherin (or other) antibody, at a concentration of about  $10\mu\text{g}/\text{mL}$  in the same blocking buffer. The antibody should be raised in an animal model different from that of the blocking buffer (blocking buffer is bovine, antibody is human, anti-mouse). Let this sit at room temperature for 2 hours. Again, this can be introduced in a volume of about  $200\mu\text{L}$  by pipette tip.
6. Wash the chip 3x, in the same manner as the first wash. Let sit for 5 minutes each time, as the fluid from the tip flows through the tip, and equilibrates into the outlet reservoirs.
7. Introduce the secondary antibody (goat, anti-mouse) in the secondary blocking buffer, 15% goat serum in 1x PBS. The secondary antibody concentration in the secondary buffer should be the same as the first.
8. Wash the chip 3x again.
9. Leave in 1x PBS, or add mounting media if you wish.

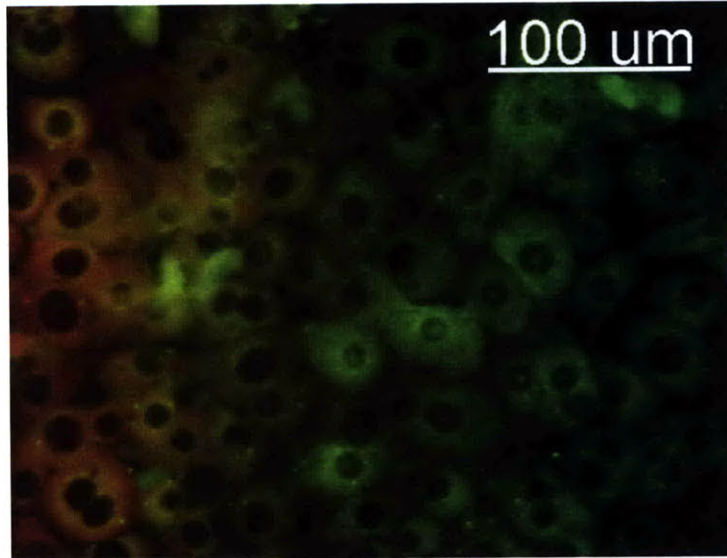


Figure 2-16: CYTOCHALASIN D. The left channel was filled with  $5\mu\text{M}$  cytochalasin D, creating a gradient across the lateral axis. The cytochalasin has a dye that emits at 468nm, and the right hand side was filled with normal medium, with 1:10000 DiI. Thus the red side has an altered cytoskeleton, with its actin unable to polymerize. The right hand side is normal. There was also no gradient in migration observed here.

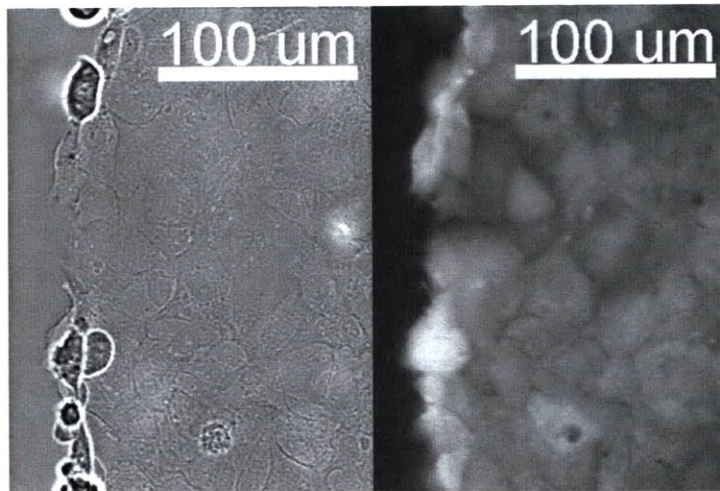


Figure 2-17: LIVE/DEAD IN MICROFLUIDICS. After the trypsin cut, all of the cells are alive. (A) brightfield, (B) calcium dye

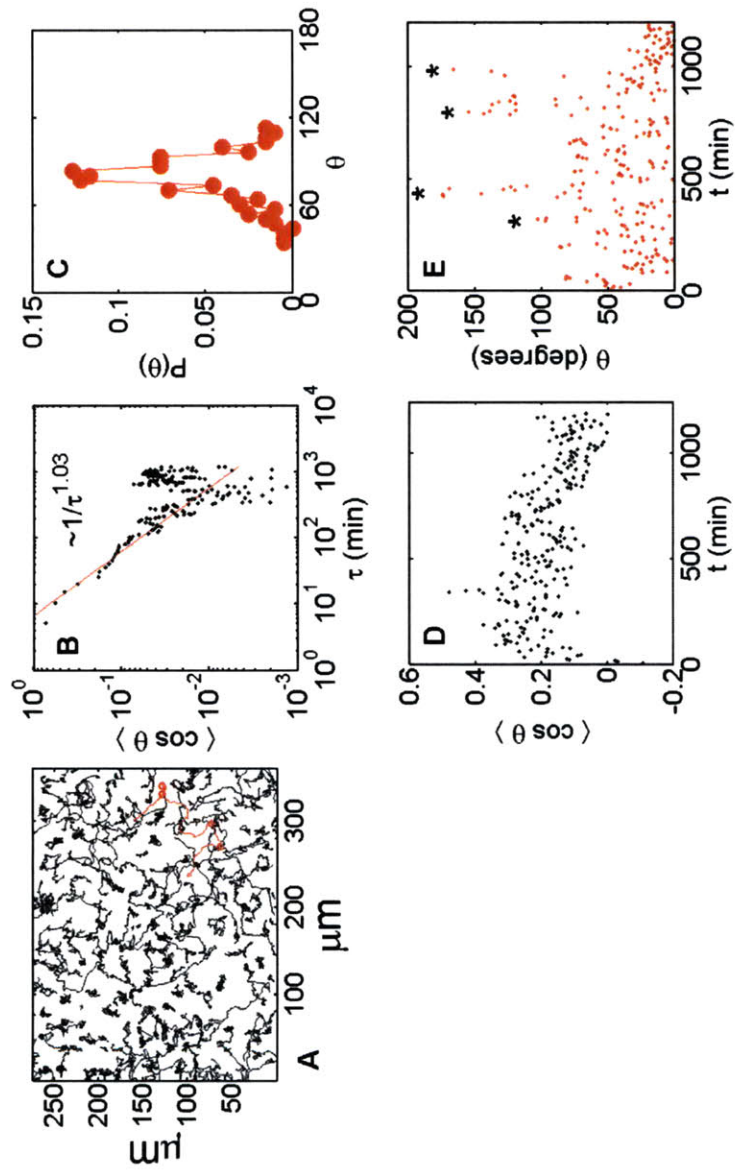


Figure 2-18: MEAN COSINE. Calculation of the mean cosine. For equilibrium (no free space) movement (A), the cosine of the angle between vectors separated by an elapsed time,  $\tau$  are averaged for the ensemble of trajectories over all  $t$  (B). That allows us to characterize the PDF for the angle of movement (C). If movement is non-equilibrium, as in wound healing and microfluidic denudation studies, it is calculated in real time, as the cosine of the angle between successive vectors (D,E).

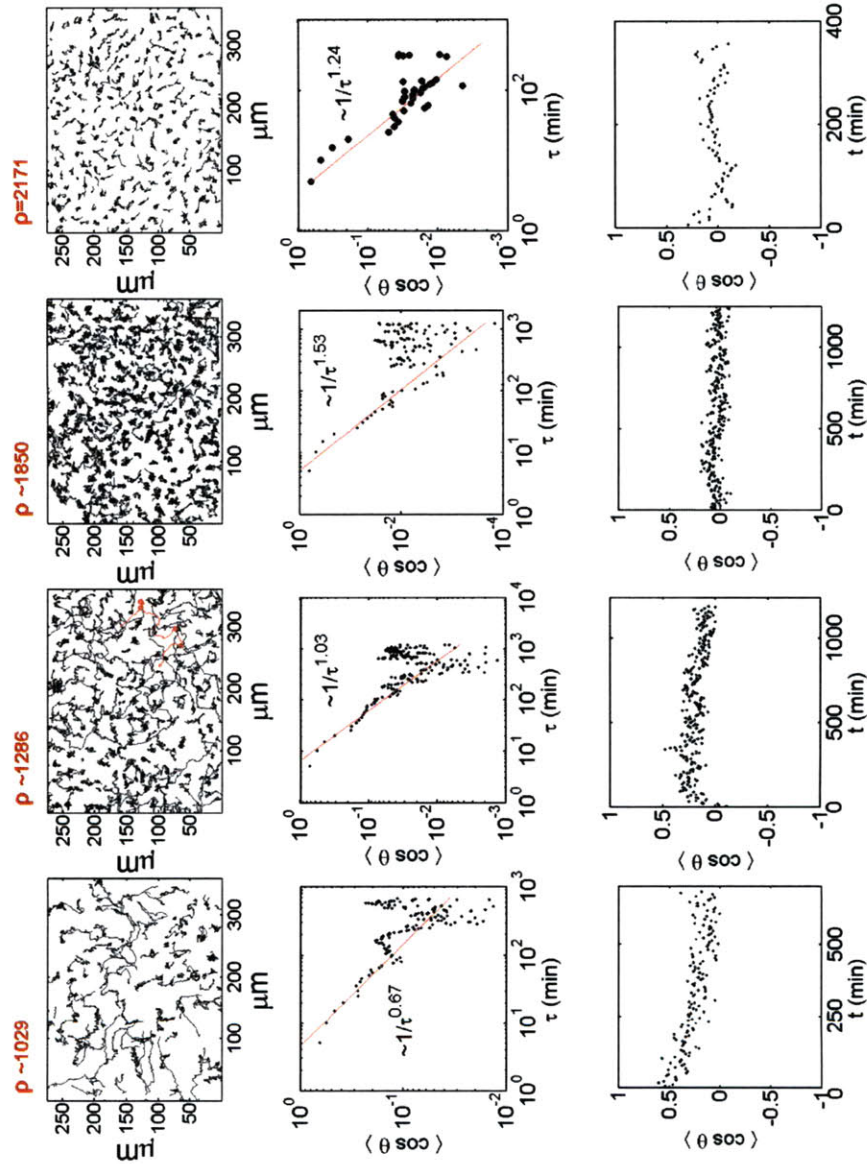


Figure 2-19: DENSITY DEPENDENCE. The density dependence of the mean cosine calculation for equilibrium movement. As the density is increased, the correlation lengthscale of the angle between successive vectors during the migration of cells within a sheet, decreases. With the smaller the magnitude of the scaling exponent, the longer the paths will persist as straight.



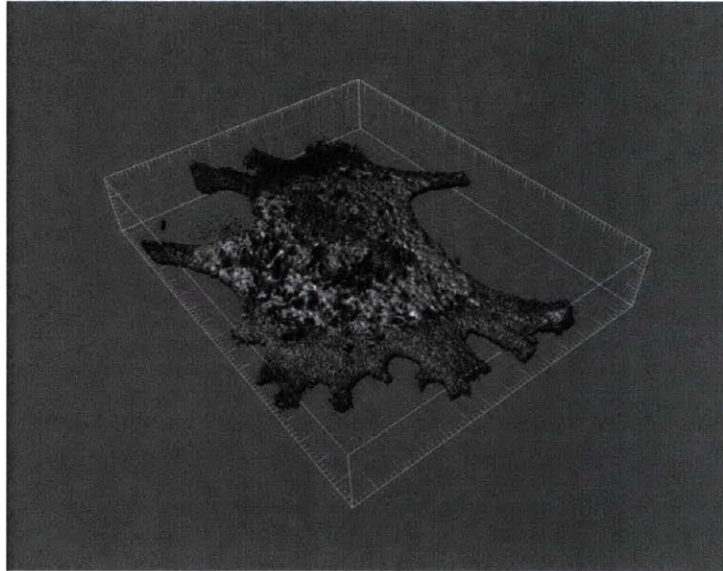


Figure 2-20: LEADING EDGE CELL MORPHOLOGY. Morphology of a leading edge CMFDA-stained cell in front of a fully confluent sheet, imaged at 100x. Grid =  $2\mu\text{m}$ .

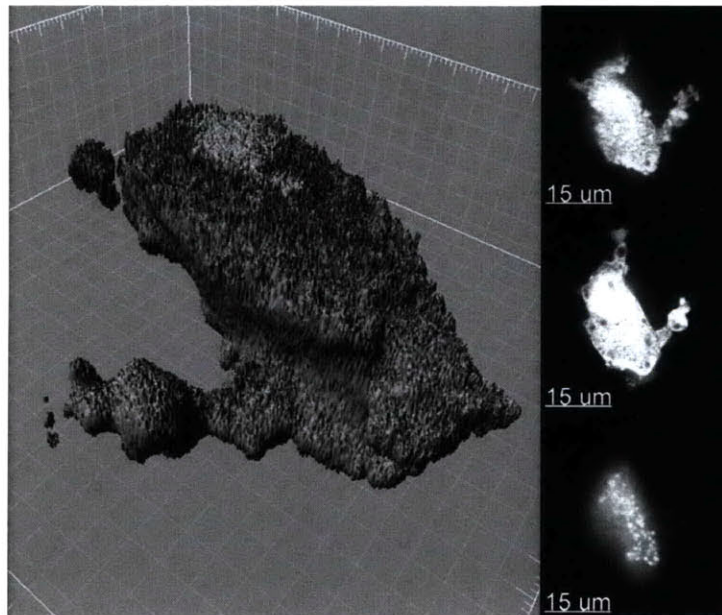


Figure 2-21: SUBMARGINAL CELL MORPHOLOGY. Morphology of a submarginal GFP-cell in a fully confluent sheet, imaged at 100x. Grid =  $2\mu\text{m}$ . Z slices are at 0.8 $\mu\text{m}$ , 2.8 $\mu\text{m}$ , and 10.8  $\mu\text{m}$  from the surface.

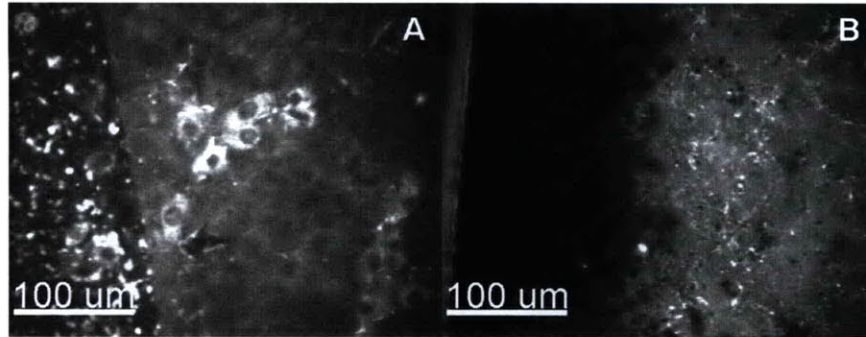


Figure 2-22: SURFACE PROTEIN REMOVAL. The denudation of cells, whether by physical scratching (A) with a 1ml pipette tip, or by enzymatic cleavage (B), removes surface protein (FN+FITC Collagen). In both cases, the new protein is added by the medium (that contains 10% FBS).

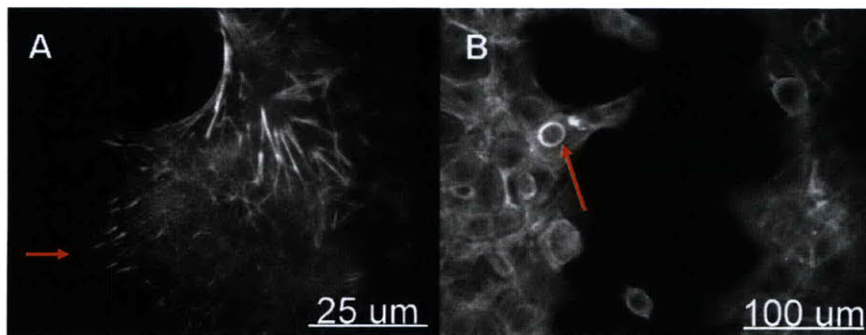


Figure 2-23: RETENTION OF ADHERENS JUNCTIONS DURING SHEET MOTION. During Wound Healing, as the sheet moves forward, the leading edge displays both focal adhesions (A, characteristic to single cell movement), as well as maintaining adherens junctions (B, characteristic to sheets). This is a fixed sample, stained with rhodamine-phalloidin.

# Chapter 3

## Substrate Mechanics and Cell Contact in Epithelial Cell Motion

### 3.1 Introduction

The study of adherent cellular monolayers as a model soft and active system can lend insight into the physical origin of correlated behavior that is implicated in important physiological processes, such as the movement of cells along mucosal surfaces (i.e. unidirectional motion in the turnover of the intestine, [28, 29, 30]), and the development of embryonic tissue (i.e. invagination of the endoderm and ectoderm, [52]). In these scenarios, we have little understanding of the *in vivo* time-dependent rheological properties of the substratum, and the influence on the emergent patterns of migrating cells within the sheet. More specifically, the rheology of the substratum will influence the extent to which the cells can deform it. This relationship however, is not straightforward, as the cell also has the potential to interact physically with its neighbors. Thus, the ability for a cell to deform its substratum may be altered when a member of a cohered population, and in turn, an actively deformed substrate may alter the overall migration of the population itself. Thus, to explore this bidirectional relationship [38], we relate the viscoelasticity of the substratum to the spatial and temporal correlations in velocity and density, and further explore the role of cell-contact in these correlations.

## 3.2 Materials and Methods

The closest approximations we have to the mechanical properties of the *in vivo* substratum, the basal lamina, that interfaces with epithelial sheets, are the excretions of extracellular matrix by tumor lines (Matrigel, BD Biosciences, [13]). This analog is of a gel-like consistency, with highly viscoelastic properties. When deformed at low frequencies, the material behaves largely as a viscous fluid, with the loss modulus approaching the storage modulus (Fig 3-1). Thus, we want to replicate this characteristic rheology, but also be able to alter it, so that we might explore the migratory patterns of cells within a monolayer for a wide range of moduli.

Thus, in this study, as a cell substratum, we use polydimethyl-siloxane spun onto a 20mm, size 0 Mattek dish, (PDMS, Sylgard 184 silicone elastomer base and curing agent; Mattek dish, Mattek Corp.), and alter the curing content over nearly an order of magnitude, to alter the shear modulus of the material over nearly five orders of magnitude (Fig 3-11). At high crosslinking concentrations (1/10), which is commonly used for the creation of PDMS devices (i.e. microfluidics, etc), the material is nearly purely elastic, and considerably stiff ( $\sim 35kPa$ ). As the ratio of crosslinker to prepolymer decreases, the shear modulus decreases, but the material also acquires a more viscous characteristic, offering an advantage in similarity to biological tissue, over purely elastic substrata, such as polyacrylamide. When the ratio approaches 1/80, like the Matrigel, for low frequencies ( $\omega = 10^{-1}rad/s$ ), the magnitude of the storage and loss moduli are roughly equal (this shear modulus will be denoted from now on as  $|G^*|$ , and equal 110Pa, measured at 1 rad/s). The surface of the material is coated with an adhesive protein, either fibronectin or collagen. These proteins can be adsorbed non-specifically (and thus dependent upon a potentially non-constant wettability), or attached covalently (denoted COV, reacted to aldehydes deposited via standard silane chemistry). Cells have adhesion receptors for these molecules, and

thus facilitate attachment of cells, as PDMS is not naturally very adhesive to cells [18].

To determine the time-dependent mechanical properties of the substrate, a constant, one-percent strain was applied to the PDMS under a cone (2 degree) and plate rheometer (Advanced Rheometer 2000), performing a frequency sweep between 1 and 100 radians/s (Fig 3-11). To ensure that this strain was within the linear regime, prior to each measurement, a strain sweep was performed roughly between 0.1 and 10 percent. The characteristic moduli for each material was taken at an angular frequency of 1 radian/s. Prior to mixing the crosslinker and the PDMS prepolymer, 0.1  $\mu\text{m}$  rhodamine carboxylated spheres (Invitrogen FluoSpheres) were added for visualization of the deformation of PDMS due to cell activity.

Mouse mammary epithelial cells (CLS-1, atcc) were added at saturating concentrations (in DMEM, 10% FBS, 1% pen/strep) to form a monolayer on the surface (necessary as single cells are compacted on soft substrates, [53, 12]). After a minimum of 12 hours, images were taken every 1 or 5 minutes for up to 36 hours on a Zeiss Axiovert 200M Confocal Microscope, while the samples were being kept at 37C and 5% CO<sub>2</sub>, and observed via a 25x oil immersion lens (Plan Neofluar 25x/0.80 1mm Korr DIC). To ablate cell contact, 200 $\mu\text{g}$  of anti-E-cadherin antibody (Invitrogen) was added at seeding, and retained in the medium. The cell nuclei were stained with a SYTO green nuclear dye (Invitrogen, SYTO 13 nucleic acid stain), and imaged at 488nm (568nm for the microspheres). Matlab particle tracking software (<http://physics.georgetown.edu/matlab>) was used to determine the centers of intensity (for both cells and PDMS-embedded beads), and assembles a trajectory for each centroid. For the ensemble of trajectories, we seek to identify timescales and lengthscales for both correlations in density and velocity. For the former, we use the standard van Hove correlation function,  $G(r, \tau)$ , which measures the changes in density as a function of elapsed time,  $\tau$  in radial coordinates [54], Eqn, 5.7. As will be seen in the results, the van Hove is typically highly symmetric, and we can therefore characterize it with a second order harmonic oscillator, and use regression to identify

spring and damping coefficients. (Eqn 3.3).

$$G(r, \tau) = \frac{1}{N} \left\langle \sum_{i=1}^N \sum_{j=1}^N \delta(r + r_j(0) - r_i(\tau)) \right\rangle \quad (3.1)$$

$$y'' + \eta(\tau)y' + \kappa(\tau)y = 0 \quad (3.2)$$

$$\zeta(\tau) = \frac{\kappa(\tau)}{\eta(\tau)} \sim e^{\tau/\tau^*} \quad (3.3)$$

The ratio of the spring coefficient to the damping coefficient,  $\zeta(\tau)$ , follows an exponential relationship, which will be characterized by the associated timescale,  $\tau^*$ . The larger  $\tau^*$ , the longer it takes for the harmonics to dampen out. Both the auto (Eqn 3.4) and the mutual (Eqn 3.5) velocity correlations decay as power laws, and are characterized by their scaling coefficients,  $\alpha$  and  $\alpha'$  respectively. The mutual velocity correlation is calculated both in the direction that joins a pair of cells ( $C_{\perp,\perp}$ ), their tangential directions ( $C_{\parallel,\parallel}$ ), as well as cross-correlating both ( $C_{\perp,\parallel}$ ). The subscripts 1 and 2 in Equation 3.5 refer to the two cells in a pair. We are interested in the lengthscale, so we chose a timescale of 1 hour, and characterize how at this timescale, the correlation decays for all separation distance,  $r$ . Generally, the only significant correlation is in the perpendicular direction, as the tangential direction is low, and roughly equal to the cross-correlation (which should be close to zero).

$$C_\tau = \langle v(\tau)^2 \rangle \sim 1/\tau^\alpha \quad (3.4)$$

$$C_{\beta,\gamma} = \langle \Delta v_{\beta,1} \Delta v_{\gamma,2} \rangle - \langle \Delta v_{\beta,1} \rangle \langle \Delta v_{\gamma,2} \rangle \sim 1/r^{\alpha'} \quad (3.5)$$

The velocity autocorrelation quantify the persistence of single cell movement in time, and the mutual velocity correlation relates how cells influence each other's movements in both time and space. When applied to the deflection of embedded beads, both functions indicate the deformability of the substrate. These equations are explained further in Chapter 5.

Upon seeding, cells will bind the substrate and each other, and form a uniform, and fully confluent monolayer. After a few hours, they begin to migrate in a coordinated fashion, often marked by coherent vector fields (3-3), as noted in numerous other studies, [4, 55, 56]. We calculate the change in these dynamics quantitatively within a narrow range of  $|G|$  (via  $\alpha, \alpha'$ , and  $\tau^*$ ), at a constant added surface adhesion protein concentration (although surface wettability may change adsorption below 1/50 PDMS concentration, [57]). The migration that characterizes each  $|G|$  is also reflected in the deformation of the substrate, both of the bulk, as visualized by the deflection of embedded fluorescent tracers, and the surface, as seen in the cell-induced deformation and reorganization of fluorescent adhesive protein (Fig 3-2). Qualitatively, there are three regimes of distinct observable behaviors (modes), which can be distinguished from each other by extent that the *cell monolayer* deforms the substrate during motion ( $|G| \sim |G|^*$ ,  $|G| < |G|^*$ ,  $|G| > |G|^*$ ). In the non-compliant, elastic limit ( $|G| > |G|^*$ ), the cells cannot deform the substrate, and the sheet is characterized by the slow evolution of long lengthscale coherent vector fields, particularly at low densities. The upper limit for cell-induced substrate deformation is  $\sim 300Pa$ . From this limit to  $\sim 50Pa$  defines the second regime ( $|G| \sim |G|^*$ ), where the sheet can induce short ranged deformation. Below this lower limit however ( $|G| < |G|^*$ ), the substrate is largely viscous, and the substrate is easily deformed on lengthscales greater than  $1000 \mu m$ . In this third regime, an instability is reached (Fig 3-12), and the sheet begins to slowly aggregate (Fig 3-17), deforming and dragging the substrate with it (to be distinguished from aggregation on soft, but elastic substrates [53]). Aside from the dynamic instability (aggregation), there is also a structural defect. There appear tension-induced holes in the sheet, which retain functional E-cadherin at the periphery, but nevertheless grow with time. During this non-equilibrium event, locally the sheet appears to have broken symmetry and slides, while globally, invaginations and structural inhomogeneities can occur that punctuate aggregation. The time-dependent resistance to shear that characterizes the point immediately preceding this behavior coincides with physiologically relevant rheology.

We further show that the phase behavior and sheet dynamics are contact-dependent, and variable upon alteration of the coupling between sheet and bulk, the linkage of the adhesive protein to the substrate surface.

### 3.3 Coupling of monolayer and bulk

The velocity autocorrelation  $C_\tau$ , differentiates random movements from constant paths, by the identification of timescales (or scaling laws for power law behaviors). The associated time scalings of cell movement and traction-induced bulk bead deflection respectively, converge as  $|G|$  decreases, until the instability is reached (Figure 3-4). This reflects a tight coupling between the motion of the cells, and the stresses transferred to the bulk substrate. Below  $\sim 67Pa$ , monolayer and bulk  $C_\tau$  track each other for nearly all timescales, reflecting long-ranged, higher-order movement near the onset of the instability. Covalent linkage of the adhesive protein however, disrupts this coupling, and there is a separation of timescales (correlations relax differently in the monolayer than in the bulk) even still on compliant surfaces (Fig 3-5). In this scenario, all surface rearrangement is ablated (Fig 3-2D). Alternatively, the addition of antibody against cell contact does not always alter the relative scaling of each correlation, but causes a faster relaxation in both. Above 67Pa, in the less compliant regime, there is little coupling of correlation between cell movement and substrate traction after just a few minutes. As cells attract each other on compliant surfaces, low density sheet cannot be achieved, and further, they retain little density dependence as compared to non-compliant surfaces.



### 3.4 Correlated Dynamics follow a second-order transition with substrate viscoelasticity

With reduced resistance to shear, the motion of the cell is more likely to persist, but accrues nearly no net movement, as the density is high. The trajectories are short-ranged, yet the instantaneous velocity is higher, suggesting a  $|G|$  induced transition between mechanisms that are responsible for each type of movement. As ablated cell contact on non-compliant surfaces does less to alter motion as it does on more compliant surfaces (Fig 3-6), there is clearly an increased role for cell contact in this (newly defined) motility of cells within the sheet on compliant substrates, one where cells are less autonomous than on surfaces with high resistance to shear.

By a mutual velocity function,  $C_{\beta,\gamma}$ , we characterize this transition by how cells influence each other's motion in time and in space. We therefore calculate this function, taken in the direction that connects each pair of cells, and use its scaling behavior as an order parameter (Fig 3-8,3-9). The magnitude and scaling behavior of these correlations vary again with  $|G|$ , and with cell contact. The power law exponent (at minimum timescales for motility and when  $G'$  and  $G''$  for the PDMS approach the Matrigel, 1hr) ranges from  $\sim 1/r^\alpha$ ,  $\alpha = 1.6$  to  $\alpha = 0.3$ , when the  $|G|$  is varied from the kPa range, down to 10's of Pa, where  $G'$  is also comparable to  $G''$ . A strong decay says cells can influence each other's velocity at close range, but that drops off very steeply even a couple of cell diameters away. An exponent less than one shows that cells can influence each other's movement over very large separation distances. Further, if we map each of these coefficients from the kPa range down to 10's of Pascals, there is a clear transition in dynamic behavior that occurs near  $|G^*|$ . Thus, the order parameter varies continuously with  $|G|$ , mirroring a second-order phase transition. Further, at the onset of this transition, the correlation appears relatively density-independent, purely a factor of the mechanics of the substrate (Fig 3-9B.). The scaling factor for the mutual measurement is a function of density on non-compliant surfaces, but is not correlated to density at all for the compliant surfaces (defined as having convergent

timescales in the velocity autocorrelation).

### 3.5 Substrate Viscoelasticity inversely modulates positional and dynamic correlation

Shifting towards a less autonomous, more mutually collective (contact-dependent) paradigm, we can consider the system a two-dimensional fluid with enhanced 'potential' between cells. Thus, we are interested in the positional organization and correlations of density that may exist within the plane (again, as there is little net displacement). By calculating the van Hove correlation function (Eqn 5.7), and treating it as a damped harmonic oscillator (Eqn 3.3), we can fit the spatial component, and we can extract damping and spring coefficients for epithelial organization on substrates that range in viscoelasticity.

Then, we can see how these coefficients evolve in time, and extract a characteristic timescale that represents the relaxation in the long-range spatial harmonics, or geometric organization of cells within the epithelial sheet. What we find is that as  $G'$  of the substrate decreased in proportion to  $G''$ , the density correlation, decreased at long lengthscales ( $\tau^*$  greater for non-compliant substrates, 3-10). On highly elastic, and rigid substrates ( $\sim kPa$ ), positional order was maintained over hundreds of microns, and on timescales of hours. On more compliant substrates  $|G| < |G^*|$ , with comparable  $G'$  and  $G''$ , positional correlation was dampened over only a couple of cell diameters. Interestingly, this behavior appeared partially density-independent for moduli below  $\sim 200Pa$ . We can directly connect this to the deformation of the substrate by the cells, by comparing the temporal decay of the velocity autocorrelation of embedded, submicron beads, with the timescale of relaxation in the spatial harmonics of the epithelial sheet. As the autocorrelation in bead velocity decays strongly for  $|G| > |G^*|$ ,  $\sim (1/\tau^\alpha)$ ,  $\alpha = 1.5$ , but retains correlation ( $\sim \alpha = 0.7$ ) for  $|G| < |G^*|$ , it

becomes clear that deformation of the substrate plays a large role in the dynamics of cell organization on a massive scale. Thus, it is clear that as the magnitude of  $|G|$  decreases, with important mention of the increase in  $G''$ , that the lengthscales of geometric organization (and not just velocity correlation) become shorter, and the timescales faster.

Further, the correlation that is endowed by the substrate to the organization and dynamics of the epithelial sheet are also conferred by the surface, as there is increased texturizing and reorganization of the adhesive protein, as the surface becomes more deformable (similarly seen in [58]). This is evidenced in the complex patterns, and even wave-like propagation of texture across hundreds of microns (Fig 3-2B).

On non-compliant substrates, cells are propelled autonomously, by traction against the surface. In doing so, they retain long-range positional order consistent with mutual exclusion of hard disk systems at the same density (Fig 3-15). At equivalent, high densities, there is low correlation over long timescales (via  $\alpha, \alpha', \tau^*$ ), and retain more basal contact with the surface, with flat, elongated structures (Figure 3-14, lamelopodial on non-compliant, filopodial on compliant). At lower densities, there is longer scale coherence in their movement. Compliant surfaces however, below the critical shear modulus ( $|G^*|$ ), are highly correlated in time, but have shorter ranged coherence in their movement. Their motion is facilitated by destabilization (reorganizing surface, less contact with the surface) with respect to the surface and driven by cell-cell contact. Their cadherin distribution further reflects the transition to non-autonomous migration, as it is similar to an EGTA-treated non-compliant substrate where cells are no longer motile. Further, by the van Hove relation, even the distinction between cells is less clear, as the density correlation is short-ranged (giving the appearance of a cellular 'continuum'). Thus, the correlated state is distinguished dynamically, by the distinct spatial organization within the sheet, its morphology, and most notably this destabiliation with respect to the surface.

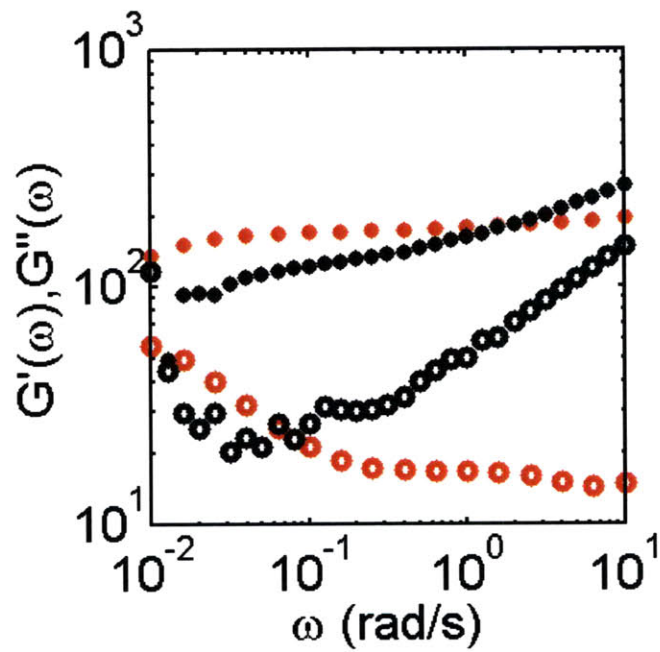


Figure 3-1: BASAL LAMINA ANALOG. Rheology of Matrigel (red), and 1/80 PDMS (black). Storage ( $\cdot$ ), Loss ( $\circ$ ) Moduli. For this composition of PDMS, the rheology nearly matches that for Matrigel, for low frequencies. We stop our comparison at  $10^{-1}$  radians/s, as below this frequency, we are uncertain concerning the rise in  $G'$  and  $G''$ .

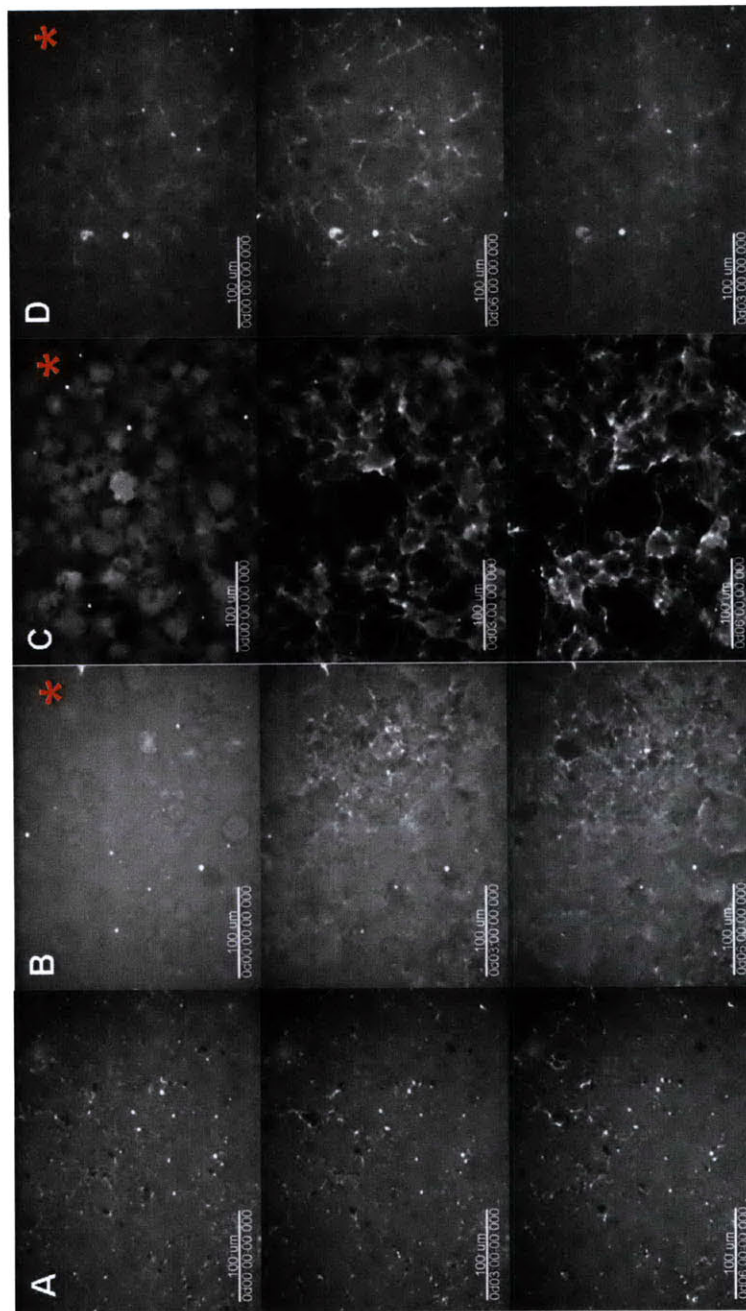


Figure 3-2: SURFACE PROTEIN AS A FUNCTION OF STIFFNESS. FITC-stained gelatin bound to fibronectin, attached nonspecifically (A-C) or covalently (D) to PDMS in a ratio of (A) 1/10, or (B,C,D) 1/80, which is the critical combination of stiffness and wettability that characterizes the most correlated state, and is thereby marked with a red star.

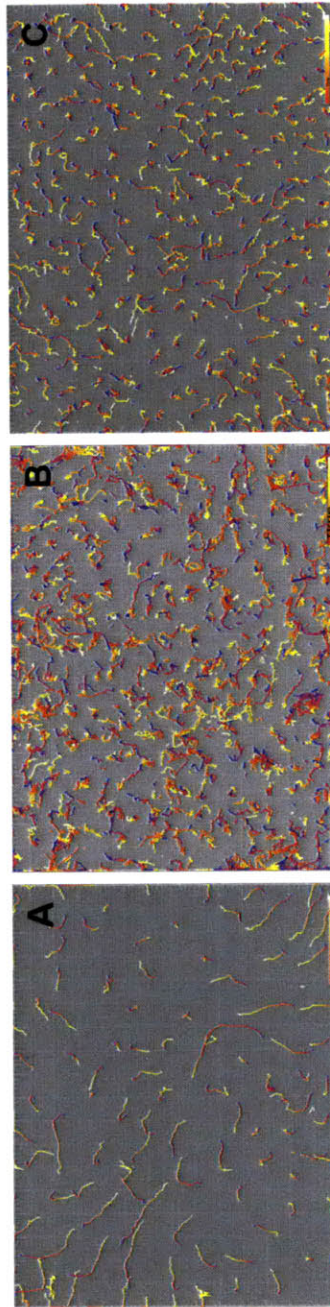


Figure 3-3: CELL TRAJECTORIES. Trajectories of dense cell populations on non-compliant (1/10) low density (A) and high density (B) or compliant (1/80) high density (C) surfaces. At low densities on non-compliant substrates, the trajectories are very coherent and coordinated. High density generally ablates this coherence on non-compliant substrates, but small domains of highly coordinated movement persists when the substrate is compliant.

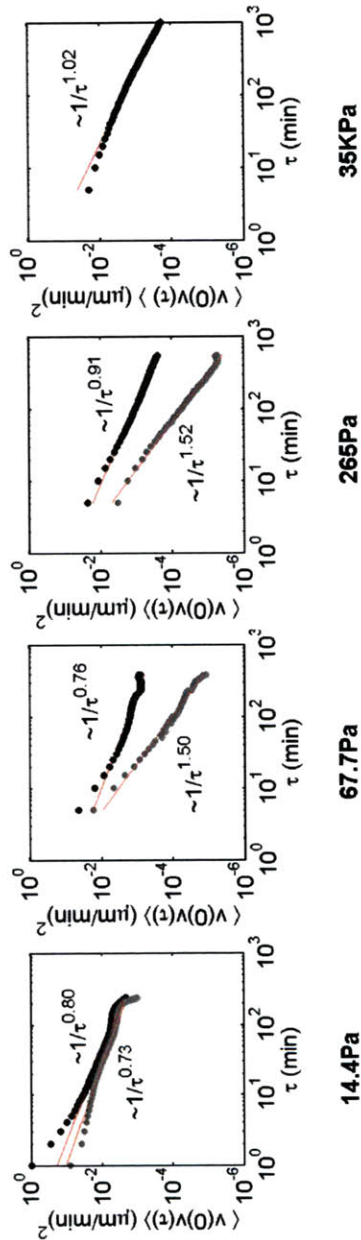


Figure 3-4: COUPLING OF CELL MOTION AND BULK MOTION. Velocity autocorrelations for cell movement (black) and bead displacement (gray) in substrates of varying viscoelasticity. As the stiffness of the surface dips below 67.7 Pa, the timescales converge, with the substrate movement mirroring the cell movement.



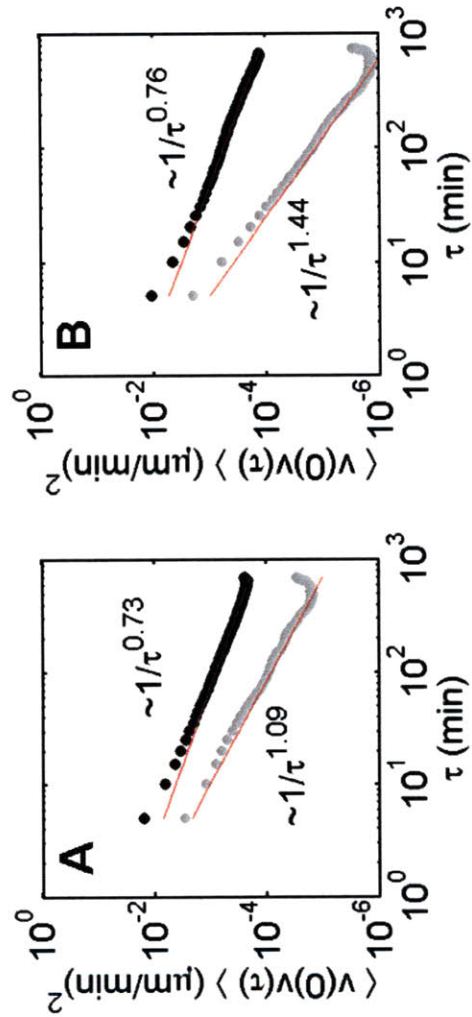


Figure 3-5: DECOUPLING OF CELL MOTION AND BULK MOTION. (A) Cell autocorrelation on 1/80 PDMS, with fibronectin covalently linked. (B) Cell autocorrelation on 1/80 PDMS, with covalently linked fibronectin, and 200 $\mu$ g anti-E-cadherin antibody to block cell-cell contact. The persistence of cell motion is not altered on this non-compliant substrate with the removal of cell-cell contact, but the correlation is no longer conferred to the substrate (same bead scaling as 1/10 PDMS composition).



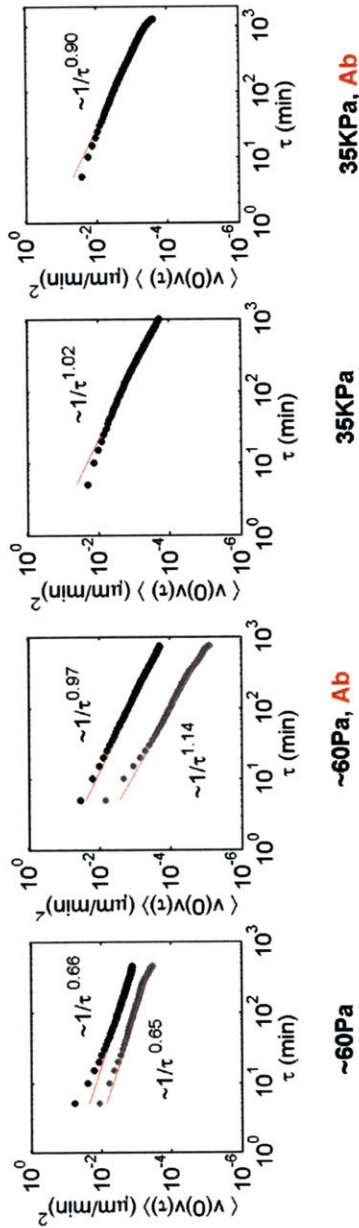


Figure 3-6: COUPLING BETWEEN CELL MOTION AND BULK AS A FUNCTION OF CELL CONTACT. Velocity autocorrelations for cell movement (black) and bead displacement (gray) on both hard (and elastic) and soft (and viscous) substrates. For hard, elastic substrates, the absence of cell-cell contact, does not alter the persistence of single cell motion. However, on soft substrates, blocking E-cadherin separates the timescales between the cell motion and the persistence, as well as decreasing the magnitude and scaling of the autocorrelation function.

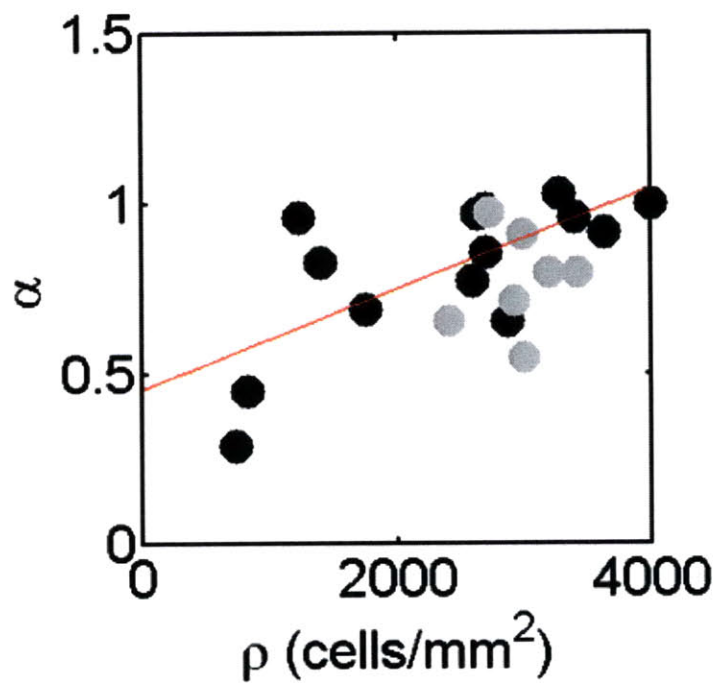


Figure 3-7: PERSISTENCE AS A FUNCTION OF DENSITY. Both deformable (gray) and non-deformable (black) substrates have roughly the same scaling behavior for all highly confluent densities. Cell motion persists for longer (and hence have a lower power law exponent) when the density is low, which is not possible on deformable substrates, as cells will compact.

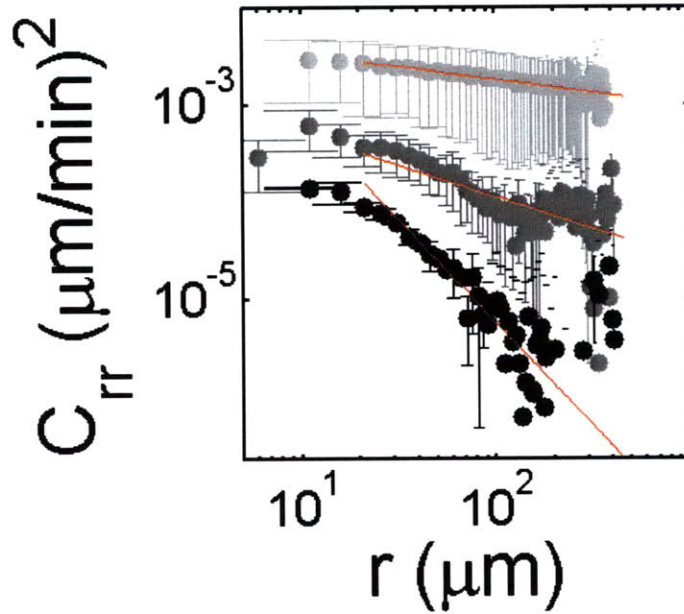


Figure 3-8: DISTINCT VELOCITY CORRELATIONS. Mutual Velocity Correlation Functions (1hr), for dense cell populations on 14.4 Pa (light gray), 287 Pa (med gray), and 35 kPa (black) substrates.

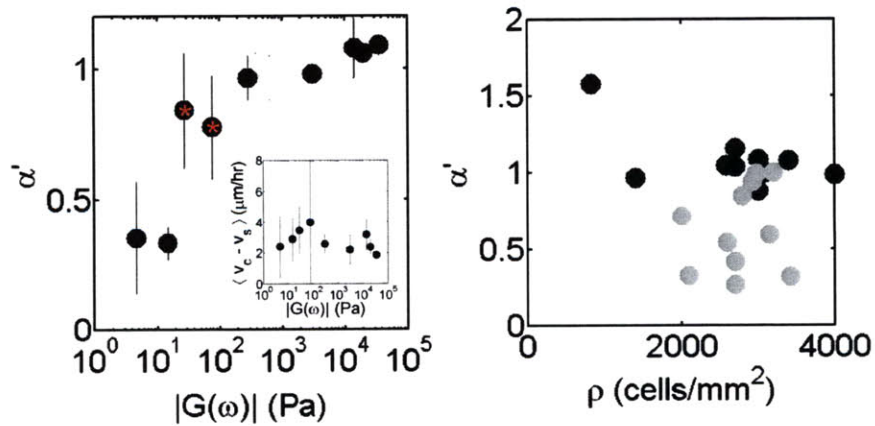


Figure 3-9: SECOND ORDER TRANSITION IN MUTUAL CORRELATION. Taking the scaling exponent,  $\alpha'$ , of the mutual velocity correlation function for each value of  $|G|$ , maps out a continuous transition from the non-compliant and less correlated ( $\sim 1/r^{1.0}$ ) to the compliant and more correlated ( $\sim 1/r^{0.3}$ ). The inset is the mean velocity of the cells, with the velocity of the beads subtracted, as the instability causes a net drift. This relative velocity is constant for all measured moduli.

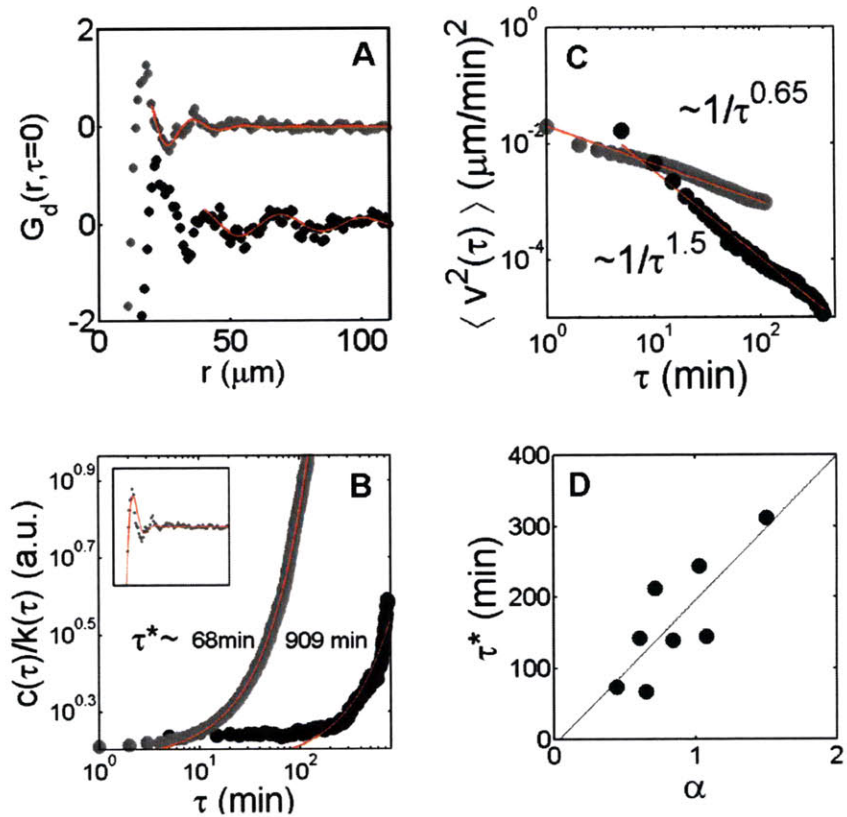


Figure 3-10: VAN HOVE CORRELATIONS. (A) radial distribution function for two systems, compliant (gray) and noncompliant (black). (B) Timescale of the evolution of the spring and damping constants, characterized by time evolution of their ratio,  $\zeta = \kappa/\eta \sim t^{\tau/\tau^*}$ . (C) Time-scaling of beads in PDMS. (D) Relationship between timescale of cell organization and timescale of bead displacement.

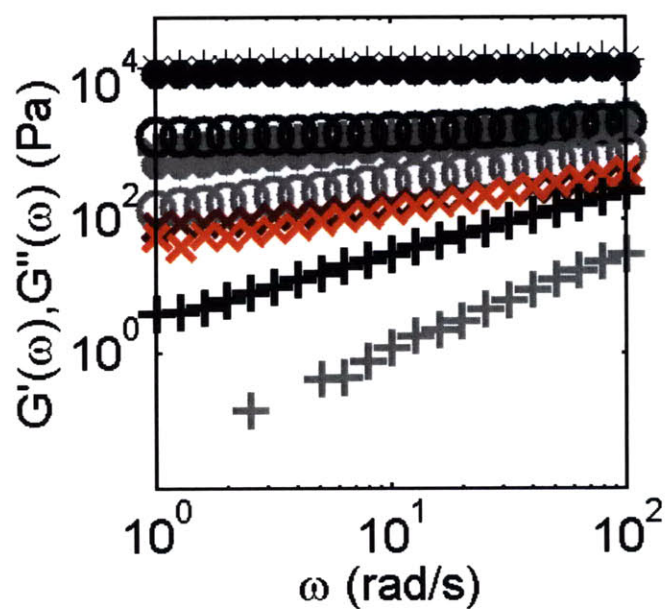


Figure 3-11: PDMS RHEOLOGY. Rheology of PDMS of different curing agent concentrations.  $G'(\omega)$  dark,  $G''(\omega)$  light, and follow: 1/10, 1/20, 1/40, 1/80 (red) and 1/160.

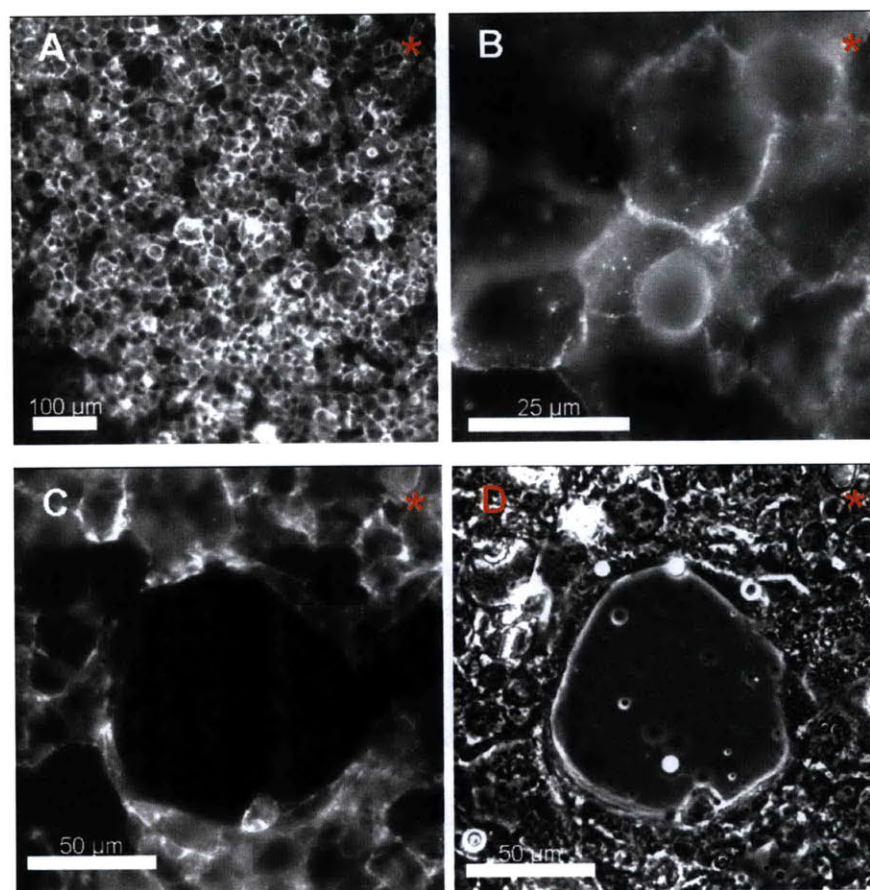


Figure 3-12: STRUCTURAL INSTABILITY. The onset of the most correlated state on compliant (1/80) PDMS is also accompanied by holes that open up in the sheet, which can grow in time. (A) 10x, (B) fluorescence image of E-cadherin on a 1/80 PDMS sheet. On the same sample, local tension induces these instabilities, which retain functional E-cadherin around the circumference (C) fluorescence, (D) bright-field.



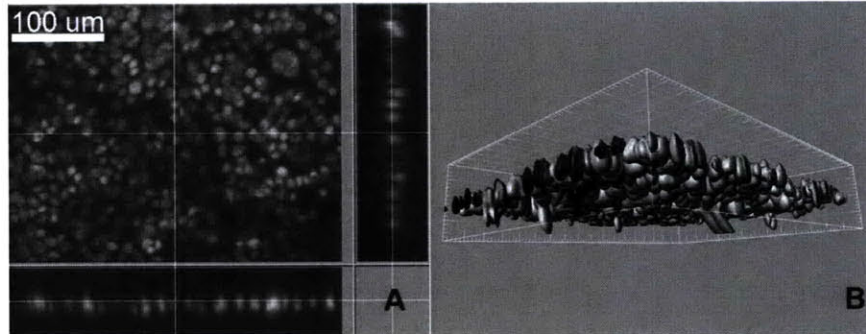


Figure 3-13: SHEET REMAINS FLAT. (A) 25x, 3D image of stained nuclei on nearly pure prepolymer (1/200). For long times, the cells retain their sheet-like character, although scattering is possible by moving underneath other cells (3D reconstruction and contour plot, B).

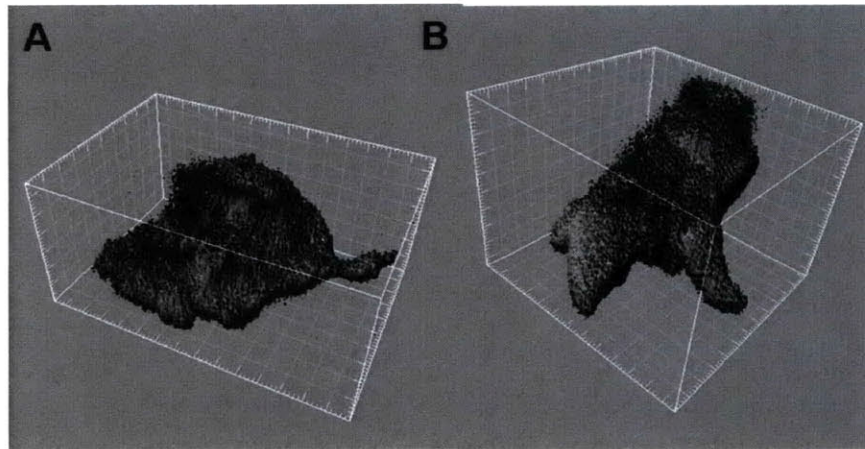


Figure 3-14: 3D MORPHOLOGY FOR DIFFERENCE STIFFNESSES. Cells on non-compliant surfaces,  $|G| > |G^*|$ , (A) are spread, while cells on compliant surfaces,  $|G| < |G^*|$ , (B) create long projections and have less interfacial area with the surface (grid =  $2\mu\text{m}$ ).

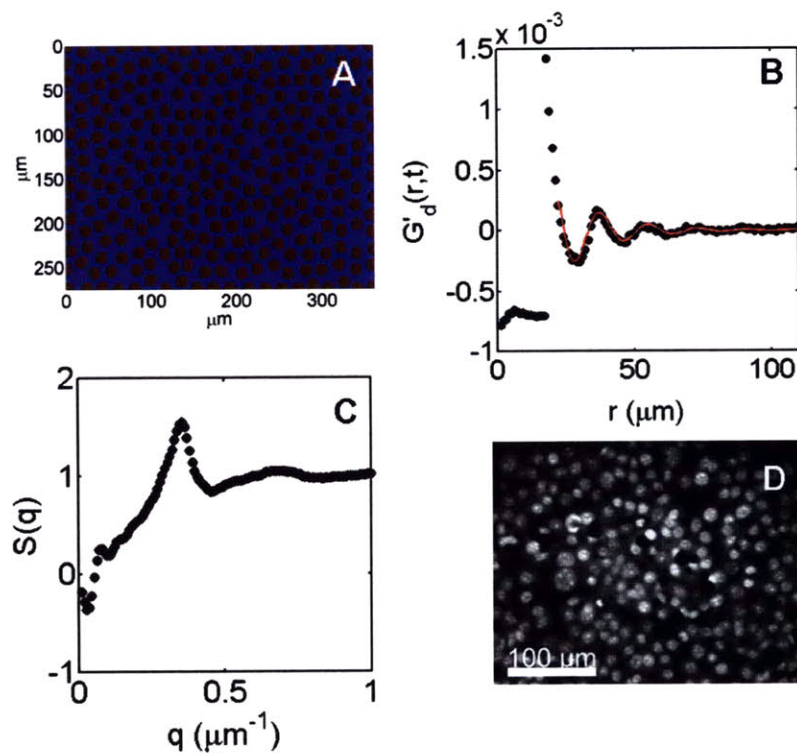


Figure 3-15: CONTROLS FOR THE VAN HOVE CORRELATION FUNCTION. Dynamic Monte Carlo simulation (A) of the same size image as most experiments, (D), at high density yields the RDF in (B) and spectrum in (C).



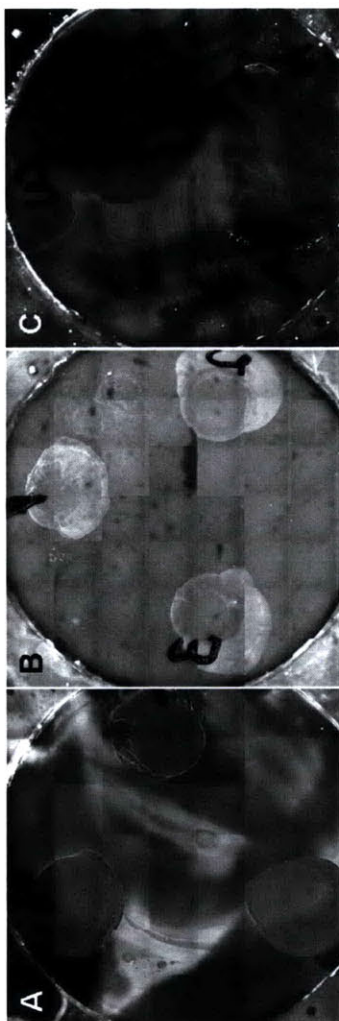


Figure 3-16: FIBRONECTIN ADSORBED TO PDMS. (1) 0.4 mg/ml, (2) 0.2 mg/ml, (3) 0.1 mg/ml stained fibronectin on 1/10, 1/60, and 1/160 PDMS, spun onto Mattek dishes. On the 1/10, and 1/60 PDMS, the fibronectin is rigidly adhered. On the 1/160 plates, where the PDMS is nearly purely viscous, the fibronectin does not stick, and instead is diffuse across the plate.

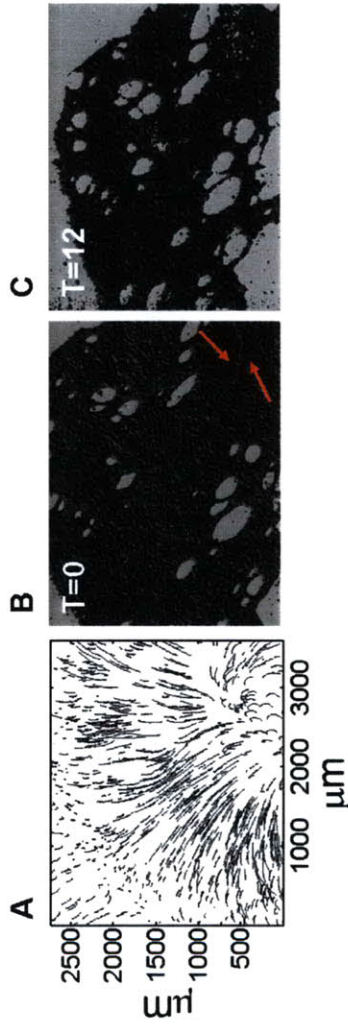


Figure 3-17: DYNAMIC INSTABILITY. On compliant substrates,  $(\mu/80)$ , the sheet will slowly begin to aggregate. This results in the deformation of the substrate over millimeters (A). Structural inhomogeneities appear during the collapse, such as the appearance of holes in the sheet, and invaginations (B,C).

# Chapter 4

## Motion of Epithelial Sheets as a function of Population Size

### 4.1 Introduction

In the previous chapters, we have established unequivocally a strong density dependence on both equilibrium and non-equilibrium sheet behaviors. With increased density, there is increased cell contact, and that the extent of that contact, the adhesivity will restrict the degrees of freedom available for fast, and correlated motion on non-compliant substrates, but facilitates higher-order movement on compliant substrates. A subtle issue however, is whether or not these effects are actually purely density-dependent, or actually depend upon the size of the population itself (as dense populations also have more cells). When we again reflect on *in vivo* epithelial sheets, they each have a characteristic size. Back to our paradigm example, the intestinal epithelium, each crypt-villus axis has a particular length, which does not vary over orders of magnitude. Thus, perhaps intertwined into the motion of the sheet is the absolute size. Thus, in this chapter, we aim to isolate separate coherent cell sheets, equal in their densities, but varying in the population.

## 4.2 Materials and Methods

The goal is to be able to image, in the same frame, multiple populations that vary in overall population, but have the same density. In this sense, we will be able to statistically discriminate the movement of each separate population, and calculate the influence of the size of this population on the velocity probability distribution (as our correlation function analyses in previous sections depend on homogenous movement, unbiased in any direction).

We can prescribe cells to two-dimensional surfaces in various shapes by soft lithography. Briefly (and outlined in detail at the end of the chapter), we design by AutoCad (2007, Autodesk) a mask, which will be partially opaque, and partially transparent to ultraviolet light. This mask, when printed onto a transparency slide (which has feature resolution as low as  $8\ \mu\text{m}$ ), is placed over a 5" silicon wafer, which has had SU-8, photosensitive resist spun on top of it. The design in the mask is opaque, so that when placed under an ultraviolet lamp, the light crosslinks that polymer where the design is not, making it hard. Then, the rest of the photoresist that was covered by the design is removed, leaving behind a raised, solid feature, whose thickness depends on the particular type of SU-8 (I use  $25\ \mu\text{m}$ ). Then, by pouring in PDMS (1/10) onto the mask, and baking it, you will remove a solid PDMS mold, which has the design, as a raised pattern. This raised pattern is the stamp, which is inked with fibronectin (1 mg/mL), and immediately placed in conformal contact for 30s with a PDMS surface (of varying stiffness) which has been oxidized in an air plasma machine for exactly 40s (depends on your machine), for transfer of the protein.

After transferral of the protein, the rest of the surface has to be made non-adhesive to cells. If we are transferring the protein non-specifically, we use Pluronic, P127 (1%) and F68 (4%) in a 1:1 volumetric ratio, and immerse the stamped dish in this solution for upwards of 20 minutes. Then, cells can be added by standard tissue culture techniques. This will passivate the surface, so that cells will only bind to the regions

that have the exposed fibronectin, forcing them to conform to the specified geometry. If we are attaching the protein covalently, then the surface must be aldehyde terminated. Upon application of the stamp, the fibronectin will bind covalently, through amines present in the protein. Conformal contact should be made for upwards of 30 seconds. Then, we add a 1% solution of PEG-amine. The PEG-amine will react with the aldehyde at the surface, and form a permanent, covalent linkage, with the PEG sticking up into solution. This reaction can be (but is not necessary) catalyzed by triethylamine.

To verify that the protein has been transferred non-specifically, I add 200  $\mu\text{M}$  of FITC-pig skin gelatin, which binds to fibronectin, but is resisted by the pluronic at the surface. This gives nice contrast, which can be seen in 4-1. After the cells are added, and are firmly adhered, they are washed to reduce the number of cells that may lie between 4-2. The cells may have to be washed multiple times, as the distance between features is as small as 100  $\mu\text{m}$ , and so it is possible that clumps of cells from the trypsinization may lie between features, and if left unwashed, may spread between them.

The cells were stained again with 1:1000 Syto or CMFDA, just like in the substrate mechanics studies. We generally prefer CMFDA, as it is generally less lethal to cells, but SYTO obviously gives better contrast to the nucleus for tracking, and as we are now imaging at 10x, instead of 25x, we cannot do without this resolution. Nevertheless, we use both, again to make sure that we are not introducing artifacts into the movement of the cells. Thus, after 20-30 minutes of SYTO/CMFDA stain, the dishes are washed, and left in the incubator for minimum of 30 min. Then, they are placed on the scope, inside of the same chamber, which feeds 5%  $\text{CO}_2$  at 37C. The cells were then imaged for upwards of 10 hours.

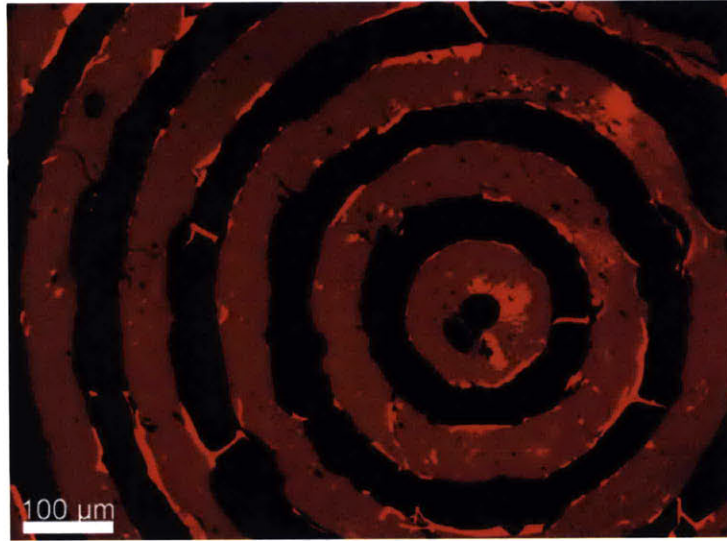


Figure 4-1: STAMPED FIBRONECTIN. 1mg/mL Fibronectin transferred nonspecifically to 1/10 PDMS spun onto a Matek dish, and stained with 1ug/ml FITC-pig skin collagen.

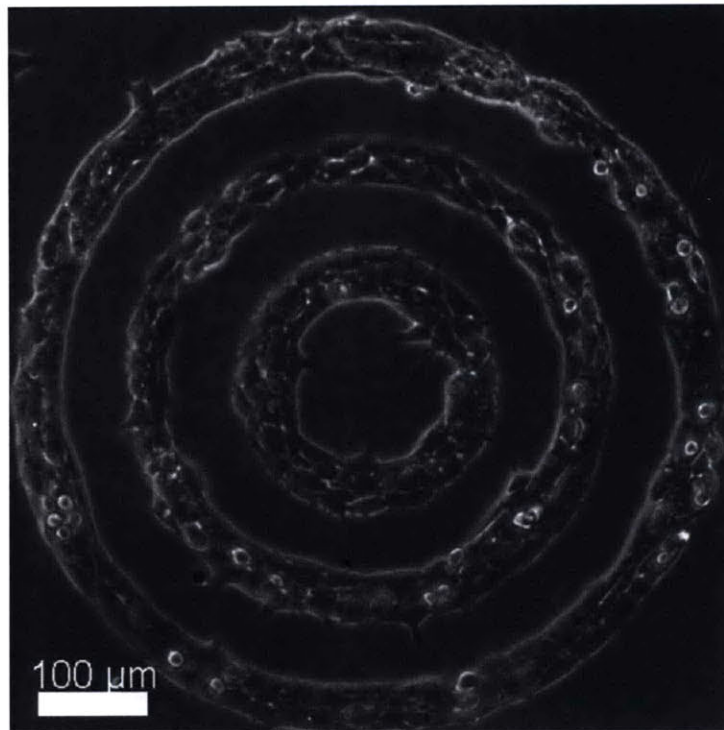


Figure 4-2: CELLS BOUND TO STAMP. Brightfield image of Mouse Mammary Epithelial Cells bound nonspecifically to 1/10 PDMS.

### 4.3 Dynamics vary only with density, not population

After assembling the trajectories of movement, but before mathematical analysis, there emerge interesting qualitative effects. First, we notice that the longest, and most persistent trajectories are always along the border (Figures 4-4,4-6). In some cases, cells can move hundreds of  $\mu\text{m}$  in 12 hours. The fastest movement is always localized to the border. From the conclusions in Chapters 1 and 2, it the most likely argument, is that considering that we have already established that cell contact is generally not conciliatory towards fast, directed movement on non-compliant surfaces, there is clearly fewer neighbors for cells along the boundaries. Further, their basal adhesions are likely less stabilized, as they are at the border between the fibronectin patch which was stamped, and the pluronic, or PEG passivated surface immediately adjacent.

Quantitatively, we can again begin with the probability density function (PDF) for the velocity. A separate PDF is calculated for each subpopulation, and is seen in figures 4-8,4-7. From the overlap, we can see that there is no difference in their non-gaussian character, or the existence of the small, fast subpopulation. Thus, based on the cell speeds, there is statistically no significance in their distributions. Further, there appears to be little distinction rather than overall magnitude of the velocity for high density populations versus lower density populations.

We can use also some of the same metrics that were used to discriminate the isotropic, or non-equilibrium measurements. The smallest dimension is only  $100 \mu\text{m}$ , so the mutual velocity autocorrelation function for example, is only valid below this range, and questionably so. Nevertheless, just to get an idea of the level of correlated motion, or rather the extent that cells can influence each other's motion over space, can be seen in figure 4-9.

## 4.4 Confinement on Substrates of Varying Rigidity

Nonspecific stamping is limited to PDMS surfaces above the composition 7/400 (Figure 4-12). At this level, the protein will transfer, but cells will easily pull it off of the substrate. Below the composition, and the protein will not transfer. Covalent transfer works as as low as 3/200, and the cells cannot remove the protein. However, I surmise that we are modifying the stiffness of the surface when we oxidize it. This step is necessary for activating the surface, so that it can be aminated, and subsequently reacted with glutaraldehyde for attachment of fibronectin. The reason for this hypothesis, was that when oxidizing by plasma, if exposed too long, the surface will crack (Figure 4-10). Presumably, after plasma treatment, the surface is a brittle layer of reactive oxygen species, whose physical properties are different than the bulk, and so applied heat makes the bulk expand, cracking the surface. This may still be a problem, even if the surface isn't overexposed. There may be an alteration to the surface stiffness, and therefore the stability of cells on the adhesive pattern is not just because the protein is attached strongly to the bulk, but that the surface is stiffer in addition to a covalent attachment. With chemical oxidation, this cracking never occurs, but nevertheless, we assume that the generation of the oxide layer is the problem, and at that level, is not visible by eye, but would have an effect on the migration of cells.

## 4.5 Appendix

### 4.5.1 Free Space sufficient for generating "Purse-String"

Aside from cell crawling as a mechanism for wound closure, there is also the actin bundle "purse-string", which generates a contractile ring around the denuded free space, and physically constricts, closing the gap. This mechanism only occurs for relatively small wounds, of free space on the order of just a few cell diameters. In



a similar fashion to the Chapter 2, where we were interested in whether or not free space was sufficient to induce migration, as a side study, we were interested in also seeing if free space was sufficient for the generation of the actin contractile ring that we see in wound healing experiments. The smallest ring in the patterning, has an inner diameter of only 50  $\mu\text{m}$ , which is on the order of 5 to 10 cells, at high density. After staining for actin, we see that there are long, thick actin bundles many times the lengthscale of a single cell that wrap around the center and the inner diameter of the ring, but not around the outer diameter (Figure 4-11). This would be implicative of increased tension towards the inner diameter, rather than the outer diameter. It is therefore evident that free space is sufficient for generating the contractile ring, and therefore not a consequence of the wound.

## 4.6 Protocols

### 4.6.1 Preparing Aldehyde Terminated PDMS Surfaces

This method is for preparing a surface for covalent attachment of fibronectin during the application of the inked stamp. I have modified a standard method for the silanation of coverslips, so that it works for functional attachment of protein to PDMS, with cell exclusion chemistry, to confine cells to the stamped region alone, for up to weeks. The APTES portion (Step 5) of the protocol was taken from Winston Timp, PhD, 2008.

#### Reagents

1. 35%  $H_2O_2$ , HCl
2. (3-aminopropyl) triethoxysilane (APTES)
3. 100% ethanol
4. Acetic Acid
5. Glutaraldehyde (unopened!)
6. PEG-amine (MW 5000)
7. Triethyl-Amine

#### Preparing the Surface

1. Spincoat the PDMS onto a 20mm round coverslip Mattek Dish.
2. Bake the dish for upwards of 1 hour, at 65C.
3. The first step is to oxidize the surface, to make it reactive to the silanation. This can be done either by plasma, or by more harsh treatments, like  $H_2O_2$ /HCl, or Pirahna. I have found that plasma works, but is less reliable. Plasma is quick, as treatment should not exceed 1 minute. I have found that 45 seconds (depends on your particular plasma machine) works well. If the plasma is left on too long,

the surface will crack, and become non-reactive. My preferred method is to add 35%  $H_2O_2$  to HCl in a volumetric ratio 9:1, and immerse each plate in this for 10 minutes, at room temperature. Longer than this, and bubbles will start to form in the PDMS.

4. Remove the 35%  $H_2O_2$ /HCl, and wash once in de-ionized water.
5. Immerse the surface in 2% (3-aminopropyl) triethoxysilane (APTES) in 95% ethanol for 2 hours. The APTES should have pH 5, which can be accomplished by the addition of Acetic Acid. I usually prepare 10mL (for 3 dishes), which comprises 9.5mL EtOH with 0.5mL  $H_2O$ , then removing 250 $\mu$ L, and adding back 50 $\mu$ L of Acetic Acid, and 200 $\mu$ L of APTES.
6. Wash the dish 3x in de-ionized water.
7. Add 5% glutaraldehyde in 1x PBS, and set at room temperature for 2 hours.
8. Wash the dish 3x in de-ionized water, let the surface dry in the hood.
9. Press the Stamp for 30 seconds, and remove (see below for details on how to prepare the stamp).
10. Immediately immerse the dish in 10% PEG-amine, and incubate at 37C for minimum of 30 minutes. This will covalently link the surface with non-adhesive polyethylene glycol (MW 1000), so that cells cannot attach to the regions that were not stamped by the fibronectin. This can be catalyzed with Triethyl-Amine (TEA).

## 4.6.2 Stamping onto PDMS

### Reagents

1. Alexa Fluor, malleimide dye (Molecular Probes)
2. 1mg/ml Fibronectin
3. F68, P127 Pluronics

### Preparing a Stamp

1. Add 50 $\mu$ L Alexa Fluor Dye + 200  $\mu$ L 1mg/mL Fibronectin for 3 hours at room temperature.
2. Add 50  $\mu$ L of dye/protein mixture to the stamp for 30 minutes.
3. Place the (1:10,7:400) PDMS covered Mattek inside the air plasma machine for (3 minutes, 45 seconds). The softest PDMS that will still adhere the fibronectin is 7:400. At this composition, cells can pull this up.
4. Wash stamp with deionized water, and blow dry with compressed air.
5. Press stamp gently onto surface immediately, for 30 seconds.
6. Add 1mL 4% P137 and 1mL 4% F68 Pluronics immediately to the surface for 15 min.
7. As an alternate to staining your own fibronectin, you can FITC-Pig Skin Gelatin adds great contrast to the adsorbed fibronectin. Add directly to the Mattek dish after the Pluronics treatment, at 200 $\mu$ M in PBS. I do not stamp collagen directly, as it does not transfer well.
8. Mouse Mammary Epithelial Cells are added at saturating concentrations after being trypsinized so that there are no clumps. This ensures that no clumps can lie between patterns, overtop regions excluded with Pluronic. Leave the cells for about 8 hours, and then wash off. It is better to saturate the stamp with cells,

than to have a low density, and wait for them to grow to occupy the stamp, as I find that the Pluronic is perfectly stable for up to a week. Thus, if cells are still growing on the stamp for that long, they may begin to walk out of the stamp.

### 4.6.3 Ninhydrin Test for Primary Amines

The following procedure is a qualitative method for detecting the presence of primary amines on PDMS samples, after the addition of the aminopropyl silane. This protocol was adapted from: <http://openwetware.org/wiki/SolidPhasePeptideSynthesis>.

#### Reagents

1. 15g phenol in 4.5mL ethanol
2. 0.0002M KCN in pyridine
3. 500mg ninhydrin in 10mL ethanol

#### Procedure

1. Place a small piece of the treated PDMS inside an eppendorf tube.
2. Prepare the following mixtures, (phenol/ethanol,KCN/pyridine,20 $\mu$ L Ninhydrin/EtOH) in the volumetric ratio (2:2:1) to the eppendorf.
3. Heat the eppendorf to 95C for 5 minutes. The amination was successful if there is a blue color.

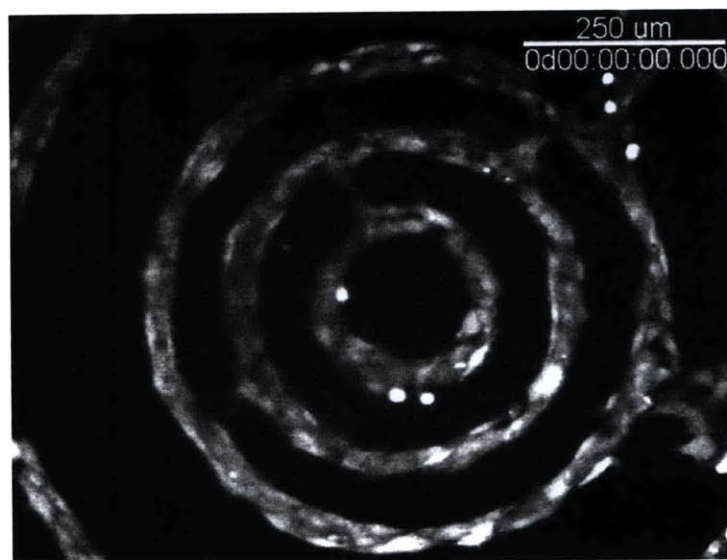


Figure 4-3: LOW DENSITY CELL POPULATION. 1/10 PDMS treated with 5 min  $H_2O_2/HCl$ , 10% PEG-amine, to generate the reactive/passivated surface. 1mg/ml fibronectin added to stamp and transferred. Mouse Mammary Epithelial Cells bound, and stained with 1/1000 CMFDA.

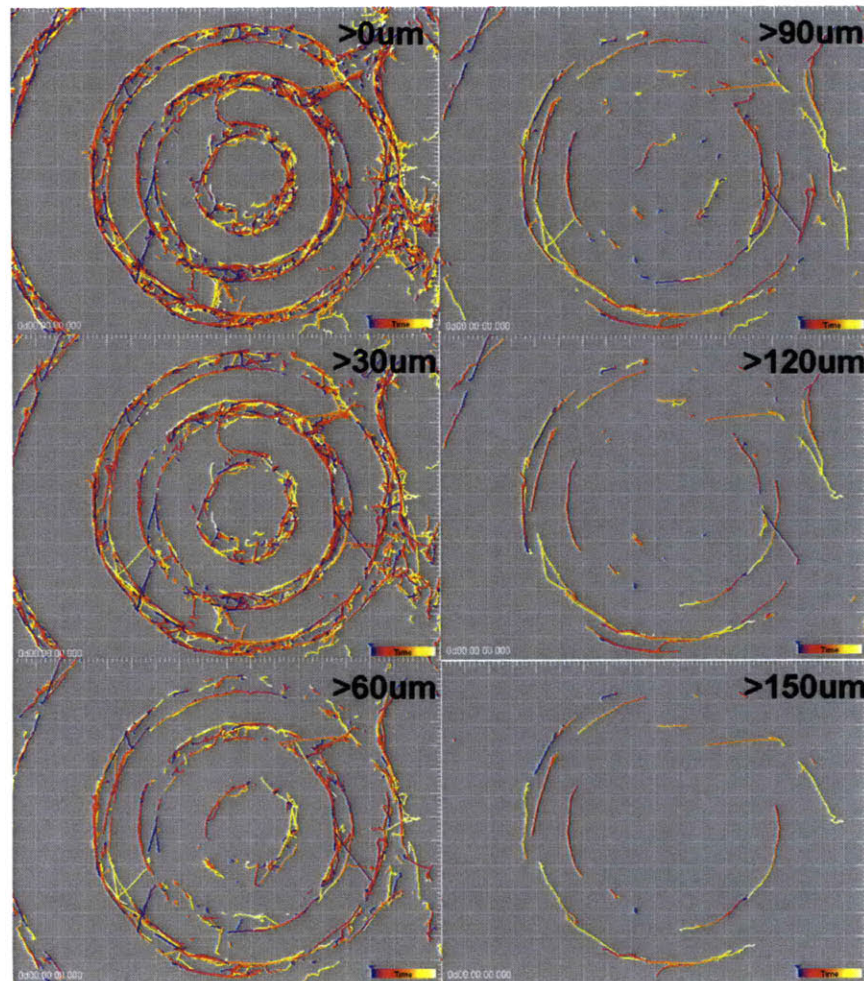


Figure 4-4: **LOW DENSITY CELL TRAJECTORIES.** Trajectories of cell movement on stamped pattern for the low density system. Low density epithelial cell populations under confinement are marked for their adherence to the boundaries, and high speed.

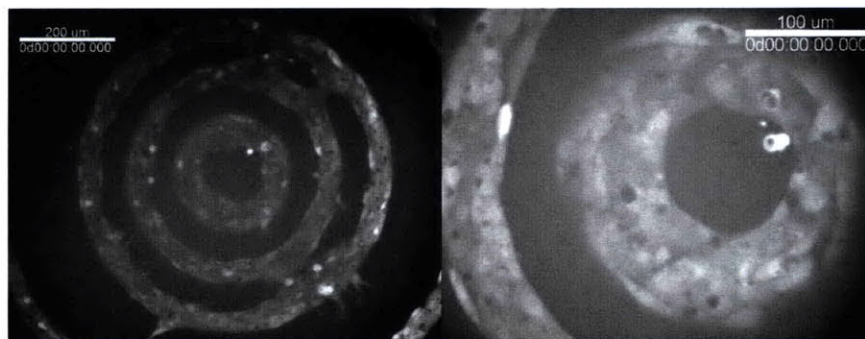


Figure 4-5: **HIGH DENSITY CELL POPULATION.** High Density of Cells, identically treated as 4-3



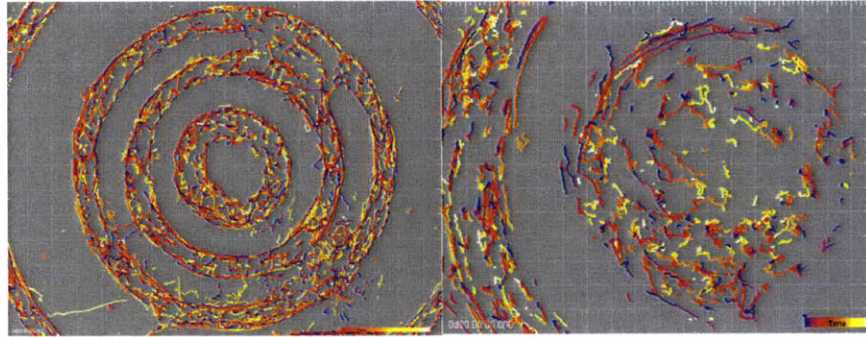


Figure 4-6: HIGH DENSITY CELL TRAJECTORIES. Trajectories of cell movement on stamped pattern for the high density system. More highly dense systems also show preferences for the boundaries, although the effect is significantly less pronounced than the lower density.

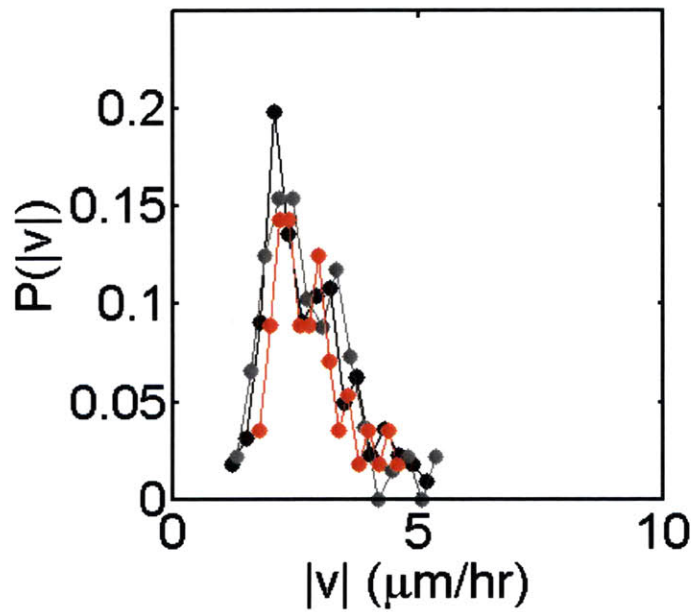


Figure 4-7: PROBABILITY DENSITY FUNCTION FOR CELL VELOCITIES (LOW). Probability Density Function for the velocity of cell trajectories in low density populations with diameters 50  $\mu\text{m}$  (red), 150  $\mu\text{m}$  (gray), and 250  $\mu\text{m}$ (black). Each overlaps, and contains the same non-gaussian character, and slight fast subpopulation.

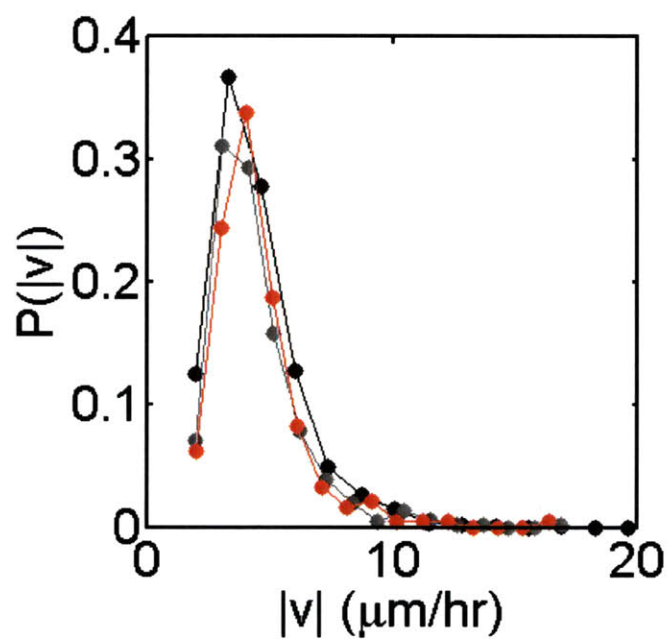


Figure 4-8: PROBABILITY DENSITY FUNCTION FOR CELL VELOCITIES (HIGH). Probability Density Function for the velocity of cell trajectories in highly dense populations with diameters 50  $\mu\text{m}$  (red), 150  $\mu\text{m}$  (gray), and 250  $\mu\text{m}$  (black). Each overlaps, and contains the same non-gaussian character, and slight fast subpopulation.

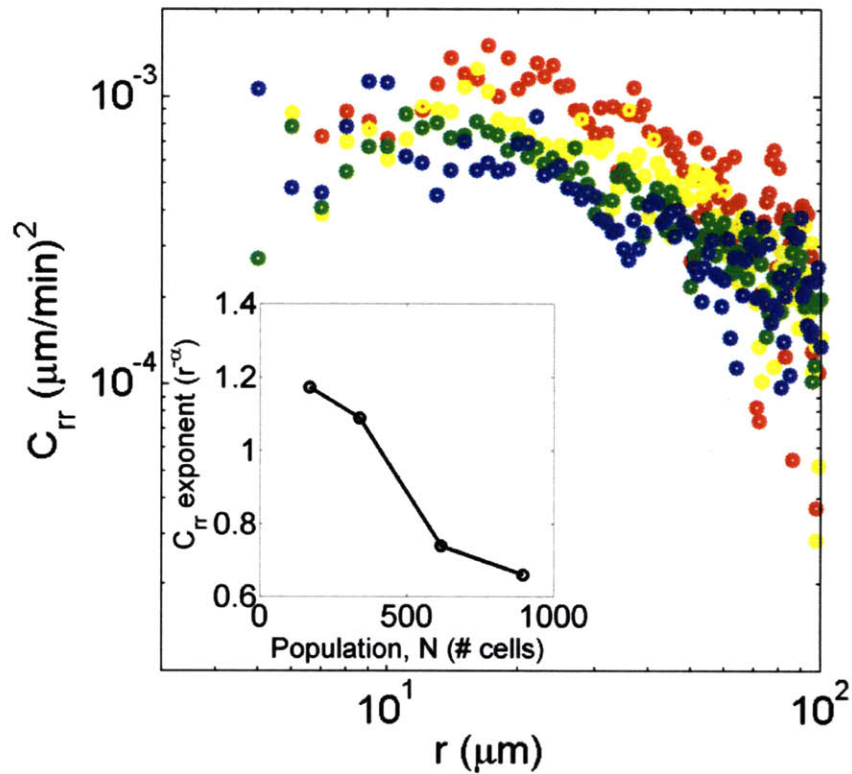


Figure 4-9: MUTUAL CORRELATION FUNCTION FOR SEPARATE POPULATIONS. Mutual Velocity Correlation Functions for the separate populations as defined by the spatial patterning. This function isn't really valid above the half-width of the patterns, which is  $50\mu\text{m}$ , but nevertheless, illustrates an important conclusion. There is no real difference in the level of correlated activity. (red:  $50\mu\text{m}$  inner radius, yellow:  $150\mu\text{m}$  inner radius, green:  $250\mu\text{m}$  inner radius, blue:  $350\mu\text{m}$  inner radius. The modulus of the PDMS is  $492.2\text{ Pa}$ , with  $G''=154.5\text{Pa}$ , and  $G'=470.2$

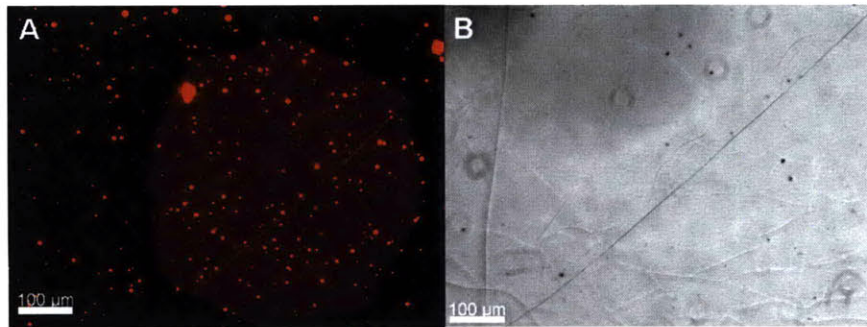


Figure 4-10: STIFFNESS ALTERATION BY OXIDATION?. Twelve minute plasma oxidation of a 1/10 PDMS surface, and subsequent non-specific stamping of fibronectin (A) 10x Fluorescence image of the fibronectin, (B) brightfield 5x image of cracks throughout the dish. Stamping on surfaces of different stiffness was not pursued, largely because we were unsure whether or not by oxidation of the PDMS surface, we were altering the stiffness as well as the chemical composition. Then we have both the effect of the covalent attachment as well as the stiffness to contend with when analyzing the movement of the cells.

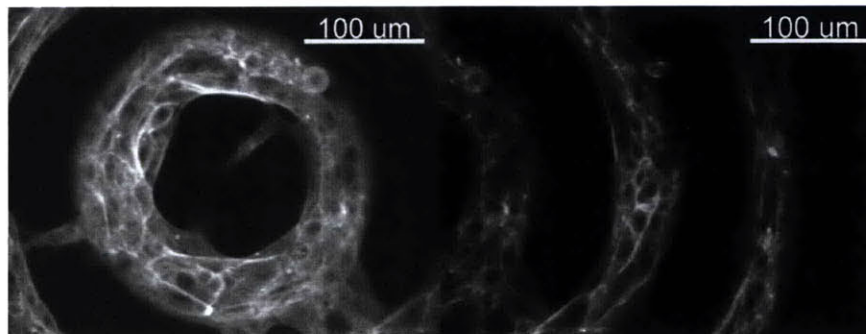


Figure 4-11: ACTIN CONTRACTILE BUNDLES IN PSEUDO PURSE-STRING. 1:200 rhodamine-phalloidin was used to stain the filamentous actin bundles in a pattern of mouse mammary epithelial cells. It shows that there is a large concentration of actin bundles arranged radially, and preferentially towards the center and the inner diameter of each ring. Thus, the formation of these bundles is not dependent upon the wound, as in the "purse-string" closure of a small wound, but is sufficiently explained by free space.



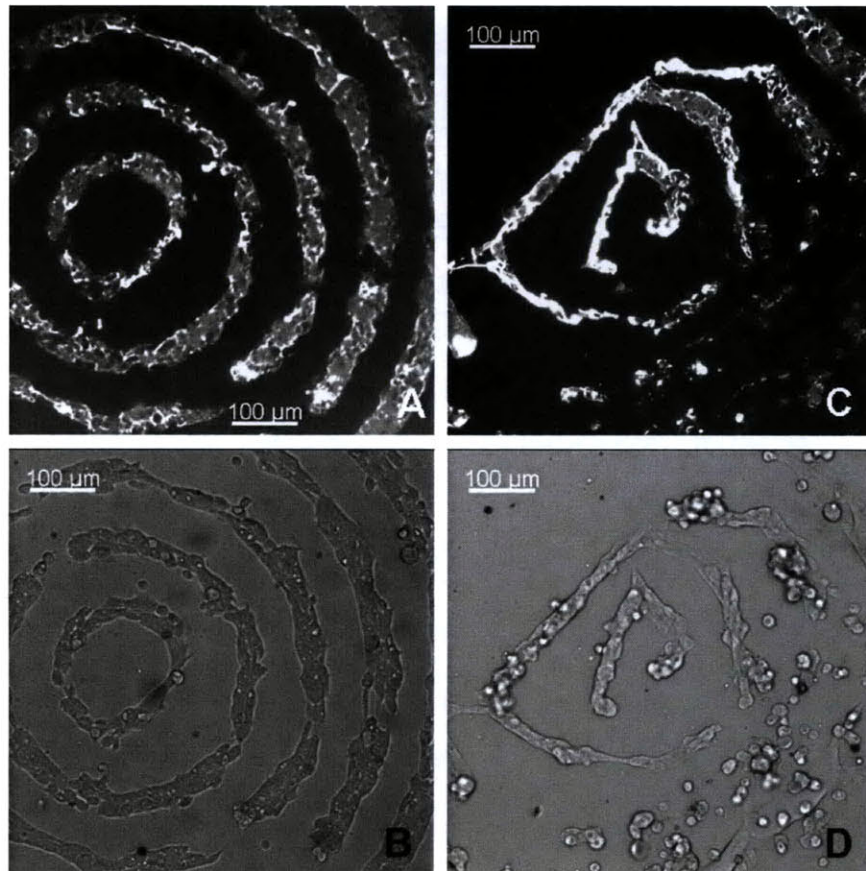


Figure 4-12: 10x image of fibronectin stamped onto two separate samples, PDMS surfaces of a crosslinker/prepolymer concentration 7/400. The surfaces were treated as described above, with FITC-Pig Skin Gelatin as contrast. Collagen is good as a contrast agent, but also adheres cells more quickly than fibronectin. This can be a valuable parameter, as even given the cell exclusion chemistry, the longer that cells sit on the surface, the more likely it is they can still bind the surface where you do not want them.



# Chapter 5

## Supplemental Studies To Sheet Motion

### 5.1 Computational Methods

#### 5.1.1 Dynamic Monte Carlo Simulations

Since the correlation function is pairwise, likewise, the potential is approximated to the sum of the energy that exists between any two cells. This effectively reduces a many-body problem to a two-body problem. That is, that any single cell will feel the effects of all of its neighbors, but we say that all neighbors essentially act independently as an approximation, and that their effects can be averaged. We expect that there are not higher-order contributions to this potential, that three or more cells contribute to a potential in a way that is significantly stronger than what can be expected purely by pairs. This type of approximation is generally considered in very low density media. In this case, when density is low, the probability of having more than two pairs come within close enough proximity to interact, we can clearly say that any interaction will be purely a two-body interaction. Nevertheless, at high densities, using a pairwise potential is still valid, because we are essentially just saying that by averaging all pairwise interactions we approach an accurate potential.

In the monte carlo simulations, we allow only two potentials to exist - either infinite in the case that two cells may occupy the same space (thereby making the probability of their occurrence zero), and zero, when the cells are not in contact.

$$U(r) = \{0, r > a\}, \{\infty, r < a\} \quad (5.1)$$

To simulate a more sophisticated potential, we would need much more detail about the energy that drives the system, as the system is athermal. The hard disk model works in athermal systems, because zero or infinite potentials make thermal energy irrelevant. However, to pursue a more detailed potential in an athermal system, we need to estimate the energy that drives cells to sample their surroundings. Others argue that the movement or arrangement of each cell involves breaking all of their adhesive connections, then we can use this as the effective energy fluctuation per cell. That is the measured force of breaking for example, cadherin-cadherin interactions, multiplied by the average number of these molecules there are per cell. Glazier et. al. ([37]) have calculated an athermal energy,  $\beta$  of  $2 * 10^{-8}$  J, or  $5.1 * 10^5$  kT by measuring the apparent diffusion of single cells in aggregate systems, and using Stoke's Einstein with measured tissue viscosity and mean cell diameter (all done for pigmented epithelial cells in aggregates of neuronal retinal cells).

While we only use the hard disk simulation as a control for our van Hove and mutual velocity correlations discribed in the subsequent subsections below, we also simulate simple Lennard-Jones potentials at different temperatures for comparison, and as internal controls for the simulations. From figure 5-7, we can see how the density correlations vary with different temperatures. At  $kT = 10$ , the 300 particle system is crystalline, and melts for increasing temperature, until it is a gas at  $kT = 1000$ . At this point, the Lennard-Jones system is identical to the hard disk system. The peaks at large separation distance (between two particles)  $r$ , disappear. The only correlation that remains is for the nearest-neighbor distance. This is relevant, as the density correlations for cells on soft substrates, show shocking similarity to



the hard disk, or high temperature systems, with the only lengthscale being the first nearest neighbor distance. This is surprising, as I would have expected that if the sheet is now increasingly reliant on cell-cell contact for its displacement, then effectively the potential between particles (cells) should be increased. The strength of the interparticle potential is modulated by the temperature. Therefore, to a system with a strong potential will resemble a low temperature system, like the one in Figure 5-7b, where there are significant correlations at large  $r$ . This however, only exists for how cells organize themselves on hard substrates. Somehow, when cells cannot deform the substrate to which they adhere, they still manage to organize themselves with respect to each other in a highly coordinated way. There is no reduced symmetry, as there are in crystalline systems. There is just long ranged, but perfectly symmetric van Hove correlations, similar to what one would find in a simple fluid.

### 5.1.2 Velocity Correlations and the Elastic Wave Equation

As part of the hypothesis that motility becomes a collective effort as a result of unbalanced cohesive contact, there should likewise be an associated parameter that relates how cells become increasingly mutually correlated. To this end, similar to the correlation the positions of pairs of cells, we correlate the motion of pairs of cells, this time not just by their separation, but also for all time. That is, that we are interested in finding out over what lengthscales and what timescales cells can influence each other's motion.

Each nucleus is placed in reference to its pair partner. After an elapsed time  $\tau$ , both nuclei (denoted as subscript 1 and 2) will have moved to new positions  $(\Delta x_1, \Delta x_2)$ . They will have moved in a fashion influenced by each other, either in towards/away from each other  $(\Delta x_{\perp,1}, \Delta x_{\perp,2})$ , or tangentially  $(\Delta x_{\parallel,1}, \Delta x_{\parallel,2})$ . I therefore correlate the movement in both directions 5.2, as well as cross correlating both directions. [3]

$$D_{\alpha\beta} = \langle \Delta x_{\alpha,1} \Delta x_{\beta,2} \rangle - \langle \Delta x_{\alpha,1} \rangle \langle \Delta x_{\beta,2} \rangle \sim 1/r^{\zeta_{\alpha\beta}} \quad (5.2)$$

The same is done for the parallel direction, as well as a cross correlation.

To remove any potential drift (important in the case of soft substrates, as the sheets slide), the correlation function is corrected by the mean displacements in each direction.

Also, considering the form that the correlation functions take, we may be able to make statements about the behavior of the sheet itself. For example, one of the main findings, is that the mutual correlation function decays as  $1/r$  in the limit of very elastic substrates. If we consider an elastic wave in an isotropic medium, then the deformation of the medium can be expressed as 5.3, which exhibits the same long-range behavior. In this equation of motion, the parameters that confer the material properties are  $\lambda$  and  $\mu$ , the Lamé (elastic) constants [59].

$$\mu \nabla^2 u + \lambda \nabla (\nabla \cdot u) \tag{5.3}$$

The solution given a point source in radial coordinates and at long lengthscales (where  $\frac{1}{r^3}$  has decayed to zero) is proportional to  $\sim \frac{a}{r}$ . Thus, for our two-point correlation, which measures deformation of complex media, a region in space where there is a  $\frac{1}{r}$  decay would indicate that the media can be considered a homogeneous continuum. The importance of this, is that the details of the mechanics with regard to components below this lengthscale are irrelevant to mechanics beyond this lengthscale. The details are averaged-out. Further, what does this imply about how cells interact? Are there analogies that can be drawn between how fluids or elastic solids decay their stress that could shed light on how cohered cells dissipate theirs?

### 5.1.3 Dynamic Structure Factor and Collective Modes

The hypothesis is that long-lengthscale correlation is established by transition from the 'reach, grab, and contract' model to an in-plane fluctuation of large, multicellu-

lar domains facilitated by the destabilization of adhesions that occurs on less elastic substrates. To add context to the characteristic lengthscales that we see within the cell sheet, we can compare those to the lengthscales, as calculated from the monte carlo hard disk and lennard-jones simulations(5-7). This hypothesis would be supported if with the increased elasticity of the substrate, that the lengthscales within the cell sheet approach what we get with monte carlo simulations of hard disk (non-interacting) systems of the same dimension.

With the assumption that cells in a monolayer will adjust their positions relative to each other in a fashion that minimizes their mutual adhesive energy, both with their substrate and each other, we can gain an understanding of the level of interaction between cells. For this, we use fluorescently labelled nuclei to track cells in two dimensions, and we utilize the radial distribution function (RDF,  $g(r)$ ), a function that measures the correlation in position between pairs of particles (cells in this case) bound by an interaction potential. More specifically, the  $g(r)$  describes the probability of finding particles suspended in a medium at a certain distance,  $r$ , away from a reference particle [5.4]. It is normalized to the overall density, such that at the density approaches the overall density at large separations ( $g(r) \rightarrow 1$ ).

$$g(r) = \frac{\langle \sum_{i=1}^{N-1} \delta(R - r_i) \rangle}{\rho} \quad (5.4)$$

The first maximum in the RDF, or the first "coordination shell", occurs at the closest distance that two cells can approach each other. This is generally the physical separation induced by purely excluded volume, the fact that two cells cannot occupy the same space at the same time. The subsequent maxima in the correlation function are due to geometric constraints - how far away other cells may be and still be correlated to the reference cell. The distance over which this is relevant is the correlation length, the parameter that characterizes the lengthscale that cells can influence each other physically in the epithelium.

The structure of the radial correlation function reveal the mechanisms that underly organization of the epithelium. In the simplest possible case, cells organize themselves in the epithelium purely avoiding occupying each others space, what (again) is known as a hard disk model. This is a repulsive interaction, and biases the probability of two cells being in close proximity. Accordingly, there will be a specific decay in the correlation, depending on the size and density of the disks (The correlation length for hard-spheres scales with the radius,  $a$ , but inversely with the volume fraction,  $\phi$ , as  $\zeta \sim \frac{a}{\phi}$  ([60])).

The van Hove correlation function is the radial distribution function taken for every elapsed time,  $\tau$ .  $\rho(r, t)$  represents the number of cells surrounding another cell given that that first cell is at the origin, at  $r=0$ . So, for every elapsed time  $\tau$ , we are taking the separation distance between all other cells,  $r$ , and that cell at  $\tau = 0, 1, 2, 3$ , etc....

$$G(r, t) = \frac{1}{\rho} \langle \rho(0, 0) \rho(r, t) \rangle \quad (5.5)$$

$$G(r, t) = \frac{1}{N} \langle \sum_{i=1}^N \sum_{j=1}^N \delta(r + r_j(0) - r_i(t)) \rangle \quad (5.6)$$

$$G(r, t) = \frac{1}{N} \langle \sum_{i=1}^N \sum_{j=1}^N \delta(r + r_j(0) - r_i(t)) \rangle \quad (5.7)$$

The dynamic structure factor is the fourier transform of the van Hove correlation function, in polar coordinates:

$$S(q, \omega) = \frac{1}{2\pi} \int_{-\infty}^{\infty} dt e^{-i\omega t} \int d^2\vec{r} e^{i\vec{q}\cdot\vec{r}} G(r, t) \quad (5.8)$$

$$S(q, \omega) = \frac{1}{2\pi} \int_{-\infty}^{\infty} dt e^{-i\omega t} \int_0^R \int_0^{2\pi} r dr d\theta e^{iqr \cos \theta} G(r, t) \quad (5.9)$$

We can integrate over all theta, as we are interested in all of the cells that lie in a circular shell around a reference cell.

$$S(q, \omega) = \frac{1}{2\pi} \int_{-\infty}^{\infty} dt e^{-i\omega t} \int_0^R r dr G(r, t) \int_0^{2\pi} d\theta e^{iqr \cos \theta} \quad (5.10)$$

$$S(q, \omega) = \frac{1}{2\pi} \int_{-\infty}^{\infty} dt e^{-i\omega t} \int_0^R r dr G(r, t) (2\pi I_0(iqr)) \quad (5.11)$$

Here,  $I_0$  is a modified Bessel function of the first kind. The modified function, while still used to represent wave-like phenomena, are not oscillatory, but grow exponentially. This function converges to  $qr = 0$ .

$$S(q, \omega) = \int_{-\infty}^{\infty} dt e^{-i\omega t} \int_0^R r I_0(iqr) G(r, t) dr \quad (5.12)$$

$$S(q, \omega) = \int_{-\infty}^{\infty} dt \cos(\omega t) \int_0^R r I_0(iqr) G(r, t) dr \quad (5.13)$$

We can use Euler's formula, for the time integral to reduce it to a cosine, since we know that the spatial function is going to be even.

$$S(q, \omega) = 2 \int_0^{\infty} dt \cos(\omega t) \int_0^R r I_0(iqr) G(r, t) dr \quad (5.14)$$

The static structure factor is just the frequency sum of the dynamic structure function:

$$S(q) = \int_{-\infty}^{\infty} d\omega S(q, \omega) \quad (5.15)$$

The first peak of the static structure factor,  $S(k)$ , is the lengthscale over which the correlation is the strongest, and is called the first diffraction maximum. From the Hard Disk case, we see that that correlation is highest at  $\frac{2\pi}{k_0} d \approx 134 \mu m$ .

The dynamic structure factor for a simple fluid consists of three peaks: the peak centered around  $\omega = 0$  is the Rayleigh peak, which represents thermal diffusion, and in our case random, unbiased motility. The two peaks on either side are the Brillouin peaks, which represent the propagation of phonons, and are spaced at  $\omega = \pm cq$ . These are the propagating modes.

From Figure ??, we see that on soft substrates, we have a loss in the positional correlation as we move towards larger  $r$ , than we have on the hard substrates. However, there is a second lengthscale that emerges in the dynamic structure factor, that is hundreds of microns. This also emerges at longer timescales.

#### 5.1.4 Dynamic Susceptibility

The auto or mutual velocity correlation, or density functions depend on equilibrium movement. There can be no biased movement in any direction. As the measurement is in radial coordinates, any asymmetry would yield inconsistencies in the spatial component. However, we wanted to be able to extract a timescale associated with movement for both the denudation studies, as well as the equilibrium substrate mechanics studies, and compare them. For this purpose, we designed an order parameter that would be used to determine the mean time it took to exchange cellular neighbors. This metric is called "Dynamic Susceptibility", and is often used in granular physics [61].

The Dynamic Susceptibility keeps track of each cell, and each of its nearest neighbors, for all time. As the cell moves around, it may break adhesions with its neighbors, move, and reform adhesions with a separate party. This metric can yield an ensemble-averaged timescale associated with this movement. It is therefore useful for distinguishing between uniform movement (all cells moving in the same direction), versus scattering (where cells are all moving in different directions). As these separate modes of movement may have the same velocity, we figured this would be an additional helpful metric for characterizing cell movement.

For each cell trajectory, we iterate through real time,  $t$ , and identify each of its nearest neighbors. From the E-cadherin staining images in Chapter 2, we determined that at high density, on average a cell had six immediate neighbors, with whom it

shared a boundary. Therefore, we were interested in the amount of time it took for a cell to exchange these boundaries, and acquire new ones, with an entirely distinct set of neighbors. While the mean number of neighbors was six, it averaged between five and seven consistently. Therefore, we chose to calculate the amount of time that it took to exchange five neighbors, such that every cell could be counted. This was also more practical, as the amount of time required to exchange all of its six neighbors turned out to be too high for obtaining a significant sample size, over which we were to take an ensemble average. Further, a cell must move a very significant distance such that its initially furthest neighbor is not potentially its closest at the end of the run. Thus, for each trajectory, we define an order parameter,  $\omega$ , which is set to zero if the cell retains its original neighbors after an elapsed time,  $\tau$ , and one if it has exchanged all five neighbors.

$$\omega = 1, S_0 \cup S_\tau \neq 0 \quad (5.16)$$

$$\omega = 0, S_0 \cup S_\tau = 0 \quad (5.17)$$

There is no fractional value. Either the entire set is the same, or it is not. Only when the entire subset is different, will the order parameter be set to zero. This order parameter is then defined as a function of  $\tau$ , the elapsed time before different time points for the single cell trajectory.

$$m(\tau) = \frac{1}{N_\tau} \sum_{i=1}^{N_\tau} \omega_i \quad (5.18)$$

where  $i$  is an index over values  $\omega$ , that existed for that particular  $\tau$ . Therefore, averaging should be very good for short time, and poor for long times. We now have the mean order parameter,  $m$ , which describes for time-evolution of exchanging neighbors. Now, we want an ensemble average,

$$M(\tau) = \frac{1}{N} \sum_{i=1}^N m_i(\tau) \quad (5.19)$$

where  $N$  is the total number of cells. This now yields a similar looking curve to each individual  $m$ , but is now an average over the entire population. Therefore, this would be invalid if there were different populations behaving differently. We figure that this was still appropriate for wound and "model" wound models, because although there is increased motility in the leading edge, as opposed to the rear, unless there is some critical difference with *how* the cells exchange neighbors, then it is still valid. In other words, if some cells scattered, and some didn't, this wouldn't be a very good average. Further, the bulk of cells in a wound healing model all behave the same. We are really averaging out the effect of the leading edge cells, because they are in vast minority (and don't have the same number of neighbors anyways). Thus, the last step to extract the timescale, is to calculate the variance of this measurement.

$$\chi(\tau) = (\langle M(\tau)^2 \rangle - (\langle M(\tau) \rangle)^2) \quad (5.20)$$

This is useful, as the location of the peak ( $\tau^{**}$ ) tells us the timescale involved with exchanging nearest neighbors, and the magnitude gives the variance, or how different the temporal behavior is among cells in the same sheet. Therefore, if the cells were all moving uniformly in one direction, the peak would be very low, while if they were scattering at different directions with different timescales, the magnitude of this peak would be very high.

Nevertheless, we decided to abandon this metric, as it is not good for comparing across different densities. To do so would yield the wrong results. For example, at low densities, cells tend to move quickly and diffusively. This should give a short timescale, but does not. That is because at low density, the nearest neighbors are actually quite far away, and thus to move to the extent that the five cells that were initially closest, are no longer in the set of nearest neighbors requires quite a bit of movement. The timescales associated with that movement tend to be longer than we even image for. Further, at lower densities, there are not strong boundaries, as indicated in the cadherin staining images, and therefore even the classification of nearest



neighbors is somewhat arbitrary.

The substrate mechanics studies were largely done at high densities, and therefore we attempted to employ the dynamic susceptibility to identify important timescales ( $\tau^*$ ) for movement on different substrates. Not only is this method suitable for this study, because the monolayers are highly dense, but contrast was given to the nucleus for imaging, and thus there was immaculate tracking of the particles. This is critical, as the timescale relies on accurately finding the nearest neighbors for every cell at every point in time. Nevertheless, the dynamic susceptibility failed to yield information that we didn't already know. When we plotted the timescales of movement versus the shear modulus of the substrate (at relatively constant density), we get essentially the same transition that we already classified by the lengthscale of the two-point correlation function from Chapter 2.

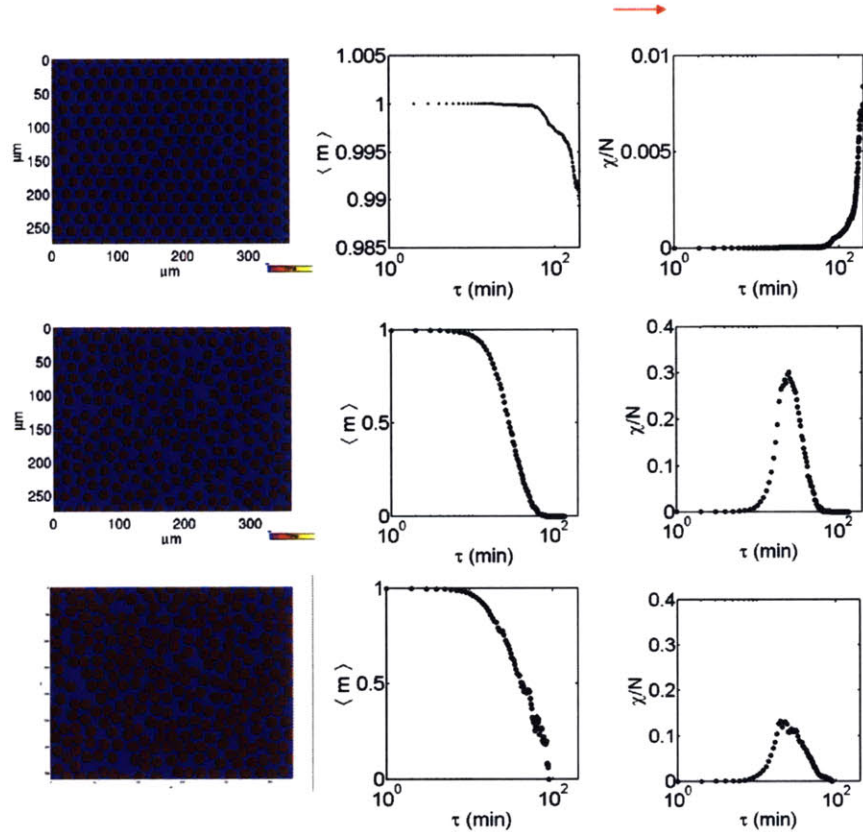


Figure 5-1: DYNAMIC SUSCEPTIBILITY. Using a technique quite common to granular physics, we seek to identify timescales involved with the exchange of neighbors. As cell monolayers that move uniformly versus those that scatter may have the same magnitude of their velocities, we wanted an order parameter that would be able to distinguish between the two. Here, we show the results of three simulations. In the top row, there is a crystalline system with low displacement, and nearly no neighbor exchange. Therefore the order parameter barely dips, and there is no identifiable timescale by the susceptibility parameter,  $\chi$ . As the temperature of the system is increased (middle row), there is now a finite timescale, as thermal energy is sufficient to drive the scattering of each of the particles. Taking the same density, but biasing the movement (bottom row), we get the the magnitude of  $\chi$  decreasing, reflecting the increased uniformity, as each cell has a preferred motion. As this system could not be easily compared across densities, we opted for just the mean cosine as a superior method.

### 5.1.5 Modeling the Sheet as a 2D XY Ferromagnetic Material

The continuous XY model was first used to describe the second order phase transition in magnetic materials with a magnetization vector that lies in a two-dimensional plane. It is symmetric with rotation in the plane (around a z-axis). At zero temperature, all of the spins are aligned, but as the temperature rises, vortices appear to destroy the ferromagnetic order (the ferromagnetic phase, corresponds to perfect magnetization, where there are no vortices). In this sense, symmetry is broken as temperature is lowered, as at high temperatures, the system is possessed by vortices which destroy any mutual orientation.

We can begin by describing the interaction between elements on a two-dimensional lattice for homogeneous systems (S(02) symmetry):

$$H = -J \sum_{\langle i,j \rangle} \vec{S}_i \vec{S}_j = -J \sum_{\langle i,j \rangle} \cos(\phi_i - \phi_j) \quad (5.21)$$

where J is the strength of interaction between nearest neighbors, and  $\phi_i$  and  $\phi_j$  represent the angles of each spin about an arbitrary axis (x-axis). Thus, there is an energetic cost to being aligned - the cosine ensures that the lowest energy state is the disordered state.

Since the order parameter (akin to the magnetization) is now a vector (as opposed to a scalar in the Ising Magnet), we will say it has two components, breaking it into:

$$\vec{m} = (\psi_x, \psi_y) = \psi_x \hat{x} + \psi_y \hat{y} \quad (5.22)$$

Depending on the strength of the nearest neighbor parameter, J (which should depend on temperature), we can have three different phases in a two-dimension XY magnet:

- 1) For weak nearest neighbor interaction (high temperatures), the two-dimensional

system is in the disordered phase, with a zero order parameter. The correlation function in this phase should decay exponentially with separation,  $|r - r'|$ .

2) At the critical point, between the ordered and disordered phase, the correlation should decay with a power law, such as:

$$C_{rr'} \sim |r - r'|^{-2x} \quad (5.23)$$

where  $x$  is a universal critical index.

3) For very strong nearest neighbor interaction (low temperatures), the hamiltonian will favor the alignment of spins to some degree, and the two-dimensional XY model develops local fluctuations in the order parameter, called spin waves. The average order parameter over all space however, for all finite values of  $J$ , is zero, and thus there is no completely ordered phase (in two dimensions). The spin waves create a correlation function that decays algebraically, as:

$$C_{rr'} \sim |r - r'|^{-2z} \quad (5.24)$$

Where  $z$  is a universal coefficient.

There movement between these phases depends on the magnitude of the coupling coefficient,  $J$ . Thus, at low  $J$ , we are in a disordered phase, at high  $J$ , we are ordered, with spin wave fluctuation, and at some intermediate, critical  $J$ , we can have a critically ordered phase.

If we can consider the order parameter to be spatially constant, then we can write down the Landau Free Energy, a series approximation in the order parameter.

In the Ising magnet, we can invert the spins, and the energy remains the same, and so the Landau Free Energy can be written as a sum over even-order terms. Further,

Ising magnets should be reversible in time, disallowing any odd terms. Our scenario is slightly different for a number of reasons. First, it is continuous. There are not two states, spin up or down, but the entire 360 degree range in a two-dimensional plane. This is more similar to the xy-model. Further, although the system should ostensibly be dissipating energy, we can say that it is effectively in a heat bath. The cells are in cell culture medium, which continuously provides them with nutrients, allowing them to move continuously, with no noticeable decrease in speed. This is in addition to the fact that they are cancer cells, which means they never stop growing or moving. Considering also, that there is no preferred direction (until symmetry is broken), we can use purely the even terms in the Landau Free Energy.

We are taking the velocity auto and two-point correlation. If we acknowledge that this is just displacement/time, then we can treat each of the following terms as strain normalized by some time.

We can write down the Landau Free Energy of the system:

$$f(T^*, \langle \vec{v} \rangle) = \alpha_0 + \alpha_1 \langle \vec{v} \rangle^2 + \alpha_2 \langle \vec{v} \rangle^4 \quad (5.25)$$

We also want to introduce a penalty for deviations from the average velocity,

$$f'(T^*, \langle \vec{v} \rangle) = \int dA \left( \frac{1}{2} \gamma_1 [\nabla \langle \vec{v} \rangle]^2 \right) \quad (5.26)$$

$$F(T^*, \langle \vec{v} \rangle) = f + f' = \alpha_0 + \alpha_2 \langle \vec{v} \rangle^2 + \alpha_4 \langle \vec{v} \rangle^4 + \int dA (\gamma_1 (\vec{\nabla} \langle \vec{v} \rangle)^2) \quad (5.27)$$

Each of these terms would have the following physical interpretations:

- (1)  $\vec{v}^2$ :
- (2)  $\vec{v}^4$ :

(3)  $|\nabla \cdot \vec{v}|^2 \sim \frac{1}{|\vec{r}|^2}[\delta u]^2$ : Spring-like energy penalty for velocity field (similar to strain). Symmetry in that compression has equivalent energy to tension. This is similar to an interfacial tension term.

(6)  $|\nabla^2 \cdot \vec{v}|^2$ : Spring-like energy penalty for differences between velocity fields. (E.g. a pair of cells may move away from each other, the adjacent pair may move towards each other, and since all four are mutually attached it creates a strained 'curvature' in their vicinity.)

In the analysis, we take two correlation functions, in the parallel and perpendicular direction are not equivalent. So again, we take the two separate components:

$$C_{ij}(\vec{x}, \vec{x}') = \langle \vec{v}_i(\vec{x}, \vec{x}') \vec{v}_j(\vec{x}, \vec{x}') \rangle - \langle \vec{v}_i(\vec{x}, \vec{x}') \rangle \langle \vec{v}_j(\vec{x}, \vec{x}') \rangle \quad (5.28)$$

Taking the two different directions,

$$C_{ij} = C_{\parallel}(\vec{x}\vec{x}')e_i e_j + C_{\perp}(\vec{x}\vec{x}')(\delta_{ij} - e_i e_j) \quad (5.29)$$

We can then try and match up the correlation functions that we compute with the analytic form, and fit.

$$\chi^{-1} = \frac{\delta^2 F}{B(\vec{k})B(\vec{k}')} \quad (5.30)$$

First, we can gain some insight into the system, but looking at the form of the Landau Free Energy. We can try and extract some lengthscales associated with the formation of those locally ordered domains by looking at the stability, as determined by the quadratic coefficients in L. If we convert the Landau Free energy in real space to fourier space, we get:

$$L = \int dV (\alpha_2 \langle \tilde{v}(\vec{k}) \rangle^2 + \alpha_4 \langle \tilde{v}(\vec{k}) \rangle^4 - \gamma k^2 \langle \tilde{v}(\vec{k}) \rangle^2) \quad (5.31)$$

Taking the quadratic Coefficients,

$$\langle \tilde{v}(\vec{k}) \rangle^2 (\alpha_2 - \gamma k^2) \rightarrow k = \sqrt{\frac{\alpha_2}{\gamma}} \quad (5.32)$$

The quadratic coefficient is minimized when  $k \rightarrow 0$ , or the correlation length,  $\zeta \rightarrow \infty$ . In the vicinity of the critical point (when the sheets switches from random motility to directed motility) there instability occurs at  $k=0$ . This means that there is no domain formation, that you move from completely unordered to completely ordered.

You can get a finite lengthscale when the derivative has two terms. This would imply the existence of another energy term such as  $(\nabla^2 \tilde{v} \vec{k})^2$  to balance the tension term. This a curvature term. This would then become:

$$L = \int dV (\alpha_2 \langle \tilde{v}(\vec{k}) \rangle^2 + \alpha_4 \langle \tilde{v}(\vec{k}) \rangle^4 - \gamma k^2 \langle \tilde{v}(\vec{k}) \rangle^2 + \kappa k^4 \langle \tilde{v}(\vec{k}) \rangle^2) \quad (5.33)$$

$$\langle v_\theta(\vec{r}) \rangle = 0 \quad (5.34)$$

$$\langle v_\theta(\vec{r}) \rangle = \theta_0 \quad (5.35)$$

$$\langle \tilde{v}(\vec{k}) \rangle^2 (\alpha_2 - \gamma k^2 + \kappa k^4) \quad (5.36)$$

$$k = \left( \frac{1}{2\kappa^2} \right)^{\frac{1}{2}} (\kappa(\gamma + (\gamma^2 + 4\kappa\alpha_2)^{\frac{1}{2}}))^{\frac{1}{2}} \quad (5.37)$$

$$k = \left( \frac{1}{2\kappa^2} \right)^{\frac{1}{2}} (\kappa(\gamma + (\gamma^2 - 4\kappa\alpha_2)^{\frac{1}{2}}))^{\frac{1}{2}} \quad (5.38)$$

This quadratic coefficient is minimized when  $k \rightarrow \sqrt{\frac{\gamma}{2\kappa}}$  This means that there is a finite lengthscale associated with the instability of the sheet.

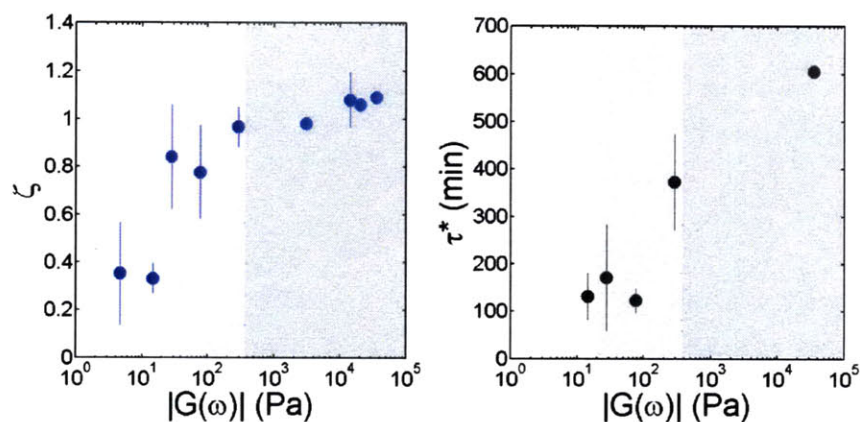


Figure 5-2: DYNAMIC SUSCEPTIBILITY PREDICTS A SECOND ORDER TRANSITION. The location of the peak in the  $\chi$  parameter,  $\tau^*$ , for the movement of monolayers on substrates of varying viscoelasticity predicts the same transition as does the divergent power law lengthscale calculated in Chapter 2, from the 2pt. velocity correlation function. The parameter  $\zeta$  is identical to  $\alpha'$  from Chapter 2, but only for very high densities.

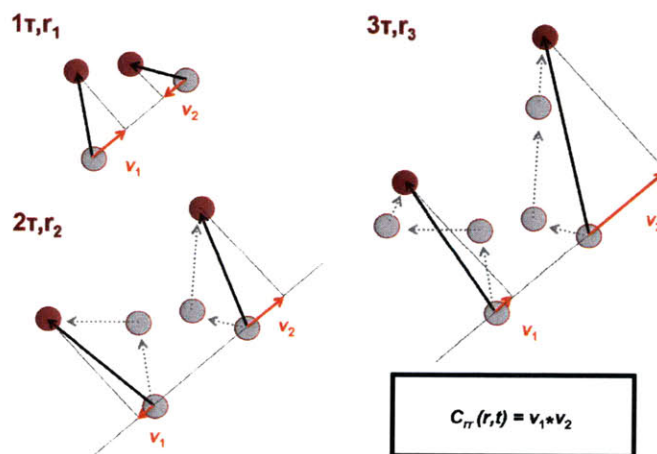


Figure 5-3: DIAGRAM OF MUTUAL 2PT CORRELATION FUNCTION. The correlation function whose power law exponent is used to outline the transition from uncorrelated to correlated behavior, is taken as the product of the velocities in the directions that connect them, in the radial, perpendicular direction.



## 5.2 Cell Mechanics

### 5.2.1 Cell Shear Modulus Calculation

As outlined in Chapter 7.11, by Fluctuation-Dissipation, we can relate the magnitude of the deflection of internalized microspheres to a shear modulus, and attempt to quantify the local mechanical properties of living cells. The movement of the beads is driven thermally, and its time dependence can be used to determine the rheology of the cell, in a fashion similar to the macroscopic rheology described in Chapter 3. Thus, the method for doing this is via Multiple Particle Tracking Microrheology (MPTM), where we use fluorescence imaging at high magnification with fast frame acquisition to generate the positions of these embedded microspheres over time, and a mathematical formalism to determine a characteristic modulus of the cell (Enthought Microrheology lab, <http://www.enthought.com/products/microrheology-lab.php>).

We use  $0.1\mu\text{m}$  and  $0.5\mu\text{m}$ , carboxylated (negatively charged), rhodamine coated latex microspheres, which we put in the medium to be internalized overnight by a subconfluent monolayer of mouse mammary epithelial cells (the chosen cell type for this thesis work), as well as Caco-2 colon epithelial cells, and then image their movement at up to 30 frames per second. The method of internalization is subject to serious debate, as some prefer this method of internalization, which is by endosomal uptake, increasing the probability of being actively transported once on the inside of the cell. The other predominant method is by microinjection, in which a needle that contains the beads, is used to puncture the cell, and force the beads inside. The clear caveat to this method is the damage that is induced by stabbing the cell. We rely on the former method, as while there is an increased likelihood of directed motion, this can be easily seen in the particle trajectories, and removed after the images have been taken.

The concentration is set such that there are on the order of tens of particles inside each cell. For averaging, generally more is greater, but as there is a high concentra-

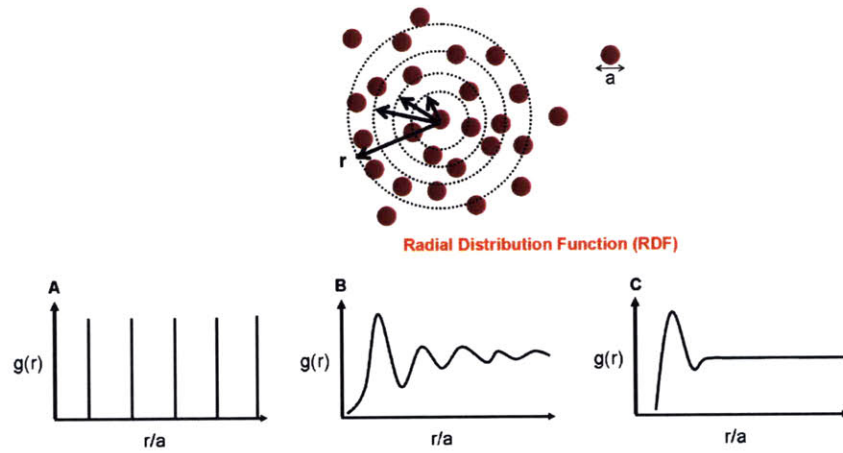


Figure 5-4: DIAGRAM OF THE RADIAL DISTRIBUTION FUNCTION. Each cell is at the origin of its own radial coordinate system. In successively larger intervals, at a distance,  $r$  away from the origin, the density of cells is counted. This function is solidly periodic for crystalline materials, oscillatory for weakly interacting or dense systems, and flat for non-interacting and very low density systems.

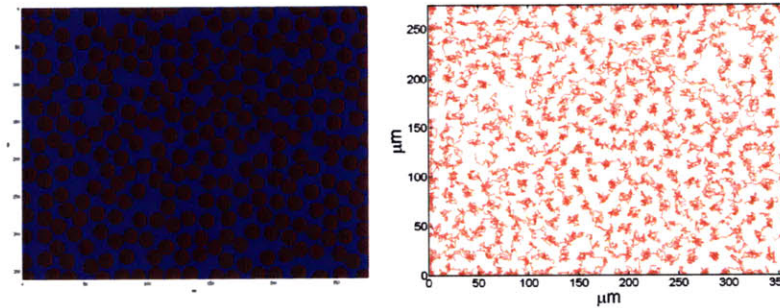


Figure 5-5: HARD DISK TRAJECTORIES. Trajectories of 300 hard disks. The potential is either 0 or infinity, and are walked around a lattice, and captured at 80 time points.

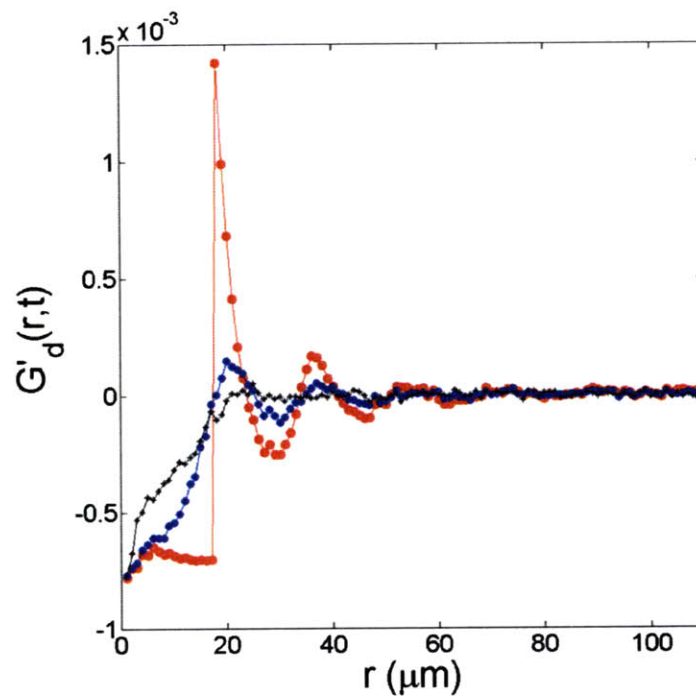


Figure 5-6: VAN HOVE CORRELATION OF HARD DISK SYSTEM MIMICKING CELL MOVEMENT. We use dynamic monte carlo simulations to reproduce cells in the same quantity and with the same dimensions as the cells we image at 25x. After collecting the trajectories of each *in silico* cell, we can calculate a control for the van Hove correlation function. At  $\tau = 0$ , there is significant order, out many cell diameters. This correlation is lost quickly over time, however.

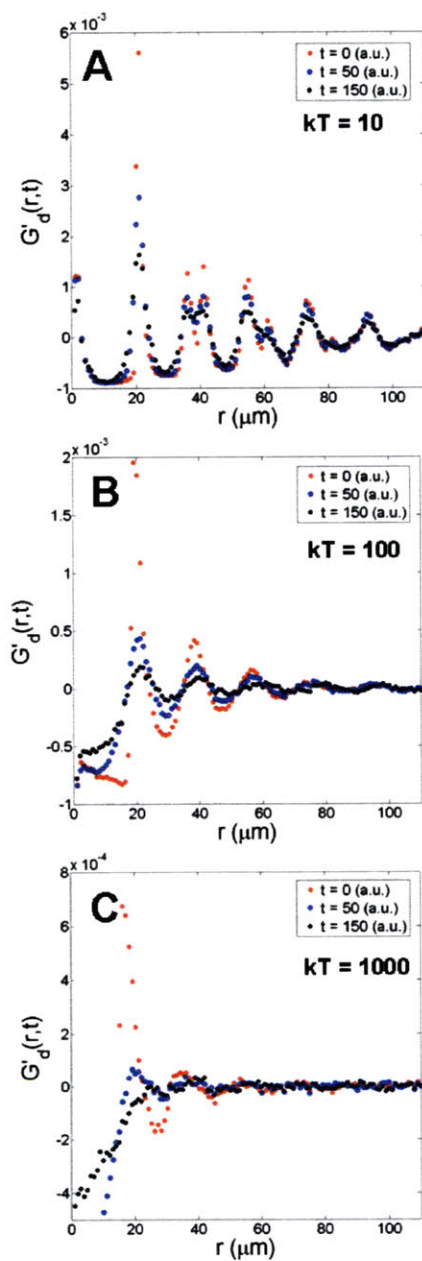


Figure 5-7: VAN HOVE CORRELATION OF LENNARD-JONES SYSTEMS MIMICKING CELL MOVEMENT. Lennard-Jones systems make use similar short-range exclusion as hard disk systems, but also have a very long ranged attraction. Using the canonical ensemble described in Chapter 8, we can lower the temperature to see the emergence of long ranged correlations in the van Hove correlation.

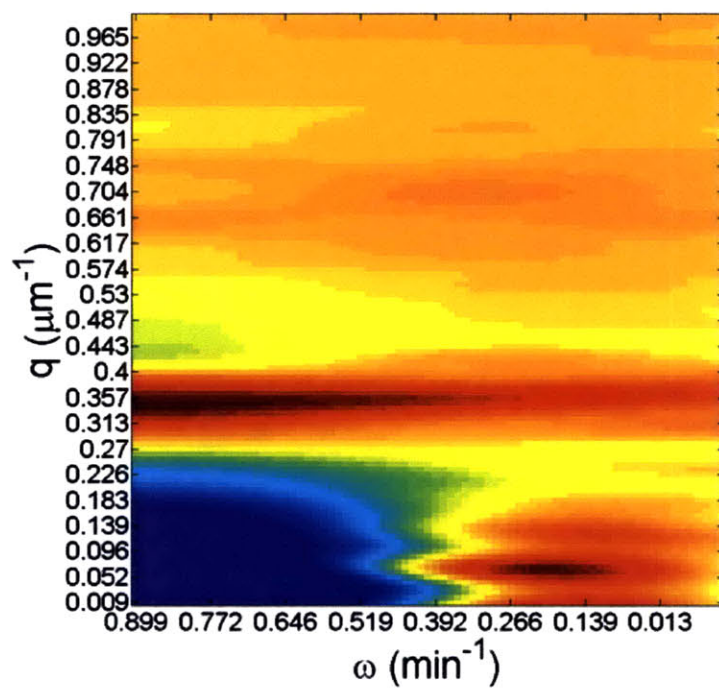


Figure 5-8: THE DYNAMIC STRUCTURE FACTOR FOR THE HARD DISK SYSTEM. The two-dimensional fourier transform in time and space peaked at  $2\pi/0.35 = 18 \mu\text{m}$ , the diameter of a single hard disk.

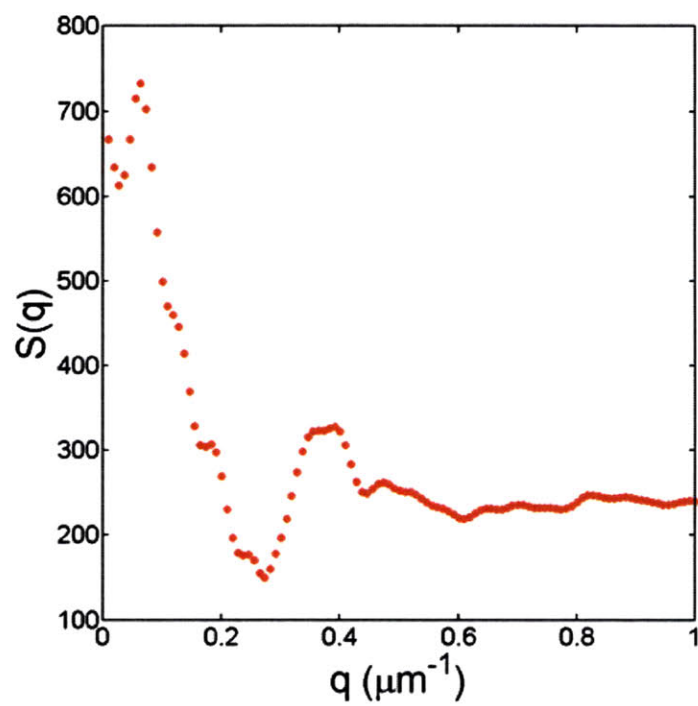


Figure 5-9: THE STATIC STRUCTURE FACTOR FOR A SHEET ON A VISCOELASTIC SUBSTRATE. The fourier transform of the radial ditribution function, showing a peak at the principal cell-cell spacing. This is the only relevant lengthscale.

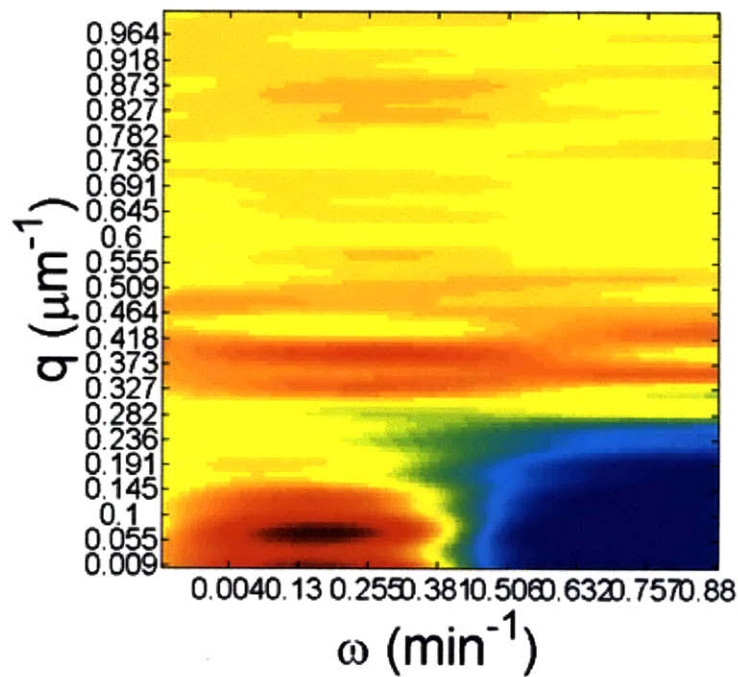


Figure 5-10: THE DYNAMIC STRUCTURE FACTOR FOR A SHEET ON A VISCOELASTIC SUBSTRATE. The same two-dimensional fourier transform was calculated on the van Hove correlation function calculated for the movement of cells within a plane, for every separation distance  $r$ , between cells, and every elapsed time,  $\tau$ , during the timecourse of the imaging. There are no significant collective modes, what would be seen as diagonals in the Dynamic Structure Factor. The only peaks remain for most time, and represent the characteristic lengthscales of the separation distances between cells.

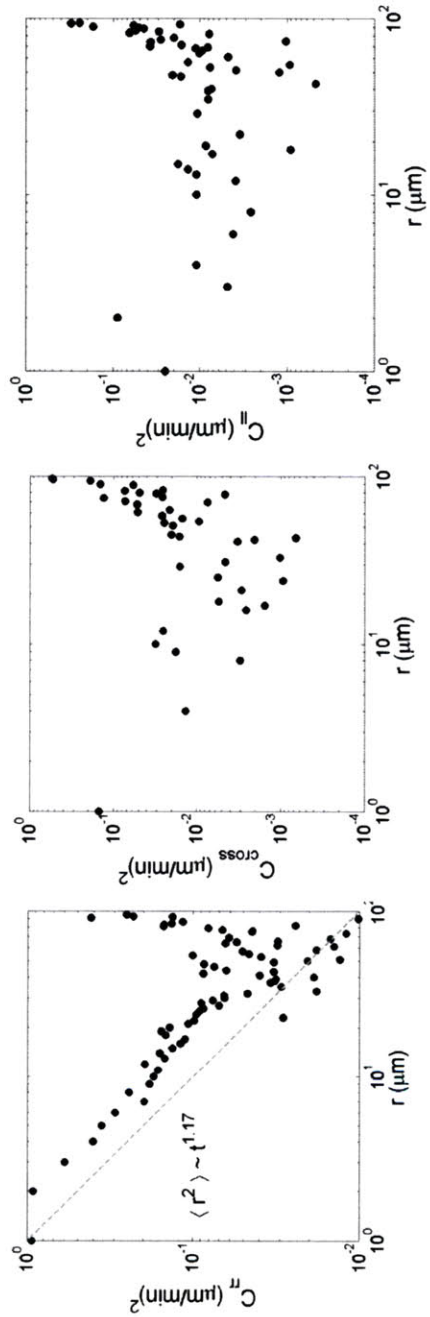


Figure 5-11: 2PT VELOCITY CONTROL. The  $C_{rr}$  has a  $1/r$  decay, and the magnitude is much greater along the mutual direction that connects two beads, than in the parallel direction, or crossing parallel and perpendicular.



tion of rhodamine on each bead, exposing continuously has proven damaging to the cell, even over just a few seconds.

After we acquire the positions of each embedded microsphere, for each point in time, we are interested in calculating the mean-squared displacement (MSD), the cumulative motion for each particle, ensemble averaged, as a function of an elapsed time (not real time). We use the square value for the displacement, as the brownian motion of thermal particles has a zero mean. Further, the (elapsed) time dependence of the MSD tells us directly how compliant or non-compliant the cytoskeleton of the cell is. This behavior tends to evolve as a power law for long times, and can thus be characterized by the scaling law exponent,  $\alpha$ . This parameter divides three separate regimes. If  $\alpha < 1$ , it is termed "subdiffusive", and means that the local environment that contains the bead has constrained it, and it is not free to sample space by what is predicted by Stokes-Einstein, as  $\alpha$  were equal to 1 (diffusive). When  $\alpha > 1$ , it is termed "super-diffusive", and this is where we generally assume there to be some active motion, if it did indeed occur. Oftentimes, within a single MSD plot, there are multiple regimes. At short times, a particle may be "caged", or confined by its local microenvironment, only to be released, either by rearrangement of the microenvironment (as it is an active network of biopolymers), or by sampling space, and running across the energetically unlikely way out.

From the frequency-dependent shear modulus in Figure 5-15, we see that for all frequencies shown, that the loss modulus is greater than the storage modulus ( $G'' > G'$ ), meaning that when subject to low rates of deformation the cell behaves like a viscoelastic fluid. The cell will dissipate energy that is applied to it, rather than store it. By taking a snapshot of the frequency-dependent shear modulus at a low frequency (1Hz - the standard, as many measurements are not made with fast cameras), we can name the elastic modulus. For mouse mammary epithelial cells, this value lies  $\sim 0.5$  Pa. This value compares with other values calculated by this same method. For example, in Tseng et al, [62], they find that for nearly all living

cells they measure, at  $1\text{rad/s}$ , they measure  $\sim 1\text{ Pa}$  ( $10\text{dyn/cm}^2$ ). Cos-7 are fibroblast cells, and by the same method, have been shown to be  $\sim 20\text{ Pa}$  ( $200\text{dyn/cm}^2$ ) [63].

It is quite surprising that we get values for the modulus of the cell that are this low. From the second order transition in correlated, mutual motion, we understand that substrate viscoelasticity plays a large role. However, substrate deformation begins in the realm of  $67\text{Pa}$ . This is three orders of magnitude greater than our calculated cell modulus. The implication then, would be that cells can contract and exert stresses that are much greater than their own resistance to shear can support. Therefore, we approach this value with caution. Our expectation was that the calculated modulus would be on the same order as what they can deform. This discrepancy is likely larger than we even expect, as we only measured the deflection of the substrate embedded beads at a magnification of  $25\times$ . This is the same magnification that we used to track cells, and so as we desired to capture many cells within a single frame, we wanted a relatively low magnification that still has a high NA, for high quality imaging (which for example, comes in handy when imaging the surface protein). We never did any studies at  $100\times$  and looking at much smaller, more minor deflections, that might be seen in more rigid substrates.

## 5.2.2 Controls

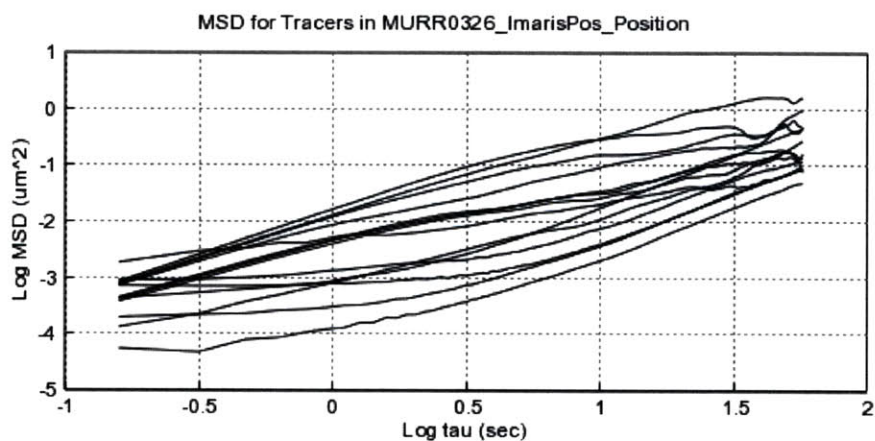


Figure 5-12: MEAN-SQUARED DISPLACEMENT FOR SINGLE ENDOCYTOSED PARTICLES.  $0.5 \mu\text{m}$  rhodamine coated, carboxylated, internalized microspheres were imaged over 60s in mouse mammary epithelial cells cultured on coverslips. Each line is a separate microsphere, located in a distinct local mechanical, microenvironment.

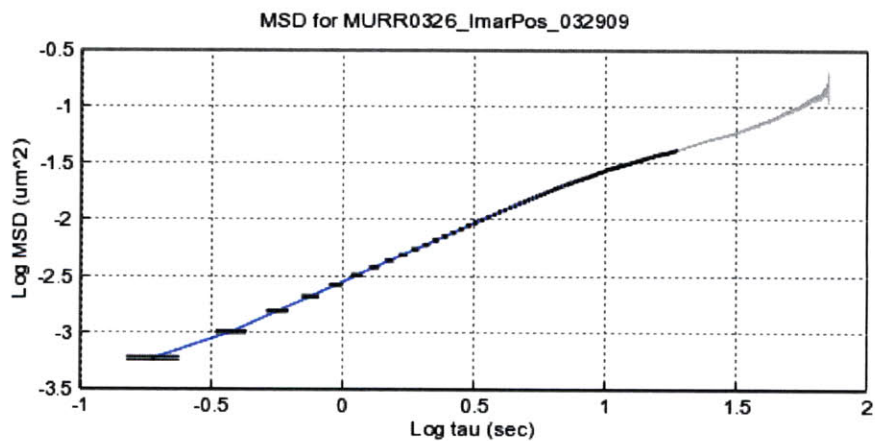


Figure 5-13: ENSEMBLE AVERAGED MSD FOR CELL ENDOCYTOSED PARTICLES.  $0.5 \mu\text{m}$  rhodamine coated, carboxylated, internalized microspheres were imaged over 60s in mouse mammary epithelial cells cultured on coverslips. The plot is the ensemble average of all of the different microspheres, so that we might fit it to a power law, and calculate the mean diffusivity of the particles.

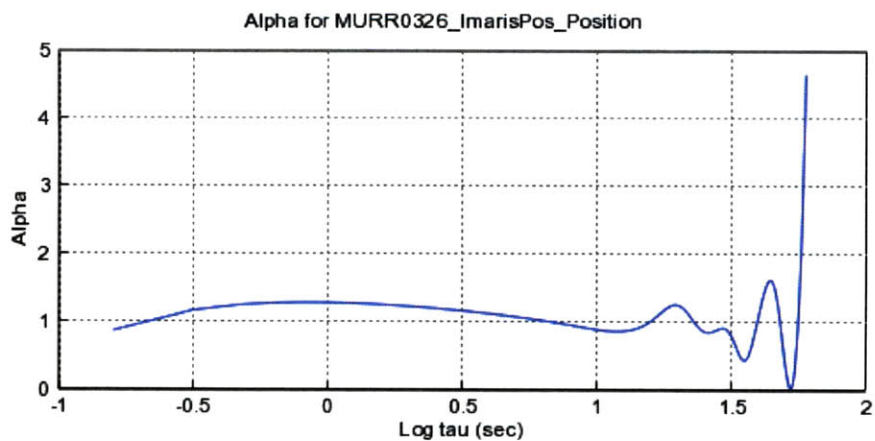


Figure 5-14: POWER LAW SCALING FACTOR FOR MSD. At short times, the embedded microspheres are often confined by the cellular cytoskeleton, and thus are "sub-diffusive" ( $\alpha < 1$ ), unable to sample space at the rate that is expected by diffusion. As more time elapses between frames however, the bead is able to break free, and diffuse freely ( $\alpha \sim 1$ )

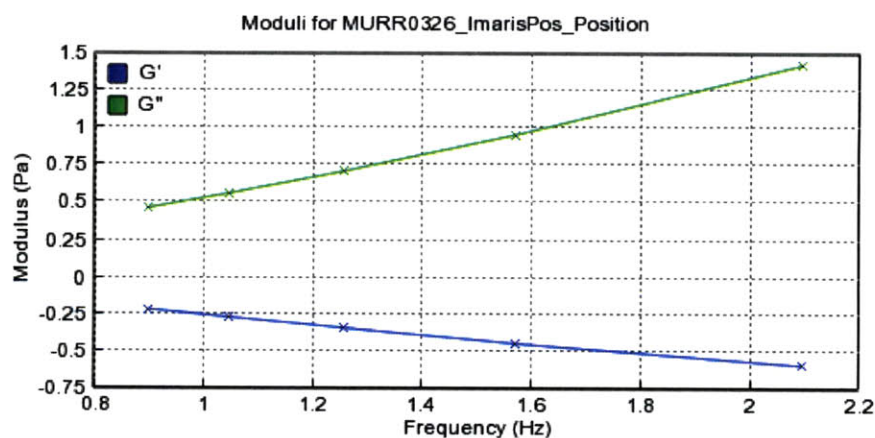


Figure 5-15: FREQUENCY-DEPENDENT SHEAR MODULUS FOR MOUSE MAMMARY EPITHELIAL CELLS. From the MSD, the particle size, and the temperature, we can calculate the frequency-dependent shear modulus.  $G'$  is the loss modulus, an indication of how the cell stores elastic energy that is applied.  $G''$  is the loss modulus, what indicates how the cell dissipates energy applied to it. Clearly from this figure, we can see that for nearly all timescales, the cell is more viscous than it is elastic.

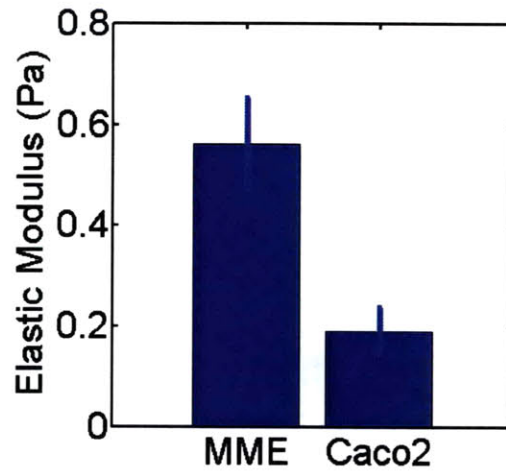


Figure 5-16: MEAN ELASTIC MODULUS FOR DIFFERENT EPITHELIAL CELLS. Mean Elastic Modulus, for both mouse mammary epithelial cells, as well as Caco-2 colon epithelial cells. The mean Elastic modulus for the mammary epithelial cells, what we use throughout the experiments in this thesis, is  $0.5631 \pm 0.0903$  Pa, or  $5.631 \text{ dyn/cm}^2$  ( $n=3$ ). The mean Elastic Modulus for the colon epithelial cells, which are more likely more similar to the intestinal epithelium, to which we draw many analogies, is  $0.1915 \pm 0.0464$  Pa, or  $1.915 \text{ dyn/cm}^2$  ( $n=3$ ). Both measurements are taken at 1 Hz.

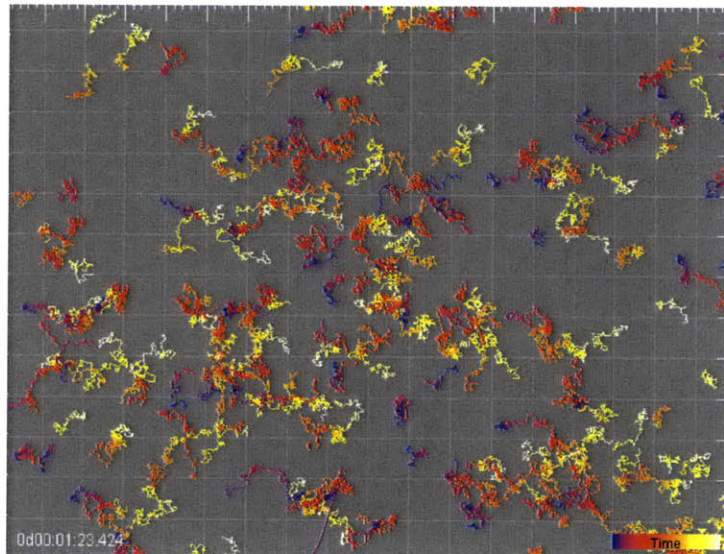


Figure 5-17: BEADS IN GLYCEROL.  $1 \mu\text{m}$  beads in a 50:50 mixture (by volume), imaged over 100 seconds. The trajectories are color-coded, with dark being old, and light colors being more recent.



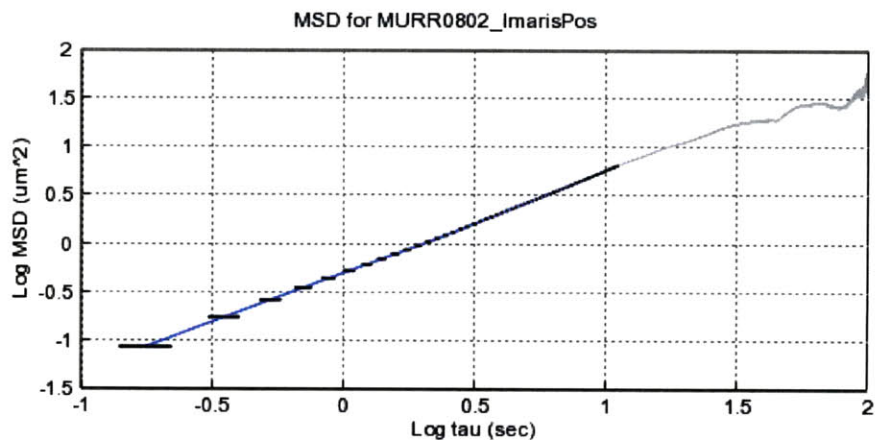


Figure 5-18: MEAN-SQUARED DISPLACEMENT FOR A 50:50 GLYCEROL/WATER MIXTURE. Perfectly linear scaling for the MSD, over nearly all timescales. The only limitation is the ability to track the beads for every frame, as the beads can diffuse out of the plane.

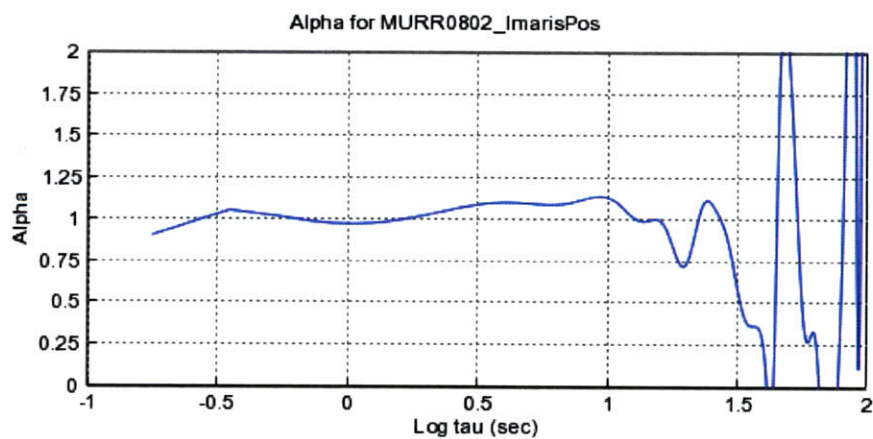


Figure 5-19: POWER LAW SCALING FACTOR FOR GLYCEROL MSD. The mean-squared displacement scales as  $\tau^{1.0}$  for nearly all timescales, confirming that all motion is strictly diffusive.

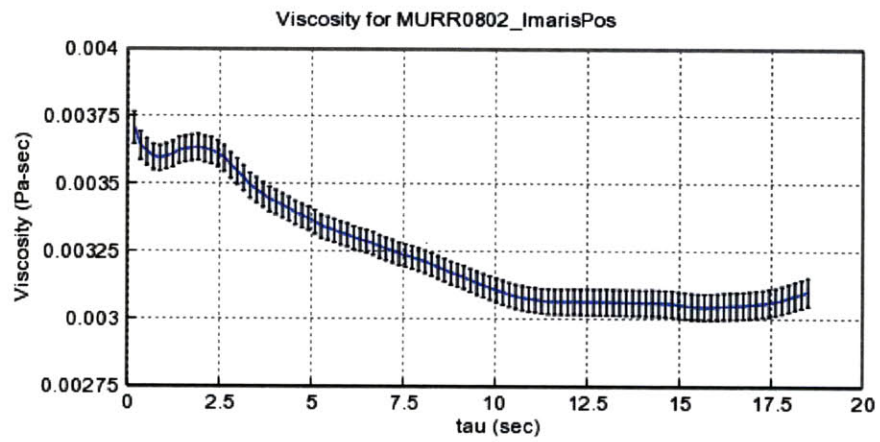


Figure 5-20: VISCOSITY OF A 50:50 GLYCEROL/WATER MIXTURE. The viscosity of the 50:50 Glycerol/Water mixture is  $\sim 3\text{mPa s}$ , as measured in *Properties of Ordinary Water-Substance N.E. Dorsey, p. 184., Hafner Publishing Co., New York (1940)*.



## Chapter 6

# Conclusions and Review of the Initial Hypotheses

We first began by addressing the outstanding issues in the field, as they pertain to the dynamics of sheet motion *in vitro*, namely, both wound and "model" wound healing assays. These systems are unable to relate the onset of coordinated sheet migration with an actual mechanism, as they are confounded by the previously unseparable free space and cell damage that occur as a result of a physical denudation. Further, they are misguided by the principal assumption that sheet motion must progress from traction at the leading edge and a physical "tug-of-war" within the sheet. Therefore, I 1) developed a superior method of denudation to separate these effects, and 2) further proposed a second model, based on the interaction of the collective sheet with a deformable substrate, characterized by the extent of its deformability and the reorganization of cell surface protein. This model relies less on traction to drive motion, but hinges critically on cell-cell contact, when destabilized with respect to the substrate. In this sense, I incorporated some of the hypotheses that exist in the biological community, regarding how *in vivo* systems move, most notably, that the cell substrate, as an analog to the basal lamina, plays a more explicit role in the conferral of correlated motion to the substrate by its viscosity. Further, this highly correlated state, is distinct both dynamically and phenotypically, as it is distinguished from other states by the geometric organization within the sheet, ability to influence each other's velocity

over long lengthscales, and as well as the cellular morphology.

## 6.1 The influence of free space in coordinated migration

We showed that denudation by enzymatic cleavage is sufficient to induce coordinated migration, and the recovery of free space. However, this recovery is significantly reduced in the submarginal region of the sheet, with most motility strictly occurring at the leading edge. Thus, even less rear motility is observed at the same density, as compared to wound healing assays. Thus, the generation of a physical wound is apparently not necessary, but is responsible for fast recovery, likely due to cell-cell signaling between cells. Nevertheless, the movement of both the border and the rear of the sheet are not statistically distinct ( $p_{border} = 0.678$ ,  $N_{border} = 14$ ,  $p_{bulk} = 0.5056$ ,  $N_{bulk} = 20$ ). The monolayer in the channel often scatters, even at relatively high densities, which recovers free space much faster.

Further, as we know that the loss of functional E-cadherin promotes a fast, invasive phenotype, with its blockage by exogenously added antibody, we show that cells speed and the recovery of free space is markedly increased ( $p < 0.001$  for both denudation models). Somewhat surprisingly, the blocking of E-cadherin not only promoted enhanced motility, but coordinated activity. By the ensemble averaged mean cosine, persistent cell behavior has a much smaller dispersion, and faster response time. Thus, even though movement is by scattering, with no continuous border, cells still move together, in a highly directed and persistent fashion.

We show that absent low densities, or the capacity to deform the substrate, free space appears to not only be sufficient for inducing sheet motion, but necessary. Gradients in cell contractility, in apoptosis, and in motility were generated along one axis

of the monolayer with no free space, and in none of these cases did there appear to be any asymmetry in motion. The one violation of this rule, is at low, but still confluent, densities. Under these scenarios, you get the evolution of long timescale and lengthscale vector fields. Thus to have highly coordinated motion of non-compliant surfaces, either free space or low density is necessary. As neither exist in any *in vivo* epithelia, these are not likely appropriate models.

## 6.2 Density and Contact Dependence in Compliant and Non-Compliant Models

This work clarifies the relationship between density (as a correlate of cell-cell contact), and the compliance of the substrate, in the dynamics of a confluent monolayer. We already know from previous studies that simultaneously, high density and non-compliant substrates hinder fast, correlated movement. As has been shown in both the presence and absence of free space (i.e. denudation models in Chapter 2, and non-compliant substrate studies in Chapter 3), cell-cell contact reduces single cell speed and direction, as well as weakens correlated motion amongst the population. However, when the substrate to which the monolayer adheres, is viscoelastic, and further, is deformable by the cells themselves, density and contact actually *drive* correlated dynamics. The relevance of cell-cell contact is further underscored by the fact that the movement of single cells, or small colonies is hindered on these surfaces. It is only with high confluency, that fast, and highly correlated dynamics emerge.

These observations are confirmed by:

1. There is no difference in the equilibrium temporal scaling behavior of the velocity autocorrelation function,  $\langle v(0)v(\tau) \rangle \sim \tau^{-0.79}$ , for dense movement either with or without E-cadherin, on non-compliant surfaces ( $p = 0.60$ ,  $N=5$ ). This suggests that the natural state of a dense monolayer is that the dynamics of

each cell are autonomous.

2. Blocking of E-cadherin on substrates with  $|G|$  below 60Pa, results in a change in scaling of  $\langle v(0)v(\tau) \rangle$ , from  $\sim 1/\tau^{0.78}$  to  $\sim 1/\tau^{1.0}$  ( $p = 3.29 * 10^{-5}$ ,  $N=10$ ), indicating that to persist with a given speed requires cell contact, and that cell motion is not autonomous. This scaling behavior is also identical to that for cells on non-compliant substrates.
3. The scaling of the mutual velocity correlation,  $\langle v(0)_1 v(\tau)_2 \rangle$  decreases with ablated cell contact. Thus, there is more coordinated group motion (as determined by an ensemble averaged, pairwise correlation function) with contact than without.

The most correlated state is parametrized by low resistance to shear and high density, per the aforementioned description. It can be further characterized as distinct, not just dynamically, but in its geometric organization, as well as morphological characteristics.

This is confirmed by:

1. The density correlation,  $G(r, \tau)$ , decays strongly for dense monolayers, for  $|G| < 60Pa$ , with lengthscales on the order of 1-2 cell diameters ( $\tau^* \sim 1$  hr). On non-compliant substrates ( $G_{substrate}|\omega| > 100Pa$ ), this lengthscale is over a hundred  $\mu\text{m}$  ( $\tau^* \sim 12$  hr).
2. The morphology of individual cells, has switched from flattened structures (lamellipodia), to more elongated ones, where there is less contact with the surface (filopodia).
3. Correlated dynamics are coincident with the destabilization with respect to the surface, as measured by the texturizing of the surface adhesive protein.

# Chapter 7

## Future Work

The clear bridge between the second and third chapters, would be to have deformable substrates inside the microfluidic channels. While there it is clear that substrate viscoelasticity can alter the level of correlated migration, there is still one remaining question - how do we break symmetry? Can there be any net movement? In my substrate studies, there is no free space, and thus the correlated motion takes the form of fluctuations, or oscillations of domains of cells, with no real net motion. For that, there needs to be asymmetry. The first priority would be to repeat the denudation experiments inside of this channel. To see how wounds can be healed inside a physically relevant mechanical environment would change the field. Therefore, to approach this problem, deformable media would likely need to be flowed into a preformed chip, and then adhered to the inside. Since the goal is to have a material which is soft, there is no real option for bonding directly to the chip. Both polyacrylamide and PDMS, which are the most common cellular substrata, have can have the surface aldehydes necessary to make the material reactive with activated glass or PDMS, these materials (or anything else) that soft would not support compression for bonding, neither would it be practical to even hold. The most promising scenario would be to flow in a second phase of silane-reactive polymer that can either be reacted with the glass or the PDMS chip. If not reacted, the top part of the chip, the PDMS channel, may actually be swollen, for the insertion of other polymers, and then dehydrated.

Also, the main problem with Chapter 4, is that stamping on soft PDMS requires covalent attachment, which also likely modifies the stiffness of the surface. Therefore, we would likely need to abandon this method, and find an alternative method for strong attachment of surface protein. One potential option is to use one similar to what was previously mentioned for incorporating a second polymer phase into a microfluidic chip - swelling. To swell, insert, and then deswell, can lock in various kinds of polymers, without the need for covalent attachment. While not as strong, they are may be likely strong enough to not be pulled off by the cells. The first thing that might be worth trying would be some long (for tangling) PEG-amine or PEG-COOH linkage. The long chain may be entangled, with the suspended reactive end. There is no way to really orient the polymer in the right direction, so high concentrations of polymer would need to be incorporated, just to make sure that there are enough reactive groups left on the surface, for reacting with the surface protein. Clearly, no further cell exclusion chemistry would be necessary, as the main problem here is getting protein to even attach in the first place.

# Chapter 8

## Derivations and Tutorials

The following is part of a tutorial on Statistical Mechanics that contains many of the derivations that I used in some of the modeling and simulation in my own work, which I decided to expand upon for the students of 20.410, the graduate course in Biomechanics in the fall of 2007. It is included here as a reference to my work.

### 8.1 Why Statistical Mechanics?

#### **What is the objective?**

Makes predictions about the macroscopic properties of a system based on the microscopic details, i.e. molecular, atomistic structural detail. Thermodynamic properties can be easily derived, such as Entropy, Free Energy, Pressure, Specific Heat, etc.

#### **Why do we need statistical mechanics?**

Thermodynamics is just a phenomenological theory, and does not connect to the microscopic parameters - what we want to know about.

#### **How do we create this connection?**

If we realize that the bulk thermodynamic properties of a material are caused by the average behavior of all of the molecules in the system, then we can try and enumerate

these behaviors at the microscopic level, the 'microstates' of the system. Once we know all of these 'microstates', we can connect directly to the free energy and every other observable, macroscopic thermodynamic quantity. For this, we rely on classical mechanics, as we consider biological and other 'soft matter' to be continuous media, and intend to derive results at the mesoscopic and macroscopic level (and we do not need quantum descriptions). Further, we can develop equations of state, such as the Ideal Gas Law, and Hooke's Law.

### **How does this relate to biological matter?**

We use statistical mechanics to understand the behavior of all matter where thermal energy is a relevant to their function. As biological matter can be found at small lengthscales, where thermal energy plays a large role from the natural equilibrium state and configuration of small molecules and proteins, to the force-length relationship of biopolymers, statistical mechanics gives us a formalism to understand the role of stochasticity. We can even tie this formalism back to thermodynamics, so that we have unified macroscopic and microscopic descriptions of the behavior of biological (soft) matter.

### **Specifically, we can answer questions like the following:**

What is the contribution of entropy to the force-length relationship for a polymer (DNA, RNA, etc)?

What is the influence of applied force on the energy barrier between the folded and unfolded states of a protein?

How do ionic solutions influence protein-protein interaction (recognition /binding /aggregation)?

What is the contribution to bending and rigidity from charge on biopolymers (e.g. the bending of DNA considering it as a polyelectrolyte)?



## 8.2 Definitions

Phase Space: The set of all positions and momenta allowed by the thermodynamic constraints (classical definition).

Microstate: The set of positions and momenta of the system for any given time - a subset of phase space.

Macrostate: a set of thermodynamic variables that corresponds to a collection of microstates (i.e.  $(N,V,E)$ ,  $(N,V,T)$ ,  $(V,T,\mu)$  will all be associated with a separate set of microstates)

Ensemble: The complete collection of all microstates that pertain to a macrostate. Each microstate must be unique, but sharing one or more macroscopic characteristics with other unique microstates (e.g. all have the same total energy). There are two ensembles we will be concerned with in this course, the microcanonical,  $(N,V,E)$ , and the canonical,  $(N,V,T)$ .

Density of states (aka Boltzmann Factor),  $\Omega(E)$ : a weighing factor for the probability of finding the system in a microstate at the energy,  $E$ .

$$\Omega(E) = e^{S/k_B} = e^{-E/k_B T} \quad (8.1)$$

Partition Function,  $Z$ : The total distribution of energy among each of the microstates accessible to a system at a given temperature. It is a sum over each boltzmann factor for each energetically unique microstate.

$$Z = \sum_j e^{-\beta E_j} \quad (8.2)$$

Boltzmann Probability: the normalized probability of observing a particular microstate, as weighted by its energy. It is the number of configurations that correspond to that energy (boltzmann factor) divided by the weighted sum of the number of possible states (the partition function).

$$P_i = \frac{\Omega(E)}{Z} = \frac{e^{-\beta E_i}}{\sum_j e^{-\beta E_j}} \quad (8.3)$$

**Examples we reference in this course:**

Ideal Gas

Ideal Polymer (Freely Jointed Chain)

Non-Ideal Polymer (Worm-Like Chain Polymer)

## 8.3 How do we approach the construction of a S.M. problem?

### 1) Define the system

Is the system open? (heat, mass, work, can cross the boundary)

Is the system isolated? (no heat, mass, or work transfer across the boundary)

Is the system closed? (no mass can cross, but heat and work can cross the boundary)

From this, we will know what ensemble to use (usually a choice between Micro-canonical and Canonical, see next section). Our only stipulation is that the system must be in thermal equilibrium.

### 2) Make macroscopic observations - capture system in different states

$$B_{obs} = \sum_v^N P_v B_v = \langle B \rangle \quad (8.4)$$

We know that what we observe is just an average, and that each microstate actually occurs with some probability,  $P_v$ , which we model by our choice of ensemble. We usually try to enumerate all of these probabilities (and thereby construct a complete partition function) by repeated observation.

For example, if we chose a closed system, where within a subsystem, microstates are not equally likely, then we say that the probability is weighted by its associated energy penalty.

$$P_v \sim e^{-\beta E_v} \quad (8.5)$$

Which if we have sampled enough, we will have for each microstate, or energy  $E_v$ , so we have a full enumeration of each of the N states:

$$Z = e^{-\beta E_1} + e^{-\beta E_2} + \dots + e^{-\beta E_N} = \sum_v e^{-\beta E_v} \quad (8.6)$$

### 3) Calculate Thermodynamic (or other) properties from Partition Function

Once we have the partition function, we can calculate ANY macroscopic, thermodynamic quantity (see later sections), for example the Helmholtz free energy:

$$F = -\frac{\ln(Z)}{\beta} \quad (8.7)$$

## 8.4 Important Principles

**Equal a priori probability:** For an isolated system (E,N,V), all microstates are equally probable. This means that any collection of configurations that we can observe in our system (positions and momenta of particles, configurations of polymers) are equally likely when we take different snapshots in time. Can also be stated in a different form, called the Ergodic hypothesis...

**Ergodic Hypothesis:** given an infinite amount of time, the system will visit all possible microstates. In short, TIME AVERAGE = ENSEMBLE AVERAGE.

$$\langle A \rangle = \sum_v P_v A_v = \lim_{T \rightarrow \infty} \frac{1}{T} \int_0^T a(t) dt \quad (8.8)$$

Issue of Practicality: ergodicity is a concept of convenience. Technically, we can't prove if something will sample space given an infinite amount of time, because we can't wait that long. Therefore, we usually just ask whether or not we can view a large sampling of states given our experimental timescales, meaning how long we are willing to wait. If we can observe a large amount of states, we call the system ergodic. Certain systems (lookup: glasses), have kinetic effects that prevent them from sampling all states in realizable times. They have found a state which is relatively stable, but not the most stable, equilibrium state. Since the state is very stable, and there is a large energetic barrier to leaving, it will never do so.

For this class, we ask will polymers (DNA, RNA, etc.) sample space within experimentally feasible times? The answer is usually YES.

**Equipartition of Energy:** if the energy of a thermally driven system depends on the square of position or speed (think springs, for example) then the mean energy for each degree of freedom is  $1/2 kT$  (i.e. a spring allowed to move in three dimensions will have three degrees of freedom, and so has an average energy of  $3/2 kT$ ).

For example, if we are looking at the kinetic energy of a particle diffusing in

three-dimensional space, then we know that its K.E. can be expressed as:

$$\frac{m\langle v^2 \rangle}{2} = \frac{m\langle v_x^2 \rangle}{2} + \frac{m\langle v_y^2 \rangle}{2} + \frac{m\langle v_z^2 \rangle}{2} = \frac{3kT}{2} \quad (8.9)$$

## 8.5 Microcanonical Ensemble (N,V,E)

The microcanonical ensemble is based on the a priori assumption that each particle/subsystem has the same energy, therefore all states are equally likely. The system is isolated, so the total energy is fixed, and does not fluctuate.

It is important to note that the canonical ensemble (next section) is a degenerate form of the microcanonical ensemble. We can always choose a smaller subsystem, where the energy does not need to remain constant, as it can be counter-balanced by the larger system it is in thermal contact with. Therefore, as we will see later, whenever we refer to a system where particles or subsystems do not have the same energy, we acknowledge that we are only looking at a small window of a much larger picture.

$\Omega_m$  = the number of ways we can arrange the components of the system given the thermodynamic constraints, i.e. that they all have the same energy (ideal particles can be arranged in a box, number of configurations ideal polymers can take, from extended to curled up).

$$P_i = \frac{1}{\Omega_m} \quad (8.10)$$

Since  $\Omega_m$  is essentially just the total number of microstates, the entropy for the system is the logarithm of this quantity. And as can be seen, this essentially plays the role of the partition function, although for the microcanonical (and grand-canonical) ensemble, we calculate the entropy with the density of states, as it pertains to a specific energy state.

$$S = k_B \ln(\Omega_m) \quad (8.11)$$

### What is this ensemble good for?

We tend to use this case for systems that are generally just driven by entropy, and the system is purely configurational, such as Ideal Gases, and Ideal Polymers (Freely-

Jointed Chain).



## 8.6 The Canonical Ensemble (N,V,T)

The canonical system refers to a subsystem (where energy does not need to remain constant), of a larger system (where it does). Consider a subsystem (A), as we have previously defined, as being in thermal contact with a much larger reservoir (B), that has a constant temperature. Within our subsystem, which we term CLOSED (by our previous definition), the microstates accessible to our subsystem are NOT equally probable, and there is an associated energy penalty for each state. However, if we consider our subsystem + reservoir, then the total energy for the total system is constant, and all microstates of this combined system are equally likely (the total system is ISOLATED) Essentially, this allows us to come up with scenarios where different configurations should cost different amounts of energy (imagine configurations of a polymer, where clearly an extended polymer should have a greater penalty than a stable, collapsed polymer), but we don't have to violate one of our mandatory laws of statistical mechanics, which is that equilibrium all microstates must be equally likely and that energy must be conserved.

The probability for each of the microstates accessible to our subsystem is described by the boltzmann factor. Therefore, the total number of microstates of system A with energy  $E_A$  and likewise for B is expressed as:

$$\Omega_A(E_A) = e^{S_A(E_A)/k_B}, \quad \Omega_B(E_B) = e^{S_B(E_B)/k_B} \quad (8.12)$$

The probability of identifying the microstates that have energies  $E_A$  and  $E_B$  for systems A and B separately are:

$$P(E_A) = \frac{\Omega_A(E_A)}{\Omega_{tot}}, \quad P(E_B) = \frac{\Omega_B(E_B)}{\Omega_{tot}} \quad (8.13)$$

However, if the systems are in thermal equilibrium with each other (b/c remember, they can transfer heat), then we know that their entropies are equal, which means their boltzmann factors are equal:

$$P(E_A) = \frac{\Omega_B(E_B)}{\Omega_{tot}} \quad (8.14)$$

Noting that  $\Omega_{tot}$  refers to the number of states of the whole system, which is ISOLATED, essentially we are back in the microcanonical, and we can say that each of the microstates are equally likely (only in this reference frame), and thus  $P_0 = \frac{1}{\Omega_{tot}}$ , and so:

$$P(E_A) = \Omega_B(E_B)P_0 \quad (8.15)$$

We also stipulated that our subsystem must be much smaller than the reservoir, so that we can say that the entropy (or energy of density of states for that matter) is much larger for the reservoir than for our system, so that we can approximate it as the total:

$$S_B(E_B) = S_B(E_{tot} - E_A) \sim S(E_{tot}) - E_A \frac{dS}{dE_B} = S(E_{tot}) - E_A/T \quad (8.16)$$

Then we can say that the probability of observing the subsystem (what we are interested in) can be expressed in terms of:

$$P(E_A) = e^{S_B/k_B} P_0 = e^{\frac{S(E_{tot}) - E_A/T}{k_B}} P_0 = e^{S_{tot}/k_B} e^{-E_A/k_B T} P_0 \quad (8.17)$$

where the first exponential is just some constant. The probability is therefore proportional to the exponent of the energy penalty for that configuration.

$$P(E_A) \sim e^{-E_A/k_B T} \quad (8.18)$$

That being the case, we want to normalize by all of the accessible microstates available to system A, which means dividing by the partition function.

$$Z = \sum_j e^{-\beta E_{A,j}} \quad (8.19)$$

When we do this, we get the well-known Boltzmann distribution, and probability in the canonical ensemble,

$$P(E_{A,i}) = \frac{e^{-E_{A,i}/k_B T}}{\sum_j e^{-\beta E_{A,j}}} \quad (8.20)$$

Since we are only talking about the subsystem A, we can say that within these confines, all microstates are not equally probable, and there is an energy penalty for every distinct configuration.

### **What will this ensemble be useful for?**

When we consider non-ideal polymers, where there is an enthalpic (not just entropic) contribution to elasticity, that different configurations are more or less likely based on how they are stretched.

## 8.7 Freely Jointed Chain

The freely jointed chain is a system of  $N$  connected rigid segments, each of length  $b$ . Entropy is the only force that opposes extension, as there is no energy penalty for bending.

Derivation of the Mean end-to-end distance (no force)

$$\langle R_{ee}^2 \rangle = \left\langle \sum_i \vec{b}_i \sum_j \vec{b}_j \right\rangle \quad (8.21)$$

$$\langle R_{ee}^2 \rangle = \left\langle \sum_i \sum_j \vec{b}_i \cdot \vec{b}_j \right\rangle \quad (8.22)$$

$$\langle R_{ee}^2 \rangle = \sum_i \sum_j \langle b^2 \cos \theta \rangle \quad (8.23)$$

$$\langle R_{ee}^2 \rangle = N^2 b^2 \langle \cos \theta \rangle \quad (8.24)$$

$$\langle R_{ee}^2 \rangle = N b^2 \sum_i \cos \theta_i \quad (8.25)$$

$$\langle R_{ee}^2 \rangle = N b^2 \left( 1 + \frac{\theta^2}{4} \right) \quad (8.26)$$

Or, for the smallest angle approximation,

$$\langle R_{ee}^2 \rangle = N b^2 \quad (8.27)$$

This is the mean end-to-end distance (and  $d$  is the dimension of the system), the typical measure of the size of a coiled entropic polymer.

Derivation of the Mean end-to-end distance (applied force)

$$\langle \vec{R}_{ee} \rangle = k_B T \frac{\partial Z}{\partial F} \quad (8.28)$$

$$\frac{\partial Z}{\partial F} = \frac{\partial}{\partial F} \sum_i e^{\frac{\vec{F} R_{ee,i}}{k_B T}} \quad (8.29)$$

$$\frac{\partial Z}{\partial F} = \frac{1}{k_B T} \sum_i R_{ee,i} e^{\frac{\vec{F} R_{ee,i}}{k_B T}} \quad (8.30)$$

$$\frac{\partial Z}{\partial F} = \frac{1}{k_B T} \sum_i R_{ee,i} e^{\frac{\vec{F} R_{ee,i}}{k_B T}} \quad (8.31)$$

$$\frac{\partial Z}{\partial F} = \frac{1}{k_B T} \sum_i R_{ee,i} e^{\frac{\vec{F} R_{ee,i}}{k_B T}} \quad (8.32)$$

$$P(R_{ee}, i) = \frac{e^{\frac{\vec{F} R_{ee,i}}{k_B T}}}{Z} \quad (8.33)$$

$$\frac{\partial Z}{\partial F} = \frac{1}{k_B T} \sum_i R_{ee,i} P(R_{ee,i}) Z \quad (8.34)$$

$$\frac{\partial Z}{\partial F} = \frac{1}{k_B T} \langle R \rangle Z \quad (8.35)$$

Rearranging,

$$\langle R \rangle = \frac{\partial Z}{\partial F} \frac{k_B T}{Z} \quad (8.36)$$

$$\langle R \rangle = \frac{\partial \ln Z}{\partial F} k_B T \quad (8.37)$$

In 2D,

$$Z = \left[ \int_0^{2\pi} e^{\frac{F b \cos \theta}{k_B T}} d\theta \right]^N \quad (8.38)$$

In 3D,

$$Z = \left[ \int_0^{2\pi} \int_0^\pi e^{\frac{F b \cos \theta}{k_B T}} \sin \theta d\theta d\phi \right]^N \quad (8.39)$$

By integrating these quantities, and then differentiating them with respect to the applied force, we can find the mean end-to-end distance.

### Derivation of the Force-length relationship: Entropic Elasticity

The following derivation traces the force-length relationship in a freely jointed chain, which has purely an entropic contribution to elasticity. It can be done for any dimension, as the probability density function for the end-to-end length is the only part that depends on dimension.

$$\vec{F} = \frac{\partial A}{\partial R_{ee}} \quad (8.40)$$

$$A = E - TS \quad (8.41)$$

$$S = k_B \ln \Omega(\vec{R}_{ee}) \quad (8.42)$$

$$P(\vec{R}_{ee}) = \frac{\Omega(\vec{R}_{ee})}{\Omega_{tot}} \quad (8.43)$$

$$P(R_{ee}, N) = \left(\frac{d}{2\pi N b^2}\right)^{d/2} e^{-\frac{dR_{ee}^2}{2Nb^2}} \quad (8.44)$$

$$S = k_B \ln \Omega(\vec{R}_{ee}) = k_B \ln \Omega_{tot} + k_B \ln P(\vec{R}_{ee}) \quad (8.45)$$

The total number of configurations is a constant, as it does not depend on the end-to-end distance, as is the coefficient of the gaussian.

$$S = C - k_B \frac{dR_{ee}^2}{2Nb^2} \quad (8.46)$$

$$A = E - TS = C' + \frac{dR_{ee}^2}{2Nb^2} k_B T \quad (8.47)$$

$$\vec{F} = \frac{\partial A}{\partial R_{ee}} = \frac{dR_{ee}}{Nb^2} k_B T \quad (8.48)$$

This is the force due to entropic elasticity, and  $d$  is the dimension of the system.

## 8.8 Worm-Like Chain

Derivation of the Mean end-to-end distance

Recall that if we are talking about a polymer in 2D, the correlation between tangents should decay with  $\frac{1}{2l_p}$ , and for 3D, should decay with  $\frac{1}{l_p}$  (this is represented in  $\alpha$  below).

$$\langle R_{ee}^2 \rangle = \int_0^L ds_i \int_0^L ds_j \langle \vec{t}_i \vec{t}_j \rangle \quad (8.49)$$

$$\langle R_{ee}^2 \rangle = \int_0^L ds_i \int_0^L ds_j e^{-\frac{|s_i - s_j|}{\alpha l_p}} \quad (8.50)$$

We are going to want to integrate over this quantity, but since there is an absolute value over the separation between tangent vectors, we can just pick an orientation, and bring out a factor of two, because the two directions are equivalent. Also, the intergral for the second spatial coordinate is only up to the first. Think that we pick one point along the polymer and move it from 0 to L. But the second, will always be behind the first, because we are intergrating a separation. Therefore the second only needs to be integrated from 0 to the first point.

$$\langle R_{ee}^2 \rangle = 2 \int_0^L e^{-\frac{s_i}{\alpha l_p}} ds_i \int_0^{s_i} e^{\frac{s_j}{\alpha l_p}} ds_j \quad (8.51)$$

$$\langle R_{ee}^2 \rangle = 2\alpha l_p \int_0^L e^{-\frac{s_i}{\alpha l_p}} ds_i (e^{\frac{s_i}{\alpha l_p}} - 1) \quad (8.52)$$

$$\langle R_{ee}^2 \rangle = 2\alpha l_p \int_0^L ds_i (1 - e^{-\frac{s_i}{\alpha l_p}}) \quad (8.53)$$

$$\langle R_{ee}^2 \rangle = 2\alpha l_p ((L - 0) + \alpha l_p (e^{-\frac{L}{\alpha l_p}} - 1)) \quad (8.54)$$

$$\langle R_{ee}^2 \rangle = 2\alpha l_p (L + \alpha l_p (e^{-\frac{L}{\alpha l_p}} - 1)) \quad (8.55)$$



### Derivation of the Force-length relationship

We can calculate the force-length relationship of the Worm Like Chain model similarly, although the partition function itself is more difficult to solve. As opposed to the constant internal energy of a freely jointed chain, the internal energy of a worm-like chain will depend on the extension.

$$\langle \vec{R}_{ee} \rangle = k_B T \frac{\partial Z}{\partial F} \quad (8.56)$$

### Derivation of the Energy of Bending

$$\frac{[energy]}{[volume]} = \frac{[force]}{[area]} * \frac{[changeinlength]}{[originallength]} \quad (8.57)$$

$$\frac{[force]}{[area]} * \frac{[changeinlength]}{[originallength]} = \frac{[F]}{[A]} * \frac{\Delta L}{L} * \frac{1}{2} \quad (8.58)$$

Remember that there is a factor of 1/2, because there are two  $\Delta L$ 's, because the bending of a beam causes one side to be compressed, and the other to be extended, by the same quantity. However, the same energy required to bend causes both of these changes.

$$\frac{[F]}{[A]} = \sigma = E \frac{\Delta L}{L} \quad (8.59)$$

$$E_{bend} = \frac{[energy]}{[volume]} = \frac{E}{2} \left( \frac{\Delta L}{L} \right)^2 \quad (8.60)$$

If we then want to find the energy per unit length, we can integrate this quantity with respect to the cross sectional area.

recalling that  $\Delta L = \frac{x}{R_L} * L$ ,

$$\frac{E_{bend}}{L} = \frac{E}{2R_L^2} \int x^2 dA \quad (8.61)$$

$\int x^2 dA$  is the moment of inertia, I

$$\frac{E_{bend}}{L} = \frac{EI}{2R_L^2} \quad (8.62)$$

This is the energy of the bend per unit length. We can also express this quantity in terms of a bend angle,  $\theta$ , by using  $L = R_L\theta$

$$E_{bend} = \frac{EI\theta^2}{2L} \quad (8.63)$$

This is the energy of bending a rod, what we use to modify Worm Like Chain, which becomes important when we want to do things like calculate the persistence length.

Calculation of the persistence length

Using the above result, with EQUIPARTITION OF ENERGY, we can take the mean energy of bending and equate it as such:

$$\langle E_{bend} \rangle = \frac{1}{2}k_B T \quad (8.64)$$

$$\left\langle \frac{EI\theta^2}{2L} \right\rangle = \frac{1}{2}k_B T \quad (8.65)$$

Rearranging,

$$\langle \theta^2 \rangle = \left( \frac{k_B T}{EI} \right) L \quad (8.66)$$

Acknowledging that the amount the polymer is going to bend will be equal to the ratio of its absolute, contour length, to the length that the polymer 'persists' as straight will be equal to  $L/\text{some constant}$ , we know that the following quantity is that constant, called the persistence length.

$$\langle \theta^2 \rangle = \left( \frac{k_B T}{EI} \right) L = \frac{L}{l_p} \quad (8.67)$$

where  $l_p = \frac{EI}{k_B T}$ .

## 8.9 Derivation of the Master Equation

The master equation is a first order differential equation that describes the evolution of probabilities in time. This is the probability of occupying one of a number of discrete states. From this equation, we can develop the fokker-planck equation.

We will present here the formalism for species diffusion.

The probability of having  $n$  molecules at a time  $t$  is:  $p_n(t)$

The probability of having  $n$  molecules  $dt$  later is:  $p_n(t + dt)$ , which can be calculated by the probability of occupying that state at a previous time ( $t$ ) and the probability of transitioning to  $t+dt$ :

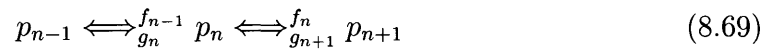
$$p_n(t + dt) = p_n(t) + dp_n(t \rightarrow t + dt) \quad (8.68)$$

where we can extrapolate on the derivative by considering aoo of the ways you can transition into and out of the  $n$  stage:

(1): Creation:  $n-1$  to  $n$  or (3)  $n$  to  $n+1$

(2): Destruction:  $n$  to  $n-1$  or (4)  $n+1$  to  $n$

This is illustrated here:



This can be reformulated as an ordinary differential equation:

$$\frac{dp_n}{dt} = -(f_n + g_n)p_n + f_{n-1}p_{n-1} + g_{n+1}p_{n+1} \quad (8.70)$$

This is known as the Master Equation.

## 8.10 The Fokker-Planck Equation

The fokker-planck equation is used to describe the time evolution of the probability density function for position or velocity, and is often applied to the brownian motion of particles in fluids.

We can use a general taylor series to extrapolate f and g from the master equation:

$$h(n + \Delta n) = h(n) + \frac{\partial h}{\partial n} \Delta n + \frac{1}{2} \frac{\partial^2 h}{\partial n^2} \Delta n^2 + O(\Delta n^3) \quad (8.71)$$

$$f(n - 1)p(n - 1) = f(n)p(n) - \frac{\partial}{\partial n} f(n)p(n) + \frac{1}{2} \frac{\partial^2}{\partial n^2} f(n)p(n) + \dots \quad (8.72)$$

$$g(n + 1)p(n + 1) = g(n)p(n) - \frac{\partial}{\partial n} g(n)p(n) + \frac{1}{2} \frac{\partial^2}{\partial n^2} g(n)p(n) + \dots \quad (8.73)$$

Back to the master equation, and the time evolution of probabilities,

$$\frac{dp_n}{dt} = -(f_n + g_n)p_n + f_{n-1}p_{n-1} + g_{n+1}p_{n+1} \quad (8.74)$$

$$\frac{dp_n}{dt} = -(f_n + g_n)p_n + (f_n p_n - \frac{\partial}{\partial n} f_n p_n + \frac{1}{2} \frac{\partial^2}{\partial n^2} f_n p_n) + (g_n p_n + \frac{\partial}{\partial n} g_n p_n + \frac{1}{2} \frac{\partial^2}{\partial n^2} g_n p_n) \quad (8.75)$$

This yields the Fokker-Planck Equation:

$$\frac{dp_n}{dt} = -\frac{\partial}{\partial n} ((f_n + g_n)p_n) + \frac{1}{2} \frac{\partial^2}{\partial n^2} (f_n + g_n)p_n \quad (8.76)$$

The term inside the parenthesis is the probability flux,  $J$ . This represents the flux of particles across any boundary. Thus,  $\frac{dp_n}{dt} = -\frac{\partial J}{\partial n}$ .

At steady state,  $\frac{dp_n}{dt} = 0$ .

## 8.11 Fluctuation-Dissipation

The point: the response of a system to a small, external perturbation is the same as the response to a spontaneous fluctuation from equilibrium.

Stoke's Einstein is a version of the fluctuation-dissipation theorem, where the coefficients for fluctuation ( $D$ ) are related to the coefficients for dissipation,  $\eta$ . This is a combination of two perspectives, where we can both model the motion of the particle as a random walk, as well as modeling the forces that act on the particle that cause it to fluctuate in space, and solve Newton's laws subject to that fluctuation force.

Using the diffusion equation with the ensemble average for the mean-squared displacement,

$$\langle \Delta \vec{r}^2(\tau) \rangle = \int \vec{r}^2 P(\vec{r}, \tau) d\vec{r} \quad (8.77)$$

$$\frac{\partial P(\vec{r}, \tau)}{\partial \tau} = D \nabla^2 P(\vec{r}, \tau); \quad (8.78)$$

$$\frac{\partial}{\partial \tau} \langle \Delta \vec{r}^2(\tau) \rangle = \int \vec{r}^2 \frac{\partial}{\partial \tau} P(\vec{r}, \tau) d\vec{r} \quad (8.79)$$

$$\frac{\partial}{\partial \tau} \langle \Delta \vec{r}^2(\tau) \rangle = D \int \vec{r}^2 \nabla^2 P(\vec{r}, \tau) d\vec{r} \quad (8.80)$$

$$\frac{\partial}{\partial \tau} \langle \Delta \vec{r}^2(\tau) \rangle = 6D \int P(\vec{r}, \tau) d\vec{r} \quad (8.81)$$

$$\frac{\partial}{\partial \tau} \langle \Delta \vec{r}^2(\tau) \rangle = 6D \quad (8.82)$$

$$\langle \Delta \vec{r}^2(\tau) \rangle = 6D\tau \quad (8.83)$$

Thus, the result is that the mean-squared displacement is expected to scale linearly with time, at least for a purely viscous fluid.

Now, we will return to Langevin, the set of force balances on a particle that will allow us to connect to the diffusion result.

STEP 1: To create a set of force balances on the particle, we need to not only include the viscous damping term from the medium, the drag on the particle, but also a random force that accounts for the stochasticity in the system. This random force is due to molecular collisions at the microscopic scale.

$$m\dot{v} = f_R(t) - F_{drag} = f_R(t) - bv \quad (8.84)$$

We cannot yet solve this equation, because we don't know the form of the random force. We can however, make further assumptions about its spectra.

STEP 2: Assume that the random force is uncorrelated and constant:

$$\langle f_R(t) * f_R(t + \tau) \rangle = F\delta(\tau) \quad (8.85)$$

This is a delta function, and thus this average only has value when  $\tau$  is equal to zero. This helps us solve the Langevin equation, because the autocorrelation drops the random force term:

$$m\frac{d^2r}{dt^2} + b\frac{dr}{dt} = f_R(t) \quad (8.86)$$

STEP 3: Using our knowledge of how to solve inhomogeneous 1st order ordinary differential equations, we can generate a solution for the velocity:

$$y'(t) + p(t)y(t) = z(t) \quad (8.87)$$

$$y = e^{-a(t)} \left( \int z(t)e^{a(t)} dt + \kappa \right) \quad (8.88)$$

$$a(t) = \int p(s) ds \quad (8.89)$$

This allows us to solve for the velocity:

$$\frac{dr}{dt} = \frac{1}{m} \int_{-\infty}^t f(t') e^{-(t-t')/\tau_R} dt' \quad (8.90)$$

$$\langle \vec{v}(t) * \vec{v}(t + \tau) \rangle = \left\langle \frac{d\vec{r}}{dt}(t) \frac{d\vec{r}}{dt}(t + \tau) \right\rangle \quad (8.91)$$

We can't solve this directly, but we can use ensemble averages.

$$\langle \vec{v}(t) * \vec{v}(t + \tau) \rangle = \left\langle \frac{1}{m} \int_{-\infty}^t f(t') e^{-(t-t')/\tau_R} dt' \frac{1}{m} \int_{-\infty}^{t+\tau} f(t'') e^{-(t+\tau-t'')/\tau_R} dt'' \right\rangle \quad (8.92)$$

$$\langle \vec{v}(t) * \vec{v}(t + \tau) \rangle = \left\langle \frac{1}{m^2} \int_{-\infty}^t \int_{-\infty}^{t+\tau} f(t') f(t'') e^{-(t-t')/\tau_R} e^{-(t+\tau-t'')/\tau_R} dt' dt'' \right\rangle \quad (8.93)$$

Since the random force,  $f_R$  is random and uncorrelated, this function only has value when  $t' = t''$ , which gives the magnitude of the random force,  $F$ .

$$\langle \vec{v}(t) * \vec{v}(t + \tau) \rangle = \frac{F\tau_R}{2m^2} e^{-(t-t')/\tau_R} e^{-(t''+\tau-t'')/\tau_R} \quad (8.94)$$

$$\langle \vec{v}(t) * \vec{v}(t + \tau) \rangle = \frac{F\tau_R}{2mb} e^{-(\tau)/\tau_R} \quad (8.95)$$



$$\langle \vec{v}(t) * \vec{v}(t + \tau) \rangle = \frac{F\tau_R}{2mb} e^{-(\tau b)/m} \quad (8.96)$$

Then we use Stoke's Drag,  $b = 6\pi\eta a$ ,

$$\langle \vec{v}(t) * \vec{v}(t + \tau) \rangle = \frac{F}{12m\pi\eta a} e^{-(6\pi\eta a\tau)/m} \quad (8.97)$$

STEP 4: Take limit of long time,  $\tau \rightarrow \infty$

$$\langle \vec{v}(t) * \vec{v}(t + \tau) \rangle = \frac{F}{12m\pi\eta a} \quad (8.98)$$

STEP 5: Assume Medium acts as Harmonic Spring, Equipartition Holds

$$\frac{1}{2}m\langle v_0^2 \rangle = \frac{3}{2}k_B T \quad (8.99)$$

$$\langle v_0^2 \rangle = \frac{3}{m}k_B T = \frac{F}{12m\pi\eta a} \quad (8.100)$$

The magnitude of the random force is now:

$$F = 36\pi\eta a k_B T \quad (8.101)$$

Use Equipartition in the velocity autocorrelation to solve for the mean-square displacement. Then we can combine the Langevin result with the Diffusion Result to get the Einstein relation.

$$\langle \vec{v}(t) * \vec{v}(t + \tau) \rangle = \frac{F}{12m\pi\eta a} e^{-(6\pi\eta a\tau)/m} = \frac{3}{m}k_B T e^{-(6\pi\eta a\tau)/m} \quad (8.102)$$

$$\vec{r}(t) = \int_0^t \langle \vec{v}(t) * \vec{v}(t + \tau) \rangle d\tau \quad (8.103)$$

$$\langle \vec{r}(t) * \vec{r}(t) \rangle = \frac{\tau k_B T}{\pi\eta a} \quad (8.104)$$

We can then combine this Langevin result with our Diffusion Result,

$$\langle \Delta \bar{r}^2(\tau) \rangle = 6D\tau, \quad (8.105)$$

We have now connected the fluctuation of the particle ( $D$ ) with the dissipation of the medium ( $\eta$ ) in our version of Fluctuation-Dissipation. These coefficients are the diffusivity and viscosity of the medium, respectively ( $a$  is the particle radius).

$$D = \frac{k_B T}{6\pi\eta a} \quad (8.106)$$

This result has been found to be surprisingly accurate, down the molecular scale, as long as we can make the assumption that the fluid is a continuum.

When we discuss microrheology later, we will use the Stokes-Einstein relation again, but we will 'generalize it' for a viscoelastic material. This means that instead of having a simple fluid with a constant viscosity  $\eta$ , the viscosity is now frequency dependent:

$$\langle r(s)^2 \rangle = \frac{k_B T}{s^2 \pi \eta(s) a} \quad (8.107)$$

We can extract knowledge about the system's resistance to shear via this complex viscosity and the maxwell model for a simple fluid,

$$G(s) = s\eta(s) \quad (8.108)$$

To get an expression for the shear modulus in terms of the fluctuation of the particle and the thermal energy:

$$G(s) = \frac{k_B T}{s a \pi \langle r(s)^2 \rangle} \quad (8.109)$$

## 8.12 Basic Thermodynamics

General Concepts:

- (1) Energy in the Universe is constant
- (2) Entropy in the universe is increasing

First Law:

$$dE = dQ + dW \quad (8.110)$$

Reversible processes:

$$dQ_{rev} = TdS \quad (8.111)$$

$$dW = -PdV + \vec{F}d\vec{r} \quad (8.112)$$

$$\Delta S_{universe} = \Delta S_{system} + \Delta S_{surroundings} \quad (8.113)$$

Fundamental Energy Equation

$$dE = Tds - PdV + Fdr \quad (8.114)$$

$$T = \left. \frac{dE}{dS} \right|_{v, \vec{r}} \quad (8.115)$$

Helmholtz free energy

$$A = E - TS \quad (8.116)$$

$$dA = -SdT - PdV + Fdr \quad (8.117)$$

$$F = \left. \frac{dA}{dR} \right|_{v, T} \quad (8.118)$$

Equilibrium and Extremes (closed systems)

(1) Const  $E, V, \vec{r}$  (isolated) - max  $S$

(2) Const  $T, V, \vec{r}$  - min  $A$

(3) Const  $T, P, \vec{r}$  - min  $G$

$dV$  and  $dP$  are very small in biological problems, so  $dG \approx dA$

## 8.13 Useful Mathematics

\*This page is adapted from Jorge Ferrer, 2005, 20.410\*

Commonly forgotten properties of summations(I)

$$\langle x_i \rangle = \frac{1}{N} \sum_{i=1}^N x_i = \frac{1}{N} (x_1 + x_2 + x_3 + \dots) \quad (8.119)$$

Commonly forgotten properties of summations(II)

$$\sum_{i=1}^N Ax_i = (Ax_1 + Ax_2 + \dots + Ax_N) = A(x_1 + x_2 + \dots + x_N) = A \sum_{i=1}^N x_i \quad (8.120)$$

Commonly forgotten properties of summations(III)

$$\sum_{i=1}^N (x_i + y_i + z_i) = \sum_{i=1}^N x_i + \sum_{i=1}^N y_i + \sum_{i=1}^N z_i \quad (8.121)$$

Gaussian Integrals (I)

$$\int_{-\infty}^{\infty} e^{-ax^2} dx = \sqrt{\frac{\pi}{a}} \quad (8.122)$$

Gaussian Integrals (II)

$$\int_0^{\infty} x^2 e^{-ax^2} dx = \frac{1}{4a} \sqrt{\frac{\pi}{a}} \quad (8.123)$$

Continuum Approximation (probability):

$$P(E) = \frac{e^{-E_i/k_B T}}{\sum_j e^{-\beta E_j}} = \frac{e^{-E/k_B T}}{\int_{-\infty}^{\infty} e^{-\beta E}} \quad (8.124)$$

Continuum Approximation (ensemble average):

$$\langle x \rangle = \sum_v P_v x_v = \int_{-\infty}^{\infty} xp(x) dx \quad (8.125)$$

Stirling's Approximation

$$\ln N! \sim N \ln N - N \quad (8.126)$$

## 8.14 Thermodynamic Variables and the Partition Function

Helmholtz Free Energy

$$F = -\frac{\ln(Z)}{\beta} \quad (8.127)$$

Mean Energy

$$\langle E \rangle = -\frac{\partial \ln Z}{\partial \beta} \quad (8.128)$$

Energy Fluctuation

$$\langle (\delta E)^2 \rangle = \frac{\partial^2 \ln Z}{\partial \beta^2} \quad (8.129)$$

Pressure

$$P = -\frac{\partial F}{\partial V}_{N,T} = \frac{1}{\beta} \frac{\partial \ln Z}{\partial V}_{N,T} \quad (8.130)$$

Entropy

$$S = \frac{\partial}{\partial T} k_B T \ln Z \quad (8.131)$$

Heat Capacity

$$C_v = \frac{\partial \langle E \rangle}{\partial T}_{N,V} \quad (8.132)$$

Heat Capacity

$$C_p = \frac{\partial \langle E \rangle}{\partial T}_{N,P} \quad (8.133)$$

## 8.15 Example: Proving the Ideal Gas Law

\*This example adapted from Peter Lee, 20.310, 2004\*

Consider a particle of volume  $V_m$  inside a closed container of volume  $V_i$ , where  $V_i \gg V_m$ . Assume that each location of the molecule is equally probable.

Let  $\omega_1$  = the number of ways of arranging this molecule.

$$\omega_1 = \frac{V_i}{V_m} \quad (8.134)$$

Let  $\omega_2$  = the number of ways of arranging a second molecule

$$\omega_1\omega_2 = \frac{V_i}{V_m} \frac{V_i - V_m}{V_m} \quad (8.135)$$

Since we said that  $V_i \gg V_m$ , then

$$\omega_1\omega_2 \sim \frac{V_i}{V_m} \frac{V_i}{V_m} = \left(\frac{V_i}{V_m}\right)^2 \quad (8.136)$$

We can then generalize this for a system of  $N$  molecules

$$W_i = \left(\frac{V_i}{V_m}\right)^N \quad (8.137)$$

If now we rupture the membrane, so that particles can sample the total volume,  $V_f$ , what is the entropy change? Well, we can use the same formula to say how the same number of particles now occupies a greater volume:

$$W_f = \left(\frac{V_f}{V_m}\right)^N \quad (8.138)$$

$$\frac{W_f}{W_i} = \left(\frac{V_f}{V_i}\right)^N \quad (8.139)$$

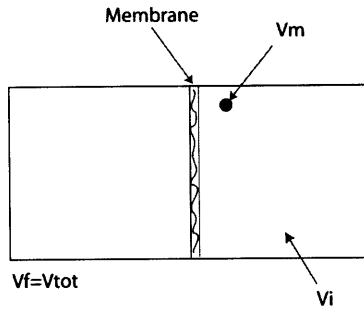


Figure 8-1: Particles occupy right side, membrane ruptures, and the volume available to the system has increased

$$\Delta S = S_f - S_i = (k_B \ln W_f) - (k_B \ln W_i) = k_B \ln \frac{W_f}{W_i} = k_B \ln \left( \frac{V_f}{V_i} \right)^N \quad (8.140)$$

$$\Delta S = N k_B \ln \frac{V_f}{V_i} \quad (8.141)$$

But, we recall that  $N = nN_A$ , where  $N_A$  is avogadro's number, and  $n$  is the number of moles. We can also convert to  $N_A k_B = R$ , so that we have:

$$\Delta S = n N_A k_B \ln \frac{V_f}{V_i} = n R \ln \frac{V_f}{V_i} \quad (8.142)$$

This is the final result for the change in entropy for increasing the volume of a closed container. We can derive the same thing from macroscopics!



- 1) Define our system: System is closed, isolated:  $Q = 0$ ,  $W = 0$ , so  $dU = 0$ . There is constant internal energy.
- 2) Describe what happens with our system: when the membrane is ruptured, gas expands IRREVERSIBLY.

This process reminds us of the ubiquitous piston problem in classical thermodynamics. This also accomplishes the task of increasing volume, to increase entropy. So, to solve this problem, we can find a "reversible" process that will result in the same final state, that is that  $dU = 0$ , since  $U$  is a function of temperature, we can select an isothermal expansion.

$$dU = 0 = dQ_{rev} - dW_{rev} \quad (8.143)$$

$$dW_{rev} = PdV \quad (8.144)$$

$$dQ_{rev} = TdS \quad (8.145)$$

Using the Ideal Gas Law,  $PV = nRT$ , we can make use of  $P = \frac{nRT}{V}$

$$\int_i^f dW_{rev} = \int_{V_i}^{V_f} \frac{nRT}{V} dV = nRT \ln V \Big|_{V_i}^{V_f} = nRT \ln \frac{V_f}{V_i} = \Delta W_{rev} \quad (8.146)$$

$$\int_i^f dQ_{rev} = \int_{S_i}^{S_f} TdS = T(S_f - S_i) = T\Delta S = \Delta Q_{rev} \quad (8.147)$$

But, we already said that  $\Delta W_{rev} = \Delta Q_{rev}$ .

So, we obtain the same result that we did beginning from the microscopics:

$$\Delta S = nR \ln \frac{V_f}{V_i} \quad (8.148)$$

## 8.16 Example: Proving Hooke's Law in an Ideal Polymer

\*this problem was taken from one of my HW problems in APP.225, Introduction to soft matter, Harvard, 2005\*

This problem illustrates how polymers behave as "entropic springs". Consider a one-dimensional model of a polymer consisting of  $N$  segments linked end-to-end, where the angle between successive links is equally likely to be  $0^\circ$  or  $180^\circ$ . Each segment has a length of  $b$ .

(a). Clearly show/argue that the number of configurations that give an overall length of  $L=2mb$  where  $m > 0$  is:

$$\Omega(N, m) = \frac{2N!}{(N/2 + m)!(N/2 - m)!} \quad (8.149)$$

(b). Show that for  $m \ll N$  this expression becomes

$$\Omega(N, m) = \Omega(N, 0) \exp(-2m^2/N) \quad (8.150)$$

(c). Calculate the entropy of the system as a function of  $L$  for  $N \gg 1$  and  $L \ll Nb$ . Explain/interpret your result.

(d). Work required to stretch this polymer an amount  $dL$  is  $f dL$  where  $f$  is the applied force. Calculate an  $f$ - $T$ - $L$  equation of state. Try to explain the observed dependencies on  $L, T, N$ , and  $b$  physically.

SOLUTION (a)

$N_+$  = Number of forward segments

$N_-$  = Number of backfolding segments

Chain Length  $L = 2mb = (N_+ - N_-)b$

$$N = N_+ + N_- \quad (8.151)$$

$$L = (N - 2N_-)b \quad (8.152)$$

$$N_- = \frac{Nb - 2mb}{2b} = \frac{N}{2} - m \quad (8.153)$$

$$N_- = \frac{N}{2} - m \quad (8.154)$$

Similarly,

$$N_+ = \frac{N}{2} + m \quad (8.155)$$

$$\text{For } N_+ > N_-, \Omega_+ = \frac{N!}{(\frac{N}{2}-m)!(\frac{N}{2}-m)!}$$

$$\text{For } N_+ < N_-, \Omega_- = \frac{N!}{(\frac{N}{2}-m)!(\frac{N}{2}-m)!}$$

Total Ways:

$$\Omega = \Omega_- + \Omega_+ = 2 \frac{N!}{(\frac{N}{2}-m)!(\frac{N}{2}-m)!} \quad (8.156)$$

SOLUTION (b)

For  $N \gg m$ , we can use Stirling's formula, where for  $x \gg 1$ ,  $\ln x! = x \ln x - x$  from part (a),

$$\ln \Omega(N, m) = \ln 2 + \ln N! - \ln\left(\frac{N}{2} - m\right)! - \ln\left(\frac{N}{2} + m\right)! \quad (8.157)$$

which can be combined to:

$$\ln \Omega(N, m) = (1 + N) \ln 2 - \left(\frac{N}{2} - m\right) \ln\left(1 - \frac{2m}{N}\right) - \left(\frac{N}{2} + m\right) \ln\left(1 + \frac{2m}{N}\right) \quad (8.158)$$

$$\ln \Omega(N, 0) = \ln \frac{2N!}{(N/2)!(N/2)!} = (1 + N) \ln 2 \quad (8.159)$$

$$\ln \Omega(N, m) = \ln \Omega(N, 0) - (N/2 - m) \ln(1 - 2m/N) - (N/2 + m) \ln(1 + 2m/N) \quad (8.160)$$

for  $x \ll 1$ ,  $\ln x = x - \frac{x^2}{2} + \dots$ ,

$$\frac{m}{N} \ll 1, \ln(1 \pm 2m/N) = \pm 2m/N - 2m^2/N^2$$

$$\ln \Omega(N, m) = \ln \Omega(N, 0) - \left(\frac{N}{2} - m\right) \left(-\frac{2m}{N} - \frac{2m^2}{N^2}\right) - \left(\frac{N}{2} + m\right) \left(\frac{2m}{N} - \frac{2m^2}{N^2}\right) \quad (8.161)$$

$$\ln \Omega(N, m) = \ln \Omega(N, 0) + 2(m^2/N - 2m^2/N) \quad (8.162)$$

$$\ln \Omega(N, m) = \ln \Omega(N, 0) - 2m^2/N \quad (8.163)$$

$$\Omega(N, m) = \Omega(N, 0) \exp(-2m^2/N) \quad (8.164)$$

SOLUTION (c) Entropy:  $S = k_B \ln \Omega(N, m)$

$$S = k_B \ln \Omega(N, 0) - \frac{2k_B m^2}{N} \quad (8.165)$$

From part (b)., we saw:

$$\ln \Omega(N, 0) = (1 + N) \ln 2 \sim N \ln 2 \quad (8.166)$$

for  $N \gg 1$

$$S = k_b N \ln 2 - 2k_B \frac{m^2}{2} \quad (8.167)$$

$$m = \frac{L}{2b}$$

$$S = k_B(N \ln 2 - \frac{L^2}{2Nb^2}) \quad (8.168)$$

SOLUTION (d)

$$dE = TdS + fdL \quad (8.169)$$

$$f = -T \frac{\partial S}{\partial L} = -k_B T \frac{\partial}{\partial L} (N \ln 2 - \frac{L^2}{2Nb^2}) \quad (8.170)$$

$$f = \frac{k_B T L}{Nb^2} \quad (8.171)$$

## 8.17 Example: Force-Dependent Equilibrium Constants(1)

Say that we abstract all of the different configurations that a polymer can take into just two categories, folded and unfolded. There are  $n_u$  unfolded configurations and  $n_f$  folded configurations. We will further state that there are also only two energy states. All folded configurations have the same free energy, and all unfolded configurations have the same free energy. We want to find the displacement over which the force must be applied to yield a particular force-dependent equilibrium constant.

$$P_{fold} = \frac{1}{Z} n_f e^{\frac{-E_{sf} + F\langle \vec{R}_f \rangle}{k_B T}} \quad (8.172)$$

$$P_{unfold} = \frac{1}{Z} n_u e^{\frac{-E_{su} + F\langle \vec{R}_u \rangle}{k_B T}} \quad (8.173)$$

$$\frac{P_{unfold}}{P_{fold}} = \frac{n_u e^{\frac{-E_{su} + F\langle \vec{R}_u \rangle}{k_B T}}}{n_f e^{\frac{-E_{sf} + F\langle \vec{R}_f \rangle}{k_B T}}} \quad (8.174)$$

$$K_{eq} = \frac{P_{unfold}}{P_{fold}} = \frac{n_u}{n_f} e^{\frac{-\Delta E_s + F\langle \Delta \vec{R} \rangle}{k_B T}} \quad (8.175)$$

Here, we are accounting for the fact that there is BOTH a change in the energy due to entropy, as well as a change in energy due to the change in length with applied force. From here, say we are interested in this change in the separation,  $\Delta R$ .

$$\ln K_{eq} = \ln \frac{n_u}{n_f} + \frac{-\Delta E_s + F\langle \Delta \vec{R} \rangle}{k_B T} \quad (8.176)$$

$$\frac{\partial \ln K_{eq}}{\partial F} = \frac{\Delta R}{k_B T} \quad (8.177)$$

$$\Delta R = k_B T \frac{\partial \ln K_{eq}}{\partial F} \quad (8.178)$$

What we have found is the distance over which a given force must be applied in order to yield a given equilibrium constant that describes the probability of being in either a folded or unfolded state.

## 8.18 Example: Force-Dependent Equilibrium Constants (2)

In this example, a constant mechanical force is applied to an RNA hairpin, and we observe the stochastic 'hopping' between being open or closed, unfolded or folded. This probability changes with the magnitude of this applied force, and the traces are seen in the accompanying figure. From these traces, identify the equilibrium constants, and plot the free energy as a function of the applied force.

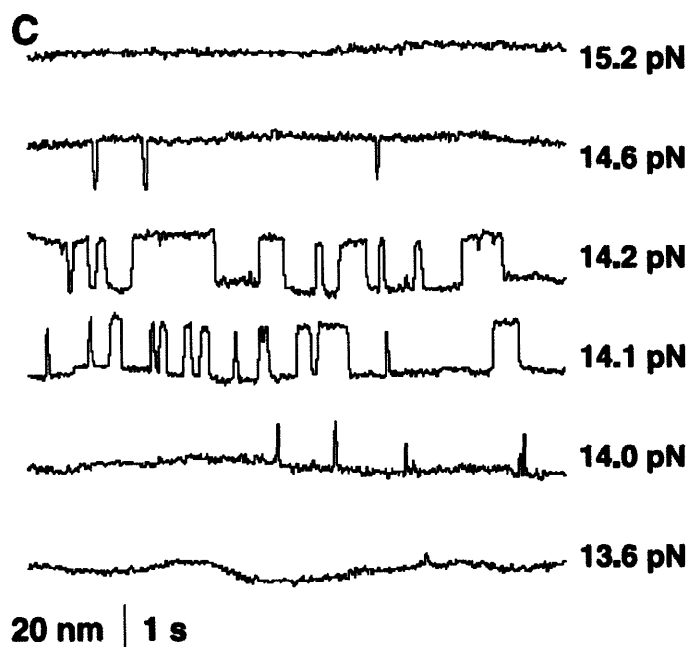


Figure 8-2: Length versus time traces of the RNA hairpin at various constant forces in 10 mM Mg21



## 8.19 Good References

Here are references that were used in the construction of this tutorial, and are very good references in general. Some may be very useful for those who want a more thorough understanding of statistical physics, with no biological slant.

- 1) Chaikin, P.M., Lubensky, T.C., Principles of Condensed Matter Physics (very easy read)
- 2) Thijssen, J.M., Computational Physics (easy read)
- 3) Landau, Lifshitz., Statistical Physics (much harder read)



# Bibliography

- [1] G. Fenteany, P. A. Janmey, and T. P. Stossel. Signaling pathways and cell mechanics involved in wound closure by epithelial cell sheets. *Curr Biol*, 10(14):831–8, 2000. Fenteany, G Janmey, P A Stossel, T P AR38910/AR/NIAMS NIH HHS/United States HL07680/HL/NHLBI NIH HHS/United States HL19429/HL/NHLBI NIH HHS/United States Research Support, Non-U.S. Gov't Research Support, U.S. Gov't, P.H.S. England Current biology : CB Curr Biol. 2000 Jul 13;10(14):831-8.
- [2] A. Jacinto, A. Martinez-Arias, and P. Martin. Mechanisms of epithelial fusion and repair. *Nat Cell Biol*, 3(5):E117–23, 2001. Jacinto, A Martinez-Arias, A Martin, P Research Support, Non-U.S. Gov't Review England Nature cell biology Nat Cell Biol. 2001 May;3(5):E117-23.
- [3] P. B. Armstrong and D. Parenti. Cell sorting in the presence of cytochalasin b. *J Cell Biol*, 55(3):542–53, 1972. 0021-9525 (Print) Journal Article.
- [4] M. Poujade, E. Grasland-Mongrain, A. Hertzog, J. Jouanneau, P. Chavrier, B. Ladoux, A. Buguin, and P. Silberzan. Collective migration of an epithelial monolayer in response to a model wound. *Proc Natl Acad Sci U S A*, 104(41):15988–93, 2007. 0027-8424 (Print) Journal Article Research Support, Non-U.S. Gov't.
- [5] K. Moutairou, P. Fritsch, J. C. Meslin, J. L. Poncy, H. Metivier, and R. Masse. Epithelial cell migration on small intestinal villi in the neonatal rat. comparison between [3h] thymidine and cytoplasmic labelling after pu-citrate ingestion. *Biol*

- Cell*, 65(3):265–9, 1989. Moutairou, K Fritsch, P Meslin, J C Poncy, J L Metivier, H Masse, R France Biology of the cell / under the auspices of the European Cell Biology Organization *Biol Cell*. 1989;65(3):265-9.
- [6] F. Escaffit, N. Perreault, D. Jean, C. Francoeur, E. Herring, C. Rancourt, N. Rivard, P. H. Vachon, F. Pare, M. P. Boucher, J. Auclair, and J. F. Beaulieu. Repressed e-cadherin expression in the lower crypt of human small intestine: a cell marker of functional relevance. *Exp Cell Res*, 302(2):206–20, 2005. 0014-4827 (Print) Journal Article.
- [7] J. F. Beaulieu. Integrins and human intestinal cell functions. *Front Biosci*, 4:D310–21, 1999. 1093-4715 (Electronic) Journal Article Review.
- [8] D. A. Lauffenburger and A. F. Horwitz. Cell migration: a physically integrated molecular process. *Cell*, 84(3):359–69, 1996. 0092-8674 (Print) Journal Article Research Support, U.S. Gov't, P.H.S. Review.
- [9] K. Wolf, I. Mazo, H. Leung, K. Engelke, U. H. von Andrian, E. I. Deryugina, A. Y. Strongin, E. B. Brocker, and P. Friedl. Compensation mechanism in tumor cell migration: mesenchymal-amoeboid transition after blocking of pericellular proteolysis. *J Cell Biol*, 160(2):267–77, 2003. Wolf, Katarina Mazo, Irina Leung, Harry Engelke, Katharina von Andrian, Ulrich H Deryugina, Elena I Strongin, Alex Y Brocker, Eva-B Friedl, Peter CA77470/CA/NCI NIH HHS/United States CA83017/CA/NCI NIH HHS/United States HL54936/HL/NHLBI NIH HHS/United States HL56949/HL/NHLBI NIH HHS/United States Research Support, Non-U.S. Gov't Research Support, U.S. Gov't, P.H.S. United States The Journal of cell biology *J Cell Biol*. 2003 Jan 20;160(2):267-77. Epub 2003 Jan 13.
- [10] J. L. Duband, S. Dufour, S. S. Yamada, K. M. Yamada, and J. P. Thiery. Neural crest cell locomotion induced by antibodies to beta 1 integrins. a tool for studying the roles of substratum molecular avidity and density in migration. *J Cell Sci*, 98 ( Pt 4):517–32, 1991. Duband, J L Dufour, S Yamada, S S Yamada, K M Thiery,

J P Comparative Study Research Support, Non-U.S. Gov't Research Support, U.S. Gov't, P.H.S. England Journal of cell science J Cell Sci. 1991 Apr;98 ( Pt 4):517-32.

- [11] C. M. Lo, H. B. Wang, M. Dembo, and Y. L. Wang. Cell movement is guided by the rigidity of the substrate. *Biophys J*, 79(1):144–52, 2000. 0006-3495 (Print) Journal Article.
- [12] Jr. Pelham, R. J. and Y. Wang. Cell locomotion and focal adhesions are regulated by substrate flexibility. *Proc Natl Acad Sci U S A*, 94(25):13661–5, 1997. 0027-8424 (Print) Journal Article Research Support, U.S. Gov't, P.H.S.
- [13] M. H. Zaman, L. M. Trapani, A. L. Sieminski, D. Mackellar, H. Gong, R. D. Kamm, A. Wells, D. A. Lauffenburger, and P. Matsudaira. Migration of tumor cells in 3d matrices is governed by matrix stiffness along with cell-matrix adhesion and proteolysis. *Proc Natl Acad Sci U S A*, 103(29):10889–94, 2006. 0027-8424 (Print) Journal Article Research Support, N.I.H., Extramural Research Support, Non-U.S. Gov't Research Support, U.S. Gov't, Non-P.H.S.
- [14] A. Engler, L. Bacakova, C. Newman, A. Hategan, M. Griffin, and D. Discher. Substrate compliance versus ligand density in cell on gel responses. *Biophys J*, 86(1 Pt 1):617–28, 2004. 0006-3495 (Print) Journal Article Research Support, Non-U.S. Gov't Research Support, U.S. Gov't, Non-P.H.S. Research Support, U.S. Gov't, P.H.S.
- [15] D. E. Discher, P. Janmey, and Y. L. Wang. Tissue cells feel and respond to the stiffness of their substrate. *Science*, 310(5751):1139–43, 2005. 1095-9203 (Electronic) Journal Article Review.
- [16] S. B. Carter. Haptotaxis and the mechanism of cell motility. *Nature*, 213(5073):256–60, 1967. Carter, S B In Vitro England Nature Nature. 1967 Jan 21;213(5073):256-60.

- [17] J. B. McCarthy, S. L. Palm, and L. T. Furcht. Migration by haptotaxis of a schwann cell tumor line to the basement membrane glycoprotein laminin. *J Cell Biol*, 97(3):772–7, 1983. McCarthy, J B Palm, S L Furcht, L T CA00651/CA/NCI NIH HHS/United States CA21463/CA/NCI NIH HHS/United States CA29995/CA/NCI NIH HHS/United States Research Support, Non-U.S. Gov't Research Support, U.S. Gov't, P.H.S. United states The Journal of cell biology J Cell Biol. 1983 Sep;97(3):772-7.
- [18] D. S. Gray, J. Tien, and C. S. Chen. Repositioning of cells by mechanotaxis on surfaces with micropatterned young's modulus. *J Biomed Mater Res A*, 66(3):605–14, 2003. 1549-3296 (Print) Journal Article.
- [19] J.Y. Wong, A. Velasco, P. Rajagopalan, and Pham Q. Directed movement of vascular smooth muscle cells on gradient-compliant hydrogels. *Langmuir*, 19:1908–1913, 2003.
- [20] J. S. Simske and J. Hardin. Getting into shape: epidermal morphogenesis in caenorhabditis elegans embryos. *Bioessays*, 23(1):12–23, 2001. Simske, J S Hardin, J Research Support, Non-U.S. Gov't Review England BioEssays : news and reviews in molecular, cellular and developmental biology Bioessays. 2001 Jan;23(1):12-23.
- [21] J. S. Simske, M. Koppen, P. Sims, J. Hodgkin, A. Yonkof, and J. Hardin. The cell junction protein vab-9 regulates adhesion and epidermal morphology in c. elegans. *Nat Cell Biol*, 5(7):619–25, 2003. Simske, Jeffrey S Koppen, Mathias Sims, Paul Hodgkin, Jonathan Yonkof, Alicia Hardin, Jeff GM58038/GM/NIGMS NIH HHS/United States Research Support, Non-U.S. Gov't Research Support, U.S. Gov't, Non-P.H.S. Research Support, U.S. Gov't, P.H.S. England Nature cell biology Nat Cell Biol. 2003 Jul;5(7):619-25.
- [22] N. Harden. Signaling pathways directing the movement and fusion of epithelial sheets: lessons from dorsal closure in drosophila. *Differentiation*, 70(4-5):181–203, 2002. Harden, Nicholas Research Support, Non-U.S. Gov't Review Germany

- Differentiation; research in biological diversity *Differentiation*. 2002 Jun;70(4-5):181-203.
- [23] A. Jacinto, W. Wood, S. Woolner, C. Hiley, L. Turner, C. Wilson, A. Martinez-Arias, and P. Martin. Dynamic analysis of actin cable function during drosophila dorsal closure. *Curr Biol*, 12(14):1245–50, 2002. Jacinto, Antonio Wood, William Woolner, Sarah Hiley, Charlotte Turner, Laura Wilson, Clive Martinez-Arias, Alfonso Martin, Paul Research Support, Non-U.S. Gov't England Current biology : CB *Curr Biol*. 2002 Jul 23;12(14):1245-50.
- [24] A. Jacinto, S. Woolner, and P. Martin. Dynamic analysis of dorsal closure in drosophila: from genetics to cell biology. *Dev Cell*, 3(1):9–19, 2002. Jacinto, Antonio Woolner, Sarah Martin, Paul Research Support, Non-U.S. Gov't Review United States Developmental cell *Dev Cell*. 2002 Jul;3(1):9-19.
- [25] Y. Danjo and I. K. Gipson. Actin 'purse string' filaments are anchored by e-cadherin-mediated adherens junctions at the leading edge of the epithelial wound, providing coordinated cell movement. *J Cell Sci*, 111 ( Pt 22):3323–32, 1998. Danjo, Y Gipson, I K R37 EY03306/EY/NEI NIH HHS/United States Research Support, Non-U.S. Gov't Research Support, U.S. Gov't, P.H.S. England Journal of cell science *J Cell Sci*. 1998 Nov;111 ( Pt 22):3323-32.
- [26] Y. Danjo and I. K. Gipson. Specific transduction of the leading edge cells of migrating epithelia demonstrates that they are replaced during healing. *Exp Eye Res*, 74(2):199–204, 2002. Danjo, Yukitaka Gipson, Ilene K England Experimental eye research *Exp Eye Res*. 2002 Feb;74(2):199-204.
- [27] M. Zhao, B. Song, J. Pu, J. V. Forrester, and C. D. McCaig. Direct visualization of a stratified epithelium reveals that wounds heal by unified sliding of cell sheets. *FASEB J*, 17(3):397–406, 2003. Zhao, Min Song, Bing Pu, Jin Forrester, John V McCaig, Colin D 068012/Wellcome Trust/United Kingdom In Vitro Research Support, Non-U.S. Gov't United States The FASEB journal : official publication

of the Federation of American Societies for Experimental Biology FASEB J. 2003 Mar;17(3):397-406.

- [28] G. H. Schmidt, D. J. Winton, and B. A. Ponder. Development of the pattern of cell renewal in the crypt-villus unit of chimaeric mouse small intestine. *Development*, 103(4):785–90, 1988. 0950-1991 (Print) Journal Article Research Support, Non-U.S. Gov't.
- [29] J. P. Heath. Epithelial cell migration in the intestine. *Cell Biol Int*, 20(2):139–46, 1996. 1065-6995 (Print) In Vitro Journal Article Research Support, U.S. Gov't, Non-P.H.S. Review.
- [30] C. S. Potten. Stem cells in gastrointestinal epithelium: numbers, characteristics and death. *Philos Trans R Soc Lond B Biol Sci*, 353(1370):821–30, 1998. 0962-8436 (Print) Journal Article Review.
- [31] Harvey F. Lodish. *Molecular cell biology*. W.H. Freeman, New York, 4th edition, 2000. Harvey Lodish ... [et al.] ill. (some col.) ; 29 cm. + 1 computer optical disc (4 3/4 in.). Ch. 1. The dynamic cell – Ch. 2. Chemical foundations – Ch. 3. Protein structure and function – Ch. 4. Nucleic acids, the genetic code, and the synthesis of macromolecules – Ch. 5. Biomembranes and the subcellular organization of eukaryotic cells – Ch. 6. Manipulating cells and viruses in culture – Ch. 7. Recombinant DNA and genomics – Ch. 8. Genetic analysis in cell biology – Ch. 9. Molecular structure of genes and chromosomes – Ch. 10. Regulation of transcription initiation – Ch. 11. RNA processing, nuclear transport, and post-transcriptional control – Ch. 12. DNA replication, repair, and recombination – Ch. 13. Regulation of the Eukaryotic cell cycle – Ch. 14. Gene control in development – Ch. 15. Transport across cell membranes – Ch. 16. Cellular energetics: glycolysis, aerobic oxidation, and photosynthesis – Ch. 17. Protein sorting: organelle biogenesis and protein secretion – Ch. 18. Cell motility and shape I: microfilaments – Ch. 19. Cell motility and shape II: microtubules and intermediate filaments – Ch. 20. Cell-to-cell signaling: hormones and receptors – Ch. 21.



Nerve cells – Ch. 22. Integrating cells into tissues –Ch. 23. Cell interactions in development – Ch. 24. Cancer.

- [32] M. L. Hermiston, M. H. Wong, and J. I. Gordon. Forced expression of e-cadherin in the mouse intestinal epithelium slows cell migration and provides evidence for nonautonomous regulation of cell fate in a self-renewing system. *Genes Dev*, 10(8):985–96, 1996. 0890-9369 (Print) Journal Article.
- [33] D. L. Nikolic, A. N. Boettiger, D. Bar-Sagi, J. D. Carbeck, and S. Y. Shvartsman. Role of boundary conditions in an experimental model of epithelial wound healing. *Am J Physiol Cell Physiol*, 291(1):C68–75, 2006. 0363-6143 (Print) Journal Article.
- [34] R. Farooqui and G. Fenteany. Multiple rows of cells behind an epithelial wound edge extend cryptic lamellipodia to collectively drive cell-sheet movement. *J Cell Sci*, 118(Pt 1):51–63, 2005. 0021-9533 (Print) Journal Article.
- [35] O. du Roure, A. Saez, A. Buguin, R. H. Austin, P. Chavrier, P. Silberzan, and B. Ladoux. Force mapping in epithelial cell migration. *Proc Natl Acad Sci U S A*, 102(7):2390–5, 2005. 0027-8424 (Print) Journal Article.
- [36] D. A. Beysens, G. Forgacs, and J. A. Glazier. Cell sorting is analogous to phase ordering in fluids. *Proc Natl Acad Sci U S A*, 97(17):9467–71, 2000. 0027-8424 (Print) Journal Article.
- [37] J. A. Glazier and F. Graner. Simulation of the differential adhesion driven rearrangement of biological cells. *Physical Review. E. Statistical Physics, Plasmas, Fluids, and Related Interdisciplinary Topics*, 47(3):2128–2154, 1993. 1063-651X (Print) Journal article.
- [38] P. L. Ryan, R. A. Foty, J. Kohn, and M. S. Steinberg. Tissue spreading on implantable substrates is a competitive outcome of cell-cell vs. cell-substratum adhesivity. *Proc Natl Acad Sci U S A*, 98(8):4323–7, 2001. 0027-8424 (Print) Journal Article.

- [39] P. A. Hall, P. J. Coates, B. Ansari, and D. Hopwood. Regulation of cell number in the mammalian gastrointestinal tract: the importance of apoptosis. *J Cell Sci*, 107 ( Pt 12):3569–77, 1994. Hall, P A Coates, P J Ansari, B Hopwood, D Research Support, Non-U.S. Gov't England Journal of cell science J Cell Sci. 1994 Dec;107 ( Pt 12):3569-77.
- [40] J. W. Cooper, R. F. Hagemann, and Jr. Brodmerkel, G. J. On the determination of intestinal epithelial cell generation time from labeling index and dna synthesis duration. *Experientia*, 30(2):186–8, 1974. Cooper, J W Hagemann, R F Brodmerkel, G J Jr Switzerland Experientia Experientia. 1974 Feb 15;30(2):186-8.
- [41] J. S. Trier, C. H. Allan, D. R. Abrahamson, and S. J. Hagen. Epithelial basement membrane of mouse jejunum. evidence for laminin turnover along the entire crypt-villus axis. *J Clin Invest*, 86(1):87–95, 1990. Trier, J S Allan, C H Abrahamson, D R Hagen, S J DK-34854/DK/NIDDK NIH HHS/United States DK-34972/DK/NIDDK NIH HHS/United States DK-36835/DK/NIDDK NIH HHS/United States Research Support, Non-U.S. Gov't Research Support, U.S. Gov't, P.H.S. United states The Journal of clinical investigation J Clin Invest. 1990 Jul;86(1):87-95.
- [42] Nicholas A. Wright and Malcolm Alison. *The biology of epithelial cell populations*. Oxford science publications. Clarendon Press ; Oxford University Press, Oxford [Oxfordshire] New York, 1984. Nicholas Wright and Malcolm Alison. ill. ; 25 cm. Includes index.
- [43] M. J. Paszek, N. Zahir, K. R. Johnson, J. N. Lakins, G. I. Rozenberg, A. Gefen, C. A. Reinhart-King, S. S. Margulies, M. Dembo, D. Boettiger, D. A. Hammer, and V. M. Weaver. Tensional homeostasis and the malignant phenotype. *Cancer Cell*, 8(3):241–54, 2005. Paszek, Matthew J Zahir, Nastaran Johnson, Kandice R Lakins, Johnathon N Rozenberg, Gabriela I Gefen, Amit Reinhart-King, Cynthia A Margulies, Susan S Dembo, Micah Boettiger, David Hammer, Daniel A Weaver, Valerie M CA078731/CA/NCI NIH HHS/United

States GM57388/GM/NIGMS NIH HHS/United States HL57204/HL/NHLBI NIH HHS/United States HL6438801A1/HL/NHLBI NIH HHS/United States T32HL00795404/HL/NHLBI NIH HHS/United States Research Support, N.I.H., Extramural Research Support, U.S. Gov't, Non-P.H.S. Research Support, U.S. Gov't, P.H.S. United States Cancer cell Cancer Cell. 2005 Sep;8(3):241-54.

- [44] H. O. Brown, M. L. Levine, and M. Lipkin. Inhibition of intestinal epithelial cell renewal and migration induced by starvation. *Am J Physiol*, 205(5):868–72, 1963. Brown, H O Levine, M L Lipkin, M United states The American journal of physiology Am J Physiol. 1963 Nov;205(5):868-72.
- [45] A. D. Luster. Chemokines—chemotactic cytokines that mediate inflammation. *N Engl J Med*, 338(7):436–45, 1998. Luster, A D R01-AI40618/AI/NIAID NIH HHS/United States R01-CA69212/CA/NCI NIH HHS/United States Research Support, Non-U.S. Gov't Research Support, U.S. Gov't, P.H.S. Review United states The New England journal of medicine N Engl J Med. 1998 Feb 12;338(7):436-45.
- [46] D. R. Burgess. Morphogenesis of intestinal villi. ii. mechanism of formation of pre villous ridges. *J Embryol Exp Morphol*, 34(3):723–40, 1975. Burgess, D R England Journal of embryology and experimental morphology J Embryol Exp Morphol. 1975 Dec;34(3):723-40.
- [47] S. Takayama, J. C. McDonald, E. Ostuni, M. N. Liang, P. J. Kenis, R. F. Ismagilov, and G. M. Whitesides. Patterning cells and their environments using multiple laminar fluid flows in capillary networks. *Proc Natl Acad Sci U S A*, 96(10):5545–8, 1999. Takayama, S McDonald, J C Ostuni, E Liang, M N Kenis, P J Ismagilov, R F Whitesides, G M GM30367/GM/NIGMS NIH HHS/United States Research Support, Non-U.S. Gov't Research Support, U.S. Gov't, Non-P.H.S. Research Support, U.S. Gov't, P.H.S. United states Proceedings of the National Academy of Sciences of the United States of America Proc Natl Acad Sci U S A. 1999 May 11;96(10):5545-8.

- [48] L. W. Anderson, K. G. Danielson, and H. L. Hosick. New cell line. epithelial cell line and subline established from premalignant mouse mammary tissue. *In Vitro*, 15(11):841–3, 1979. Anderson, L W Danielson, K G Hosick, H L Research Support, U.S. Gov't, P.H.S. United states In vitro In Vitro. 1979 Nov;15(11):841-3.
- [49] K. H. Yoon, M. Yoon, R. D. Moir, S. Khuon, F. W. Flitney, and R. D. Goldman. Insights into the dynamic properties of keratin intermediate filaments in living epithelial cells. *J Cell Biol*, 153(3):503–16, 2001. Yoon, K H Yoon, M Moir, R D Khuon, S Flitney, F W Goldman, R D 1 PO1 DE12328/DE/NIDCR NIH HHS/United States Research Support, U.S. Gov't, P.H.S. United States The Journal of cell biology J Cell Biol. 2001 Apr 30;153(3):503-16.
- [50] J. L. Schwachtgen, P. Houston, C. Campbell, V. Sukhatme, and M. Braddock. Fluid shear stress activation of egr-1 transcription in cultured human endothelial and epithelial cells is mediated via the extracellular signal-related kinase 1/2 mitogen-activated protein kinase pathway. *J Clin Invest*, 101(11):2540–9, 1998. Schwachtgen, J L Houston, P Campbell, C Sukhatme, V Braddock, M United states The Journal of clinical investigation J Clin Invest. 1998 Jun 1;101(11):2540-9.
- [51] K. M. Ridge, L. Linz, F. W. Flitney, E. R. Kuczmarski, Y. H. Chou, M. B. Omary, J. I. Sznajder, and R. D. Goldman. Keratin 8 phosphorylation by protein kinase c delta regulates shear stress-mediated disassembly of keratin intermediate filaments in alveolar epithelial cells. *J Biol Chem*, 280(34):30400–5, 2005. Ridge, Karen M Linz, Laura Flitney, Frederick W Kuczmarski, Edward R Chou, Ying-Hao Omary, M Bishr Sznajder, Jacob Iasha Goldman, Robert D P01-DE12328/DE/NIDCR NIH HHS/United States P01-HL71643/HL/NHLBI NIH HHS/United States Research Support, N.I.H., Extramural Research Support, Non-U.S. Gov't Research Support, U.S. Gov't, Non-P.H.S. Research Support, U.S. Gov't, P.H.S. United States The Journal of biological chemistry J Biol Chem. 2005 Aug 26;280(34):30400-5. Epub 2005 Jun 22.

- [52] William Bloom and Don Wayne Fawcett. *A textbook of histology*. Saunders, Philadelphia, 10th edition, 1975. William Bloom, Don W. Fawcett. ill. ; 27 cm.
- [53] W. H. Guo, M. T. Frey, N. A. Burnham, and Y. L. Wang. Substrate rigidity regulates the formation and maintenance of tissues. *Biophys J*, 90(6):2213–20, 2006. 0006-3495 (Print) Journal Article Research Support, N.I.H., Extramural.
- [54] Paul M. Chaikin and T. C. Lubensky. *Principles of condensed matter physics*. Cambridge University Press, Cambridge, 1st pbk. edition, 2000. P.M. Chaikin, T.C. Lubensky. ill. ; 25 cm. Originally published 1995. Overview – Structure and scattering – Thermodynamics and statistical mechanics – Mean-field theory – Field theories, critical phenomena, and the renormalization group – Generalized elasticity – Dynamics : correlation and response – Hydrodynamics – Topological defects – Walls, kinks, and solitons.
- [55] B. Szabo, G. J. Szollosi, B. Gonci, Z. Juranyi, D. Selmeczi, and T. Vicsek. Phase transition in the collective migration of tissue cells: experiment and model. *Phys Rev E Stat Nonlin Soft Matter Phys*, 74(6 Pt 1):061908, 2006. 1539-3755 (Print) Journal Article Research Support, Non-U.S. Gov't.
- [56] H. Haga, C. Irahara, R. Kobayashi, T. Nakagaki, and K. Kawabata. Collective movement of epithelial cells on a collagen gel substrate. *Biophys J*, 88(3):2250–6, 2005. 0006-3495 (Print) Journal Article Research Support, Non-U.S. Gov't.
- [57] X. Q. Brown, K. Ookawa, and J. Y. Wong. Evaluation of polydimethylsiloxane scaffolds with physiologically-relevant elastic moduli: interplay of substrate mechanics and surface chemistry effects on vascular smooth muscle cell response. *Biomaterials*, 26(16):3123–9, 2005. 0142-9612 (Print) Journal Article.
- [58] R. K. Sawhney and J. Howard. Slow local movements of collagen fibers by fibroblasts drive the rapid global self-organization of collagen gels. *J Cell Biol*, 157(6):1083–91, 2002. 0021-9525 (Print) Comparative Study Journal Article Research Support, Non-U.S. Gov't Research Support, U.S. Gov't, P.H.S.

- [59] L. D. Landau, E. M. Lifshitz, Arnold B. d Markovich Kosevich, and L. P. Pitaevskii. *Theory of elasticity*. Pergamon Press, Oxford [Oxfordshire] ; New York, 3rd english edition, 1986.
- [60] X. Lei, B. J. Ackerson, and P. Tong. Settling statistics of hard sphere particles. *Phys Rev Lett*, 86(15):3300–3, 2001. Lei, X Ackerson, B J Tong, P United States Physical review letters *Phys Rev Lett*. 2001 Apr 9;86(15):3300-3.
- [61] A. R. Abate and D. J. Durian. Topological persistence and dynamical heterogeneities near jamming. *Phys Rev E Stat Nonlin Soft Matter Phys*, 76(2 Pt 1):021306, 2007. Abate, A R Durian, D J United States Physical review. E, Statistical, nonlinear, and soft matter physics *Phys Rev E Stat Nonlin Soft Matter Phys*. 2007 Aug;76(2 Pt 1):021306. Epub 2007 Aug 30.
- [62] Y. Tseng, T. P. Kole, and D. Wirtz. Micromechanical mapping of live cells by multiple-particle-tracking microrheology. *Biophys J*, 83(6):3162–76, 2002. Tseng, Yiider Kole, Thomas P Wirtz, Denis Comparative Study Evaluation Studies Research Support, U.S. Gov't, Non-P.H.S. United States Biophysical journal *Biophys J*. 2002 Dec;83(6):3162-76.
- [63] S. Yamada, D. Wirtz, and S. C. Kuo. Mechanics of living cells measured by laser tracking microrheology. *Biophys J*, 78(4):1736–47, 2000. 0006-3495 (Print) Journal Article.